

# **AARP - XlabF: Compact Solutions for Future Advanced X-ray Studies**

**Vol. LXXV**

**Editor: D. Hampai**



# FRASCATI PHYSICS SERIES

Series Editor  
Antonella Antonelli

Technical Editor  
Lia Sabatini

Cover by Elisa Santinelli

---

Volume LXXV

---

*Istituto Nazionale di Fisica Nucleare – Laboratori Nazionali di Frascati*  
*Divisione Ricerca*  
*Ufficio Biblioteca e Pubblicazioni Scientifiche*  
*P.O. Box 13, I-00044 Frascati Roma Italy*  
*email: [library@lists.lnf.infn.it](mailto:library@lists.lnf.infn.it)*

Copyright © 2022 by INFN

*All rights reserved. No part of this publication may be reproduced, stored in a retrieval system or transmitted in any form or by any means, electronic, mechanical, photocopying, recording or otherwise, without the prior permission of the copyright owner.*  
*ISBN 978-88-86409-76-6*

**AARP - XlabF: Compact Solutions for  
Future Advance X-ray Studies**

**22 June 2022**



Frascati Physics Series Vol. 75  
 AARP - XlabF: Compact Solutions for Future Advanced X-ray Studies  
 Jun 22, 2022

## Scientific Program

S. Dabagov, INFN-LNF, XlabF	“Opening - Introductory talk on the subject and history”
D. Hampai, INFN-LNF, XlabF	"XlabF an Italian X-ray Reference Point"
V. Guglielmotti, INFN-LNF, XlabF	"Applications of x-rays and optics @XLab Frascati: from Cultural Heritage to materials analysis"
A. Di Filippo, Univ. della Tuscia	“Tree-rings as unique natural archives to reconstruct environmental change in time and space”
L. Migliorati, Univ. Di Roma Sapienza	“Peltuinum: la città romana e i campi interdisciplinari”
S. Sanna, Univ.di Roma Tor Vergata	“X-ray characterization of ultra thin free-standing doped ceria membrane for green hydrogen”
E. Bocci, Univ. Guglielmo Marconi	“Innovative energy projects and related materials analysis”
E. Ciro Zuleta Univ. Guglielmo Marconi	“High temperature conditioning and solid oxide fuel cell: experimental tests and analysis”
A. Tocchio, XGLAB	“DANTE - Digital Pulse Processor for X-ray Spectroscopy”
F. Picollo, Univ. Torino, INFN Sezione Torino	“Single cell level radiobiology at High Brilliance X-Ray Source Laboratory”
C. M. Martella – Univ. della Tuscia, XlabF	"Life in space project: Fungal growth ability and ultrastructural damage after growth in hypersaline substrata"
Z. Ebrahimpour, INFN-LNF	“Development and characterization of novel optics for focusing X-rays”
F. Bonfigli, ENEA Frascati	"Volumetric reconstruction of color center distributions in X-ray irradiated LiF crystals obtained by confocal spectromicroscopy techniques"
I. Cacciotti, Univ. Niccolò Cusano	"Multifunctional advanced (bio)materials for applications in the biomedical, environmental and food sectors “
S. Ceccarelli, Univ. di Roma Tor Vergata	“Colour characterisation of a painted Japanese emakimono”
A. Giannoncelli, Elettra,Sincrotrone Trieste	"Advances in X-ray Fluorescence Spectromicroscopy at TwinMic beamline in Elettra"



Frascati Physics Series Vol. 75 (2022)  
AARP - XlabF: Compact Solutions for Future Advanced X-ray Studies  
Jun 22, 2022

## FOREWORD

I am pleased to present this special issue of the Frascati Physics Series (FPS), compiled by selected contributions of the workshop AARP - XlabF: Compact Solutions for Future Advanced X-ray Studies.

The AARP series (Advanced Accelerator & Radiation Physics seminars has been proposed and organised by Prof. S.B. Dabagov and non officially known as "Dabagov's seminar" ), based on international meetings, is dedicated to the frontier topics in both fundamental and applied research associated with new techniques of beam acceleration, novel powerful radiation sources, and radiation physics applications. Previous events were held at NRNU MEPhI, at the National Laboratories of Frascati of the National Institute for Nuclear Physics (INFN-LNF), at CERN, at the Naples' Institute of Engines (IM CNR), at CEA Cadarache Research Center, and many Universities in Europe. They were dedicated to novel techniques for electron beam acceleration, to advanced methods for free electron lasers, to Compton scattering of relativistic electrons in strong laser fields, to laser-plasma wakefield acceleration technique, advanced X-ray optical solutions for various studies (e.g., incoherent and coherent X-ray imaging by tabletop facilities), novel X-ray spectroscopy instrumentation, powerful X-ray source studies by means of polycapillary optics, etc., as well as research performed in the framework of various international collaborations.

In the AARP framework, the workshop Compact Solutions for Future Advanced X-ray Studies was organised by LNF INFN in Frascati (Italy) on 22<sup>th</sup> June 2022. As a part of this workshop, presented volume represents a successful extension of all the experiments that were carried out at XlabF (INFN-LNF) and partially already presented in a number of the proceedings volumes and books issued by SPIE, Journal of Modern Physics A, Il Nuovo Cimento, Nuclear Instruments & Methods in Physics Research B, Physical Review: Accelerator & Beams, World Scientific Publ.

The common thread of the "Compact Solutions for Future Advanced X-ray Studies" workshop was the interaction of X-ray radiation in a matter, in particular, laboratory X-ray analysis techniques within the XlabF collaborations.

The history of X-ray physics has started more than 100 years ago. In 1895, W. Roentgen; at University of Würzburg (Germany), accidentally discovered that electricity, when passed through a glass vacuum tube known as a Crookes' tube, emanates invisible rays (unknown to that time - the origin of the name "X"), which can pass through the human body. Providing with imaging of body tissue, this feature has been used in medicine since the very beginning (even without any knowledge and then any restriction for many years). This discovery was awarded with the first Nobel Prize in Physics. About 15 years later, following the discovery of the diffraction of X-rays by Max von Laue in 1913, two major fields of materials analysis have developed: wavelength-dispersive spectrometry and energy-dispersive spectrometry. By one side the energy dispersive spectrometry allows the unique identification of an element to be made and elemental concentrations can be estimated from characteristic line intensities, X-ray Florescence (XRF) spectrometry. The second field of materials analysis involves characterization by means of atomic arrangement in the crystal lattice, X-ray Diffraction (XRD) spectrometer.

During the XX century, X-ray studies have led to the awarding of several Nobel Prizes. The most famous, and already cited, was W. Roentgen (Physics - 1901), followed by P. Von Lenard (Physics, "for his work on cathode rays" - 1905), M. Von Laue (Physics, "For his discovery of the diffraction of X-rays by crystals" - 1914), W.H Bragg and W.L. Bragg (Physics, "For their services in the analysis of crystal structure by means of X-rays', an important step in the development of X-ray crystallography" - 1915), C.G. Barkla (Physics, "For his discovery of the characteristic Röntgen radiation of the elements', another important step in the development of X-ray spectroscopy" - 1917), K.M.G. Sieghan (Physics, "for his discoveries and research in the field of X-ray spectroscopy" - 1924). All these studies are directly connected to theories and/or experimental applications. However, X-rays were paramount for many other Nobel Prizes, in particular I want to cite P.J.W. Debye (Chemistry, "for his work on molecular structure through his investigations on dipole moments and the diffraction of X-rays and electrons in gases" - 1936), H.J. Muller (Medicine, "or the discovery of the production of mutations by means of X-ray irradiation" - 1946), F.H.C. Crick, J.D. Watson and M.H.F. Wilkins (Medicine, "for their discoveries concerning the molecular structure of nucleic acids and its significance for information transfer in living material" - 1962), D.C. Hodgkin (Chemistry, "for her determinations by X-ray techniques of the structures of important biochemical substances" - 1964) and R. Giacconi (Physics, "for pioneering contributions to astrophysics, which have led to the discovery of cosmic X-ray sources" - 2002).



Figure 1: XlabF facilities @ INFN-LNF

As of today, XRF analysis finds a wide range of application since it allows the quantitative analysis of elements in the periodic table, from F (atomic number 9) upwards. Newer developments allow also the determination of the low atomic number elements including B, C, O and N. On the other side, XRD is applicable to any ordered (crystalline) material and although much less accurate or sensitive than the fluorescence method, is almost unique in its ability to differentiate phases. The fluorescence and diffraction techniques are to a large extent complementary, since one allows accurate quantitation of elements to be made and the other allows qualitative and semi-quantitative estimations to be made of the way in which the matrix elements are combined to make up the phases in the specimen. Thus a combination of the two techniques will often allow the accurate determination of the material balance of a sample.

Since the beginning of 21<sup>st</sup> century, at the Frascati's National laboratories (LNF), we dedicated research program on selected topics of X-ray physics within the projects of the INFN CSN1/CSN5 commissions. This activity has collected the researches in a wide spectrum of fundamental and applied physics dealing with interaction of beams and radiations in media, and over time became the basis for the creation of a specialised laboratory, so-called "XLab-Frascati" (XlabF, "Dabagov Lab", ~ 2010).

One of the main experimental activity of XlabF is in the field of X-ray spectroscopic and imaging analyses. The experience for X-ray manipulation by polycapillary optics defines the main XlabF experimental activities on the laboratory instrumentations for XRD,  $\mu$ XRF and  $\mu$ CT, which allow performing studies in various applications such as cultural heritage, innovative ma-

materials, medical diagnostics, pharmacology, radiation diagnostics, novel scientific detectors characterization, etc. Furthermore, the ability of designing and manufacturing dedicated polycapillary optics allows XlabF to evaluate various experimental schemes for different spectroscopic and imaging applications, resulting in the design and development of various instrumental prototypes and new desktop workstations for advanced compact X-ray techniques.

In general, the topics presented in this workshop are related to experimental activities at XlabF, by researchers from both LNF and the National and International collaborations performed at several private companies, universities and research institutions.



Figure 2: Workshop Poster

After brief introduction to the origin and scope of XlabF done by Prof. S. Dabagov, the chairman D.H. has presented a summary talk on X-ray Techniques, in particular the used ones at XlabF, all the activities for R&D of novel experimental systems as well as for the Technological Transfer department of INFN. Successfully we had oral presentations that cover several fields as follows:

- new tool for semi-quantitative analysis, in particular applied on cultural heritage (Dr,ssa V. Guglielmotti);

- XRF analysis on pigments from ancient scrolls (Dr.ssa S. Ceccarelli);
- the status of the Peltuinum archeological site, enhancing the the XRF and XRD analysis (Pof.ssa L. Migliorati);
- XRF analysis on tree rings as natural archives for pollutant quantification in time and space finalized to evaluate the climate change;
- several studies on advanced materials, for green energy applications, by XRF and XRD (Prof. E. Bocci, Prof. S. Sanna, PrDr. E.C. Zuletta);
- XRF and  $\mu$ XRF on biological and exo-biological samples (Dr. F. Picollo, Dr.ssa M.C. Martella, Prof.ssa I. Cacciotti, Dr.ssa A. Giannoncelli);
- MCP Optics as a novel X-ray optical devices and relative applications (Dr.ssa Z. Ebrahimpour);
- novel X-ray detectors, both regarding new sensors and new hardware (Dr.ssa F. Bonfigli, Dr. A. Tocchio).

All these presentations were based on the results of the experiments performed at XlabF (as a facility for external users). A good portion of the contributions to the workshop are collected in this book, which could hence be a useful collection. More details and the slides of the talks can be found at: <https://agenda.infn.it/event/31663/>.

In conclusion, I would like to point out that the success of the workshop "AARP - XlabF: Compact Solutions for Future Advanced X-ray Studies" was due to the careful work of the workshop co-chair, Dr.ssa V. Guglielmotti, the secretaries as well as the support from INFN and Dr. F. Galdenzi, who helped me review all the articles included in this book. I am pleased to recognise an attentive supervision of the workshop done by Prof. Dabagov.

Finally, I would like to acknowledge the work by Prof. S. Dabagov and Dr. G. Cappuccio started more than 25 years ago that finalised in establishing XlabF as a new facility at LNF, with the outlook to extend the activities opening to external users as a X-ray laboratory with several techniques.

I hope that this FPS volume will take a worthy place in your library along with well-known published books and papers on XRF, XRD and Imaging applied in several fields, as a possible point of reference on X-ray Techniques.

Dariush Hampai

chairman of the "AARP - XlabF: Compact Solutions for Future Advanced X-ray Studies" Workshop

Frascati (Rome), September 25, 2024



Frascati Physics Series Vol. 75  
AARP - XlabF: Compact Solutions for Future Advanced X-ray Studies  
Jun 22, 2022

## CONTENTS

D. Hampai, INFN -LNF, XlabF	"XlabF an Italian X-ray Reference Point"	1
A. Di Filippo, Univ. della Tuscia	"Tree-rings as unique natural archives to reconstruct environmental change in time and space"	38
F. Bonfigli, ENEA Frascati	"Volumetric reconstruction of color center distributions in X-ray irradiated LiF crystals obtained by confocal spectromicroscopy techniques"	51
S. Ceccarelli, Univ. Tor Vergata	"Colour characterisation of a painted Japanese emakimono"	63
S. Pettinato Univ. N. Cusano	A high-quality single-crystal CVD- Diamond dosimeter for high energy photon beams monitoring	83
L. Migliorati, Univ. Sapienza	"Peltuinum: la città romana e i campi interdisciplinari"	98
F. Picollo Univ. Torino, INFN Sez.Torino	"High dose-rate and spatial resolution X-Ray beam at the high brilliance X-Ray Laboratory (HIBRID LAB)	115



## **XLABF - AN ITALIAN X-RAY REFERENCE POINT**

D. Hampai

*INFN-LNF, XLab Frascati, Frascati, Italy*

V. Guglielmotti

*INFN-LNF, XLab Frascati, Frascati, Italy*

E. Capitolo

*INFN-LNF, XLab Frascati, Frascati, Italy*

S.B. Dabagov

*INFN-LNF, XLab Frascati, Frascati, Italy*

*RAS P.N. Lebedev Physical Institute, 119991, Moscow, Russia.*

*National Research Nuclear University MEPhI, 115409, Moscow, Russia*

### **Abstract**

X-ray analytical techniques are widely used in the world. However, due to the strong radiation-matter interaction, to design optical devices suitable for X-ray radiation remains a challenge. As a consequence of novel advanced material studies, in the last 30 years several tipologies of X-ray lenses have been developed. This work is a short review on the status of X-ray optical devices, in particular of polycapillary optics (polyCO), from design and fabrication to various applications.

Contextually, in this review we will report the activities of our lab, XLab Frascati (XlabF) at INFN-LNF, with a focus on new advanced X-ray imaging and spectroscopy tools based on combination of the modern polyCO hardware and the reconstruction software, available as in-house developed and commercial ones, in three main fields, *high resolution X-ray imaging*, *micro-XRF spectroscopy* and *micro-tomography*.

## 1 Introduction

X-rays are widely used in analytical techniques all around the world. Although the advent of higher and more brilliant sources, in many cases proper optical elements for manipulating the beam are required and getting such devices for X-ray photons is not simple due to the strong interaction of radiation with matter.

The pioneering works of Laue <sup>1)</sup> and Compton <sup>2)</sup> on the reflection of X-rays by a smooth surface made possible to design an optical device capable to manage and manipulate coherent and collimated beams at grazing incidence angles. However, according to the Bragg condition, the relatively low interplanar distance in ordinary crystals leads to many limits on their use as X-ray optical devices. At the beginning, all powerful X-ray optics were based on mirrors built on two grazing incidence schemes, one proposed in 1948 by Kirkpatrick and Baez <sup>3)</sup>, and the other in 1952 by Wolter <sup>4)</sup>. In both cases, a very precise coincidence of the optical axes of the mirrors and a thorough treatment of the surfaces is required, and they are actually used only at Synchrotron Radiation facilities (SR).

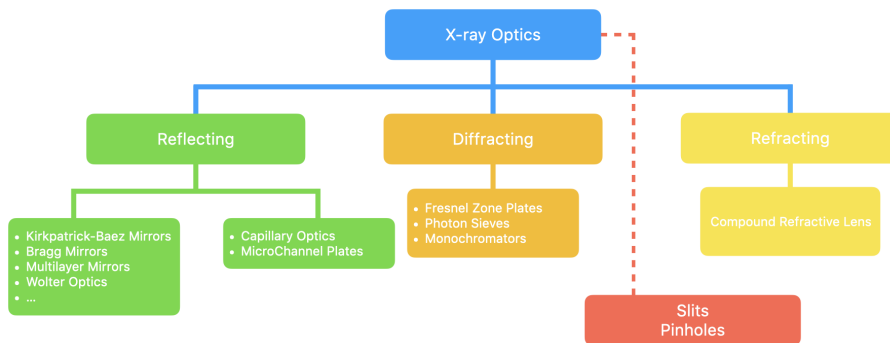


Figure 1: *X-ray optics categories scheme.*

The advances in material engineering processes have allowed to extend the possibilities of configuration for grazing-incidence optics. The new optical X-ray devices can be divided in three main categories (Fig. 1): reflective,

refractive and diffractive optics, while "aperture" optics, as slits or pinhole, are not properly considered as optics.

In the following section a general overview on the very recent status of all the optics will be done. In particular, a focus on the capillary optics state-of-the-art and the latest results in different analytical fields achieved at XLab Frascati by means of polyCO combined with conventional sources will be reported.

## 2 State of the Art

The hard X-ray region is taken as extending from about few keV (around 1 keV) to gamma rays with several hundred keV ( $\sim 100$  keV). Within this energy range, X-ray optics are divided in three main categories, defined by the basics of the phenomenon, summarized in Tab. 1. For a first approach to the different kind of X-ray optics, one can refer to several works <sup>5, 6, 7, 8, 13, 14, 15</sup>.

In the next sections, some of the most common X-ray optics, at least one for each category, will be reported.

### 2.1 Reflective mirrors

The principal limit of an X-ray imaging optical system is to generate images with a resolution equal to the diffraction limit  $D_{diff}$  <sup>16, 17</sup>):

$$D_{diff} = \frac{\lambda}{2 \sin(\theta_a/2)} \quad (1)$$

where  $\theta_a$  is the largest aperture angle between the rays that form the image, and  $\lambda$  is the radiation wavelength.

Taking into account that the reflective optics is based on the total external reflection (TER) phenomenon, the largest aperture angle for the focusing element at grazing incidence is  $2\theta_c$ . At X-ray wavelengths, the refraction index  $n \sim 1 - \delta + i\beta$  is less than 1, but the deviation is proportional to electron density. Due to  $n < 1$ , X-rays bend away from the normal when entering dense materials, whereas visible light bends towards the normal. High reflectivity occurs when the glancing angle is below a critical angle  $\theta_c < \sqrt{2\delta}$ .

$$\theta_c = 2.32 \cdot 10^3 \left( \frac{Z\rho}{A} \right)^{\frac{1}{2}} \lambda < \sqrt{2\delta} \quad (2)$$

where  $Z$ ,  $A$  and  $\rho$  are the atomic number, atomic mass and density, respectively, of the surface and  $\lambda$  is the X-ray wavelength in nm. From this derives that suitable materials for producing the mirrors are metals with high density, such as gold, nickel, and platinum to name a few.

Therefore, the maximum possible resolution is given by the formula:

$$(D_{diff})_{max} = \frac{\lambda}{2 \sin(\theta_c)} \quad (3)$$

For spherical and cylindrical mirrors, the resolution  $D$  is mainly determined by the values of the aberrations  $D_{ab}$ , as  $D = \sqrt{(D_{diff}^2 + D_{ab}^2)}$ . The aberration component is mainly dependent on the geometrical properties of the mirror and the experimental layout (in particular on primary axial spherical aberration and the slope of the focal surface) <sup>18</sup>.

To reduce aberrations when using spherical mirrors, one should work with large grazing angles and with small apertures. To satisfy the first condition, it is mandatory to use heavy material during the manufacturing in order to provide a large critical angle, as gold, platinum, iridium. For the second condition, reducing the aperture for limiting spherical aberrations and coma limit the number of photons collected. A spherical aberration can be completely eliminated using a parabolic or elliptical mirror, while coma cannot be corrected by reflecting X-rays from a single surface of any shape.

A good compromise is the combinations of mirrors in order to reduce aberrations in real grazing-incidence systems. Composite systems in which radiation is reflected from two or more spherical or aspherical surfaces are divided into two types: mirrors where the meridian planes are mutually perpendicular (Kirkpatrick-Baez systems) and mirrors that use combinations of coaxial and confocal conic sections (Wolter systems.)

### 2.1.1 Kirkpatrick-Baez Mirrors

The first grazing incidence system to form a real image was proposed by Kirkpatrick and Baez <sup>3</sup>). Fig. 2 shows a geometrical arrangement of such a so-called Kirkpatrick-Baez system (KB mirrors). KB optics consists of two orthogonal curved mirrors and is practically employed only at synchrotron laboratories, while Wolter optics consists of two tubular rotationally symmetric TER-mirrors. The first reflection focuses to a line, which is focused by the

second surface to a point. This was necessary to avoid the extreme astigmatism suffered from a single mirror but it was not free of geometric coma aberrations, yet. Nevertheless, the system is attractive for being easy to construct the reflecting surfaces. These surfaces can be produced as flat plates and then mechanically bent to the required curvature. To enhance the reflectivity, multilayer mirrors, where the refractive index varies periodically with depth, can be used. Multilayer mirrors are formed by depositing alternating layers of two materials of different refractive index that form long-term stable interfaces. Typically the two materials are made by alternating high and low atomic number ( $Z_0$ ) in order to maximize the difference in electron density. Today, as a result of improved techniques for developing highly finished and perfect surfaces, ellipsoidal and paraboloidal, instead of cylindrical shape, mirrors can be manufactured to a high degree of perfection, and focusing down to 10 nm spot size <sup>9)</sup>.

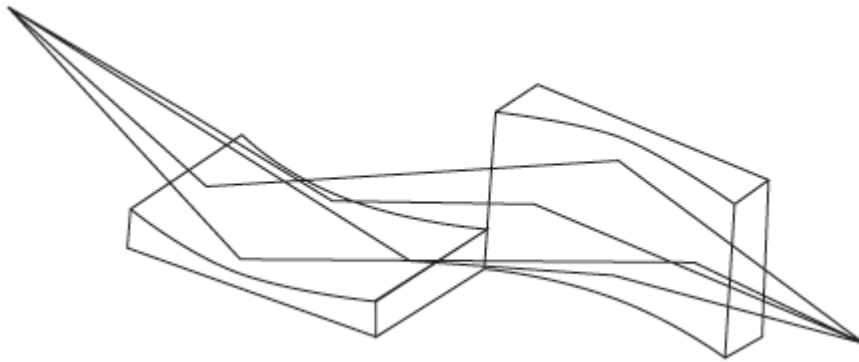


Figure 2: *The arrangement of the Kirkpatrick-Baez X-ray objective* <sup>3)</sup>.

However, the disadvantage of grazing incidence optics, as KB, is the very low acceptance angle and the huge dimensions of the system, thus limiting the use only in SR facilities for scanning microscopies and spectroscopies.

### 2.1.2 Wolter Optics Mirrors

A solution to coma aberration problem coming from KB mirrors was partially solved in 1952 by Wolter <sup>4)</sup>, through double sequential reflection of X-rays from two mirrors of different curvature. Wolter mirrors are located in coaxial configurations and have a common focus.

Mirrors with revolution surfaces (paraboloids, hyperboloids and ellipsoids) are able to achieve images not distorted by aberrations in an extended field of view. The beam path should be formed by two consecutive reflections on combinations of paraboloid-hyperboloid or paraboloid-ellipsoid surfaces located in coaxial and confocal geometry <sup>24)</sup>.

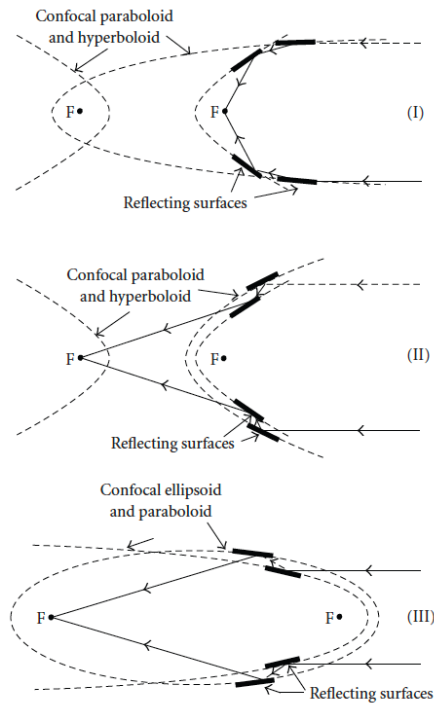


Figure 3: *The schematics of Wolter X-ray lenses <sup>4)</sup>.*

As different mirrors configurations, Wolter proposed focusing systems of

three different types, which became known as the Wolter I, II and III systems, where the main difference is the ratio of the length of the focus to the total length of the system, i.e., the minimum physical length of the telescope. The efficiency of these optics depends on the ratio of effective aperture to total aperture, the reflectivity of the mirror surfaces and the amount of stray light produced by the surface roughness  $R$  of the mirrors ( $R$  has to be at least below 1 nm). In particular, in the following we summarize the characteristics of each type:

- Type I Wolter optics consist of an elliptical mirror (or a parabolic mirror in the case the source is very distant, so the incoming light is parallel to the optical axis) followed by a hyperbolic mirror. This type of Wolter optics is used in X-ray telescopes, because of its relatively short focal length and the possibility to nest several mirrors in concentric shells to increase the total aperture.
- Type II Wolter optics again consist of an elliptical mirror (or once again a parabolic mirror in the case of a distant source, so the incoming light is parallel to the optical axis) followed by a hyperbolic mirror. But in this case the mathematical focal point of the hyperbola being closer to the light source has to coincide with the focal point of the ellipse (respectively parabola).
- Type III Wolter optics only work for incoming light nearly parallel to the optical axis, i.e. for very distant sources. They consist of a parabolic mirror followed by an elliptical mirror.

The Wolter I system is the most widely used due to the simplest configuration. It is preferable in analysis where the optimization criteria are the most effective collection area for X-rays and a large field of view. Moreover, Wolter I optics allows several optical elements to be nested into each other increasing the effective area of reflection. This is an extremely important aspect for the design of telescopes, since almost all sources of cosmic X-ray radiation are weak, and the maximum aperture of the mirror system is crucial <sup>25, 26</sup>).

### 2.1.3 *Poilycapillary Optics*

In analogy to visible light fibre optics, another type of X-ray optics, based as previous devices on total external reflection, are single or straight or tapered

hollow glass tubes<sup>27)</sup>, Fig 4<sup>28)</sup>). This type of X-ray optics, based on an assembly of a large number of hollow capillary tubes stacked together, was hypothesized by Kumakhov in 1984 and realized in 1986. In this type of X-ray lenses, the incident beam hit the tubes interior surface at small angles (accordingly with the experimental setup, the source and the detector, smaller than the critical angle) and is guided through the channel by total external reflection.

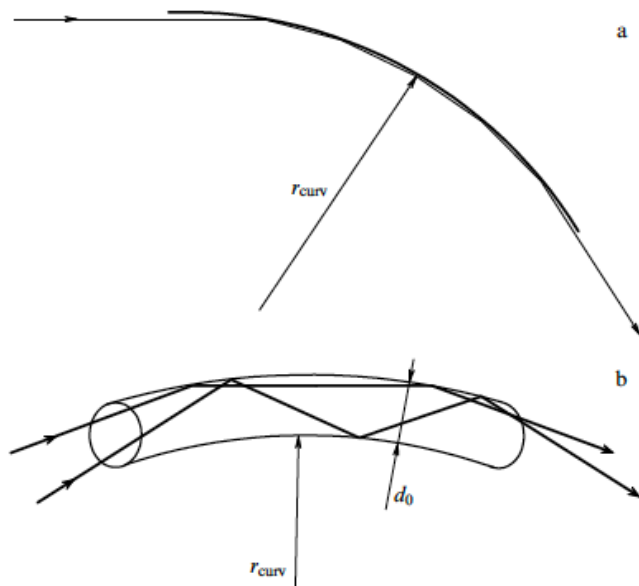


Figure 4: *The bending of a beam by a curved surface with a curvature radius  $r_{curv}$  (a) and a bent capillary with a diameter  $d_0$  and a curvature radius  $r_{curv}$  (b), from<sup>28)</sup>.*

For a bended capillary, not all rays entering the channel satisfy the condition  $\theta < \theta_c$ . Assuming that the inner radius  $r_0 = d_0/2$  of the capillary is small compared to the curvature radius  $r_{curv}$  of the bent capillary ( $r_0/r_{curv} \ll 1$ ) and take into account the fact that the critical TER angle for X-ray photons is small ( $\theta_c \ll 1$ ), the expression for the maximum value of the glancing angle

can be written as follows <sup>29)</sup>:

$$\theta_{max} \sim 2 \left( \frac{r_0}{r_{curv}} \right)^{\frac{1}{2}} \quad (4)$$

By this way, the condition that must be met for the capture of radiation into the capillary transmission mode to be effective is

$$\theta_{max} \leq \theta_c \quad (5)$$

Since the radiation power transmitted by a single capillary is very small because of the small aperture, to increase the aperture it's necessary to use a system of closely packed capillaries. When the packing is dense, the system consists of many capillaries arranged in layers around a central capillary. In the case of focusing capillary optics, each layer has its own curvature. The curvature varies from zero for the central channel to a certain limiting value determined by the parameters of the system and source.

In the simplest case, a monocapillary, the angular aperture at its entrance, Fig. 5a, is equal to  $\Delta\phi_m \propto \theta_c \ll 1$ . By this consideration, the power transmitted is  $W_m \propto \theta_c^2 T_m$ , where  $T_m$  is the transmission coefficient, which depends on the geometrical parameters and manufacturing of the monocapillary.

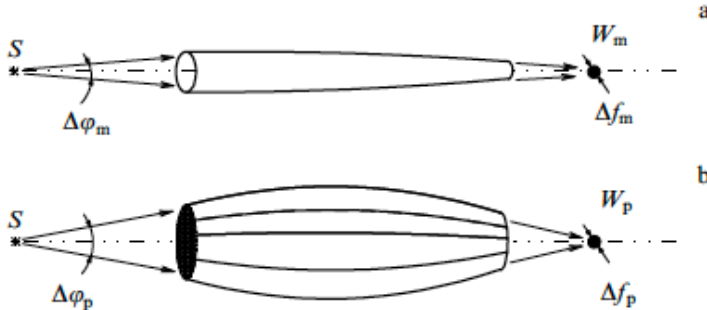


Figure 5: *Focusing X-rays by (a) a monocapillary and (b) a system of capillaries (S is the source of X-rays, and  $\Delta f$  is the size of the focal spot), from <sup>28)</sup>.*

The efficiency, in terms of intensity flux, can be increased by using polycapillary systems (Fig. 5b). Thanks to the construction geometry of a packed

capillary system, the entrance angular aperture of a polycapillary system may be much larger than the critical TER angle and equal to  $\Delta\phi_p \propto \theta_c$ , increasing the transmitted radiation power as  $W_p \propto (\Delta\phi_p)^2 T_p \gg W_m$ , where  $T_p$  is the transmission coefficient of the polycapillary system, usually  $\gg 10\%$ . A polycapillary system designed in a certain way makes it possible not only to effectively transmit radiation but also to increase the radiation density  $w \sim W/(\Delta f)^2$  by focusing the radiation to a spot of size  $\Delta_f$ , Fig. 5:

$$w_p \propto \frac{\pi}{4} (\Delta\phi_p^2) \frac{T_p}{(\Delta f_p)^2} \quad (6)$$

Since the radiation density at a distance  $L$  from the source is inversely proportional to the distance,  $w_0(L) \propto 1/(4\pi L^2)$ , the use of a capillary lens makes it possible to achieve the following gain in radiation density (for a more detailed and complete review see 28):

$$G \left( \frac{w_p}{w_0} \right)_L = \left( \frac{L\Delta\phi_p}{\Delta f_p} \right)^2 T_p \quad (7)$$

#### 2.1.4 Micro Channel Plates

A particular shape of channel optics are the Micro Channel Plates (MCPs), Fig. 6a. As for polycapillary optics, MCPs also focus X-rays by reflection from the inside surfaces of the channels. However, because of the channels' dimensions, MCPs are the simplest possible case of "point-to-point" focusing, Fig. 6b. The image is formed at the same distance from the plate as the source and the picture can be extended into two dimensions to allow focusing of a point source by an array of square or circular channels such as an MCP, with the rays reflected twice. The MCP, however, focuses not every ray perfectly - a ray can go straight through a channel without reflection, so ending up either above or below the focus, causing a diffuse halo around the image, like in the lobster eye X-ray lens. Moreover, a ray can be reflected only once, so this ray will be focused in one-dimension only and consequently ending up somewhere along a line through the focus. This causes a cross-like image centered on the focus.

An important modification occurs if the MCP is slumped to a spherical shape of radius  $R_{slump}$ , then it can be used to focus parallel rays to a point and/or to generate a parallel beam from a point source, Fig. 6c 30).

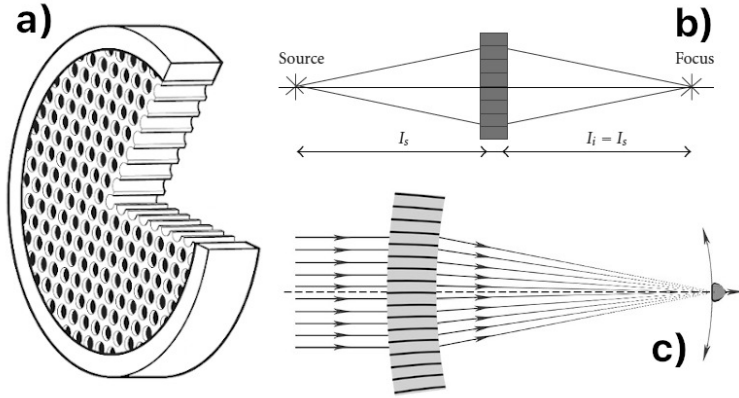


Figure 6: *Multi Channel Plates. a) Schematic structure of MCPs. b) The principle of MCPs X-ray Optics. c) Experimental layout for focusing X-ray beam: primary parallel beam, spherical bent MCPs and focused X-rays, from 30).*

## 2.2 Diffractive optics

Diffractive optics are phase relief elements that use micro-structures to alter the phase of the light propagated through them, and thus manipulate it. By this way, Diffractive Optical Elements (DOE) are devices that make use of the wave nature of light, modifying the phase of the propagating light by slowing it down in some areas of the beams vs. others. This allows shaping the beam using diffraction effects, in various ways to create shapes and light patterns that are impossible to achieve in different methods using refractive optics. The way a DOE changes the phase of the beam propagated through it is obtained by using micro structure patterns fabricated onto a substrate material. Photons that passed through the sunken areas in the diffractive element moves faster than light that goes through the higher areas (as in the case of light speed that is faster in air than in the material), creating a controlled phase delay<sup>31</sup>).

In the X-ray energy range, the most common and used DOE is the Fresnel Zone Plate (FZP), Fig. 7. ZFPs, commonly circular diffraction gratings consist of a series of concentric rings of radius  $r_n^2 = n\lambda F$ , where the rings become narrower at larger radii until the last, finest zone of width  $\Delta r_n$  is reached

(Soret approximation <sup>32</sup>). The focusing capability is based on constructive interference of the wavefront modified by passage through the zone plate. The wavefront modification is obtained through the introduction of a relative change in amplitude or phase in the beams emerging from two neighboring zones.

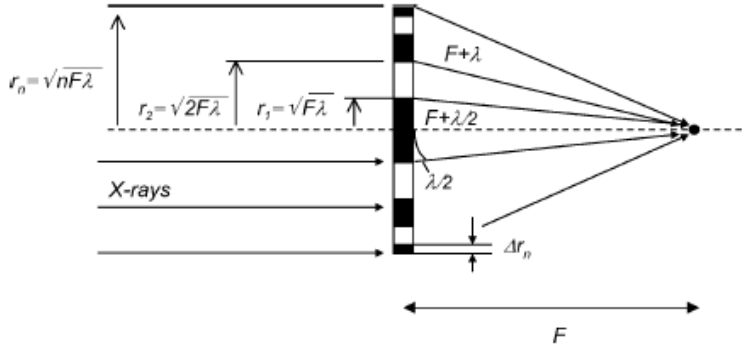


Figure 7: *Fresnel Zone Plate* <sup>33</sup>).

As for a light microscope lens, the Rayleigh resolution of a FZP is determined by its maximum diffraction angle  $A_n = \lambda/(2\Delta r_n)$ , approximately  $1.22\Delta r_n$ . Moreover, solving the path difference between an axial ray and ray at  $r_n$ , gives a more accurate definition of  $r_n$ , as

$$r_n^2 \approx n\lambda F + \frac{(n\lambda)^2}{4} + \dots \quad (8)$$

where the second term is the spherical aberration correction and it is significantly important when  $n \sim 4F/\lambda$ , i.e. a zone plate with a large numerical aperture. As an example, we should consider a zone plate  $80 \mu\text{m}$  in diameter with a  $20 \text{ nm}$  outer zone width (common geometric parameters for a FZP). For soft X-ray, the spherical aberration correction causes a  $\sim 30 \text{ nm}$  change in the radii of the outer zones, that is absolutely comparable with the  $20 \text{ nm}$  outer zone width.

As FZP is a diffractive optical element, this kind of optics mostly has more than one diffraction order, leading to more than one focus point, Fig 8 left side. In general, the behavior of FZP positive diffraction orders is to

produce a convergent beam, while negative diffraction orders even result in diverging beams as a dispersive lens with virtual focus points. When a FZP is used as focusing lens, normally only the first diffraction order is used and all other orders have to be blocked by a suitable aperture, called order sorting aperture, Fig. 8 right side.

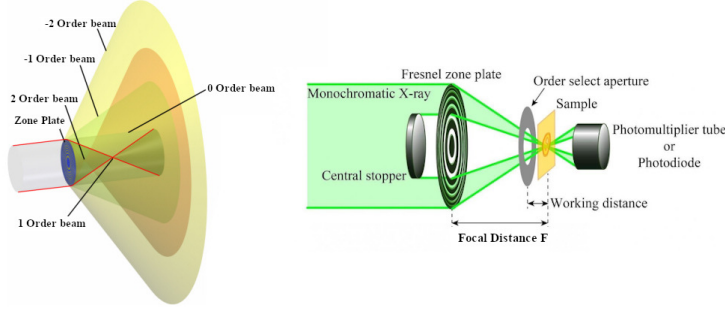


Figure 8: *Diffraction orders of a circular FZP (left); on the right, schematic optical setup with order sorting aperture, in order to select the diffraction order, and central stopper, for Soret approximation (right).*

The diffraction efficiency  $\epsilon_m$  of a FZP used in the  $m^{th}$  diffraction order is defined as

$$\epsilon_m = \frac{I_m}{I_0} \quad (9)$$

with the incoming intensity  $I_0$  and the intensity in the  $m^{th}$  diffraction order  $I_m$ . For  $m = 1$  commonly the efficiency values is in the range of 20 ÷ 50%, obtained with Ni based FZP and 7 keV energy beam <sup>34</sup>).

### 2.3 Refractive optics

Up to twenty years ago, refractive optical devices, which are extremely used in visible light, were generally considered inappropriate for focusing X-rays, as refraction effects are extremely small and absorption is strong. Up to the middle of 90's, refraction index for X-rays,  $n = 1 - \delta - i\beta$  where  $\beta$  is the absorption index and  $\delta$  is the refractive index, differs from unity by only a factor of  $10^{-5} - 10^{-7}$  while the  $\beta$  absorption index is high making diffractive

optics unusable. However, in 1996 it was shown that with low-Z materials, refractive optical devices can focus X-ray beams <sup>8)</sup>.

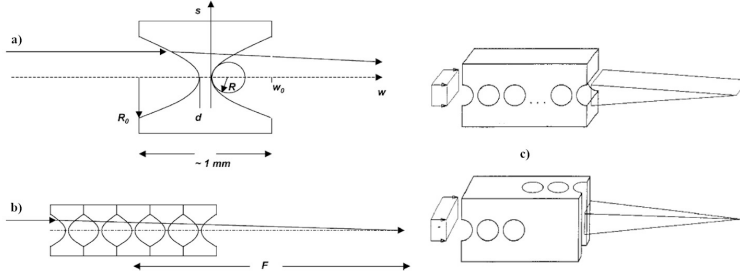


Figure 9: *Parabolic compound refractive lens (CRL). A single optical device (a) and stacked behind one another to form a CRL (b) <sup>33)</sup>. CRL for two-dimensional focusing in crossed geometry (c) <sup>35)</sup>.*

Since the  $(1 - \delta)$  in the index of refraction is smaller than 1, optics must have a bi-concave shape obtained by drilling a hole in the material, Fig. 9a. However, as  $\delta$  is very small for low-Z materials, lens radius should have dimensions in the order of micron size. To overcome this technical limitation, it was proposed to realize a Compound Refractive Lens (CRL), consisting of a linear array of many simple lenses manufactured in low-Z material (as carbon, boron or aluminum). A single lens has a focal distance of  $F = R/2\delta$ , where  $R$  is the lens radius. Considering  $N$  holes, CRL has the focal length  $F = R/2N\delta$ , Fig. 9b. To reduce spherical aberrations, the holes have parabolic profile  $s^2 = 2Rw$  where  $R$  is the radius of curvature at the apex of parabola. A lens with thickness  $2w_0 + d$  (where  $w_0$  is the dimension of the hole and the the thickness of the material between two holes) has an aperture  $2R_0 = 2\sqrt{2Rw_0}$ . As the drilling hole is axially symmetric (cylindrical or double parabolic shape), CRLs can only deflect the beam in one direction. By this way CRLs are actually realized in cross geometry layout, where two arrays of holes have perpendicular axis, allowing the possibility to manipulate the beam in both directions, Fig. 9c.

Unfortunately, since the index of refraction depends on the X-ray energy, refractive lenses are chromatic and this substantially limits their applicability. Therefore there is a strong demand for the development of energy tunable refractive optical systems when X-ray energy can be tuned in a reasonable

range without changing the beam position on the sample. In case of saw-tooth refractive lenses, it is easily possible to tune the energy by changing the gap between lenses <sup>36, 37</sup>).

### 3 XLab Frascati @ LNF

For the last 20 years, at the Laboratori Nazionali di Frascati (LNF-INFN) a team of researchers has been focused on the study of X-ray optics, in particular polycapillary optical elements, being involved in several national and international projects and collaborations. This research line has resulted in the establishment of a new dedicated laboratory, XLab Frascati (*XlabF*), which is also focused on the application of these optics for X-ray analysis in various fields, such as cultural heritage, innovative materials, medical diagnostics, pharmacology, beam diagnostics, detectors characterization, etc. The laboratory activities aim in particular to deeply study optics and evaluate various experimental schemes for different X-ray applications such as X-ray diffraction (XRD), X-ray fluorescence (XRF and TXRF - total reflection X-ray fluorescence) and X-ray imaging. The final result of our studies is the design and development of various instrumental prototypes and new X-ray desktop facilities for advanced techniques.

Actually, the INFN team has the knowledge and availability of four facility stations (RXR, XENA, PXRDS and CTS) that are normally open to external users: their combined work allows optimizing and matching the various analysis, while one more station is actually in realization and in commissioning (Soft X-ray Fluorescence). In more details, the facilities available are:

1. XENA (X-ray Experimental station for Non-destructive Analysis);
2. RXR (Rainbow X-Ray);
3. PXRDS (Powder X-ray Diffractometer Station);
4. CTS (Computed Tomography Station);
5. SoX (Soft X-ray Fluorescence).

In the following, we present a concise review about the XlabF facilities in correlation with some representative experimental results.

### 3.1 XENA

Started as a unique experimental station, it was used for all the different X-ray analysis performed at the laboratory. Operative and equipped with three X-ray Oxford Apogee tubes (W, Mo and Cu anodes), a set of mechanical components and motors for lens alignment and scanning, and an optical table providing many geometrical setup possibilities, XENA is a facility dedicated exclusively to imaging, tomography<sup>38)</sup> and characterization of X-ray devices such as novel sources<sup>39)</sup>, optics<sup>40)</sup> - diffractive crystals<sup>41)</sup> and vibrating optics<sup>42)</sup> - and detectors<sup>43, 44)</sup>.

In the past,  $\mu$ XRF punctual measurements were carried out by combining one of the three X-ray tubes with a polyCO full-lens having an Input Focal Distance (IFD) of 56.5 mm, an Output Focal Distance (OFD) of 44 mm, a length of 12 cm, and a focal spot size of 100  $\mu$ m. The tubes work at a maximum voltage of 50 kV and current of 1 mA. Changing the geometry setup, and by means of a CCD camera for the system alignment, total reflection XRF analysis for low concentration samples can be performed. Preliminary studies have allowed to reach detection limits under 10 ng for 10 elements (Si, Cl, Ar, K, Ca, Ti, Cr, Mn, and Fe)<sup>45)</sup>, Fig. 10.

Since the installation of RXR, a dedicated setup for XRF - see below, XENA facility was utilized only for Imaging, Tomography and advanced studies for novel sources, detectors and optics. A great result was obtained using  $\mu$ -Tomography to reconstruct the first 2/3 mm of spray coming out of a nozzle. Experiments on sprays are generally performed by means of non-intrusive diagnostic techniques to not interfere with the process. Typically, conventional optical techniques using light sources from near ultraviolet (UV) to infrared (IR) wavelength region (180-900 nm) are applied. Global morphology measurements concerning both liquid and vapor phases can be obtained. Scattering techniques coupled with high speed cameras allow characterizing the main jet geometric parameters such as the tip penetration and the cone angle, while vapor phase is investigated through refractive-index gradient-based techniques such as shadowgraphy. All these techniques provide useful information about the vapor-liquid fraction and their time evolution. However, there are strong limitations concerning the inner structure investigation due to the high liquid density near the nozzle spray and in the core of the jet. In these areas both absorption and multiple scattering effects of the incident light prevent

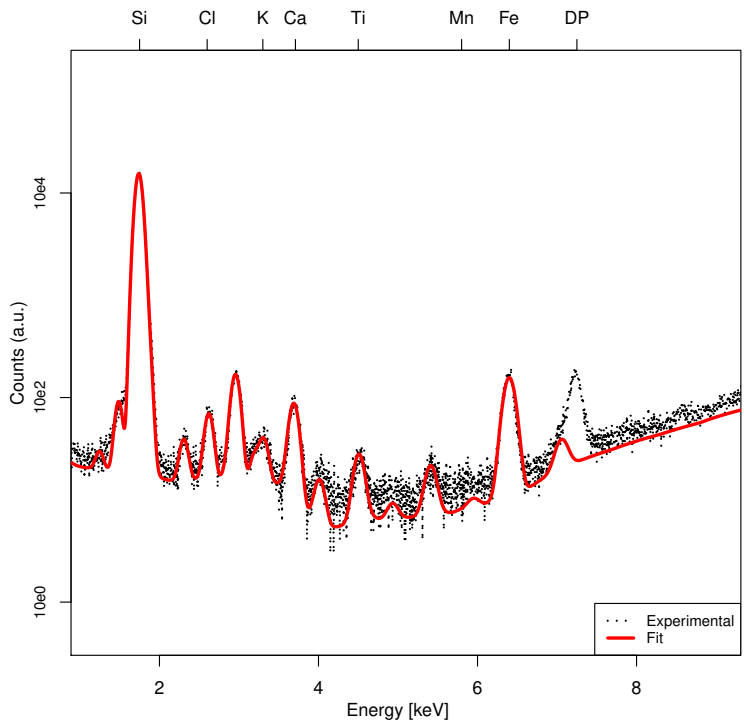


Figure 10: *TXRF spectrum of insoluble dust from an Antarctic ice core.*

this approach restricting it to low-dense areas typically surrounding the spray. Measurements on the internal features of a spray are fundamental to characterize the break-up of the fuel occurring at the nozzle exit and influencing the whole spray development.

Due to the weak interaction of X-rays with fluids, as engine fuels, the radiation can penetrate the sprays structures and provide spatially-resolved information along the propagation direction. In the 80's, first studies on dense sprays by X-ray absorption techniques have been tested, when the mass distribution of the liquid phase in a water/gaseous nitrogen spray was estimated using X-ray absorption method <sup>46</sup>). Recently, Synchrotron Radiation absorption-based techniques have been applied to investigate high-dense regions of the

sprays providing quantitative measurements of the mass. X-rays penetrate the dense part of fuel spray because of their weak interaction with the low Z hydrocarbon chain, obtaining radiography and tomography to investigate the sprays and to reconstruct the three-dimensional (3D) structure.

The use of polycapillary lenses has allowed to overcome lower energy, high divergence and time-continue structure beams limitations in order to obtain high-intense quasi-parallel beams with a 60% transmissivity. In collaboration with the former Istituto Motori - CNR (now STEMS-CNR), XlabF team studied a GDI 6 hole injector with  $\mu$ CT technique in order to determine the inner structure of dense sprays just outside the tip of the injector, for all the details see [38]. The injection apparatus consisted of a pneumatic pump activated by a pressured gas, a multi-hole injector for gasoline direct injection and a programmable electronic unit for pulses control. The spray has been injected at 12.0 MPa pressure and 4 Hz frequency in a transparent Plexiglas vessel at atmospheric back-pressure and ambient temperature. The oil was delivered by a solenoid-actuated 6 hole GDI injector (0.193 mm hole diameter). The experimental setup, which includes X-ray source and polycapillary optics (left side) and GDI injector mounted on the bottom of the rotating stage (right side), is shown in Fig. 11a.

Fig. 12 reports both fuel density and X-ray absorption distributions in the jet longitudinal plane. X axis refers to the jet cross-section, while y axis is normal directed to the nozzle. The radiation absorption is a function of the crossed fuel mass, and its estimation becomes useful to better understand the jet profile as well as the corresponding density distribution. At the nozzle hole exit, the absorption immediately raises due to the combined effect of the increase of both cross-section radius and density, up to the maximum at the distance of about 1200  $\mu$ m from the orifice. The related density profile shows a maximum just out of the nozzle.

As known, the density of a sample is related to the absorption through the attenuation coefficient as well as the crossed mass section radius. Considering the camera spatial resolution, the data corresponding to a distance lower than 150  $\mu$ m from the nozzle are not considered for quantitative measurements even if reported in the graph. At 150  $\mu$ m from the nozzle the maximum value of 110.5 kg/m<sup>3</sup> has been detected. In this selected region, just outside the injector, the air-fuel interaction is significant only on the spray edge. Later on,

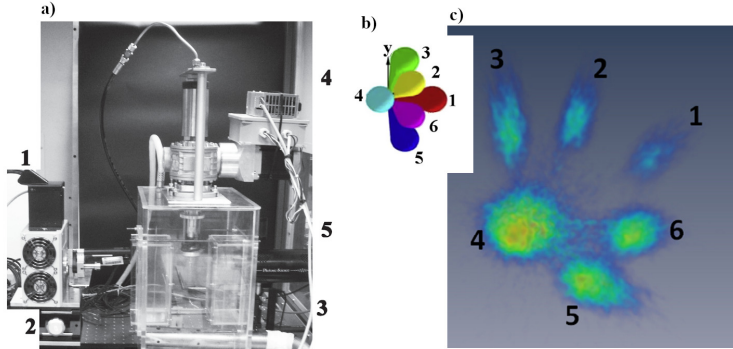


Figure 11: a) X-ray  $\mu$ CT experimental setup for 3D tomography of GDI spray. (1) X-ray source, (2) polycapillary optics, (3) nozzle injector, (4) rotative stage, (5) CCD detector. b) Sketch of spray from the GDI nozzle and jets position referred to the nozzle axis in the  $xy$  plane. c) Top view of tomography picture of the six-hole GDI spray <sup>38</sup>).

the signal decreases due to the combined effect of growing spray section, loss of momentum flux and enhanced air-fuel mixing.

### 3.2 RXR

RXR is an experimental station at XLab Frascati <sup>47</sup>), dedicated for X-ray fluorescence studies based on the use of polycapillary lenses in a confocal geometry <sup>11, 48</sup>). The flexible RXR layout allows investigating specimens of the dimensions ranging from several millimeters up to half meter and weighting up to several tens of kilograms. Compared to similar existing XRF stations, apart from the possibility for investigating large samples, the main advantage of this equipment is the detection system with two spectrometers optimized to work separately at high and at low X-ray energies. The confocal geometry combined with a 3-axes fine motion system makes possible 3D  $\mu$ XRF elemental tomographic acquisitions (colour tomography). At present this station in operation at high XRF energies is used for cultural heritage and geological applications.

The RXR unit is a rather compact experimental apparatus dedicated to the research on 2D/3D X-ray micro-fluorescence ( $\mu$ XRF) spectroscopy. Its

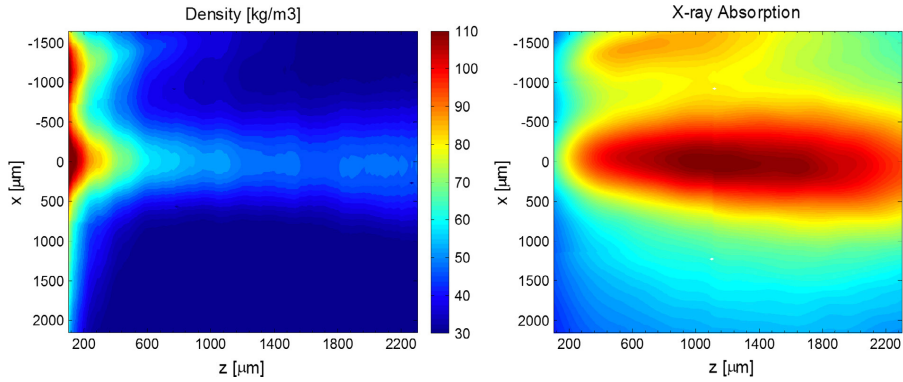


Figure 12: *Jet longitudinal plane distribution of fuel density (left) and X-ray absorption (right)* <sup>38</sup>.

main parameters are characterized by a probe size ranging from 70 to 80  $\mu\text{m}$  and by an excitation energy from 6 to 30 keV (the low energy can be optionally decreased to approximately 1 keV but not in confocal mode). The RXR setup is composed by two dedicated polycapillary optical elements. A full-lens focuses the incident beam to the sample position, while the second one optimized for the energy range of 6-30 keV concentrates the fluorescent radiation onto the detector.

The experimental layout of the station includes a focusing polycapillary lens with a 90  $\mu\text{m}$  FWHM spot size matching the Mo X-ray tube (Oxford Apogee 5000), a detector combined with a dedicated semi-lenses (from X-Channel Techn.), an alignment system and an optical microscope with a CCD camera (Basler acA750-30gc). To align the sample in the vertical plane and to scan the surface we use a laser profilometer with a spatial resolution of 10  $\mu\text{m}$  (Microspilon NCDT 1401). The software adopted for control instrumentation and data acquisition is based on LabVIEW.

To perform the confocal geometry capabilities as well as to discriminate volumes characterized by different densities and composition, a soft solid sample with metallic inclusions was investigated, defined by a screw encapsulated in a drop of ethanol and methyl acetate glue. Unlike a classical tomogra-

phy approach (CT scan), 3D- $\mu$ XRF reconstruction has been performed collecting 2D scans on different sections along the axial direction. In this analysis, a total volume of  $4.1 \times 4.1 \times 2.1 \text{ mm}^3$  was probed with a step of  $100 \mu\text{m}$  ( $\Delta x = \Delta y = \Delta z = 100 \mu\text{m}$ ) and acquisition period of 5 sec/step.

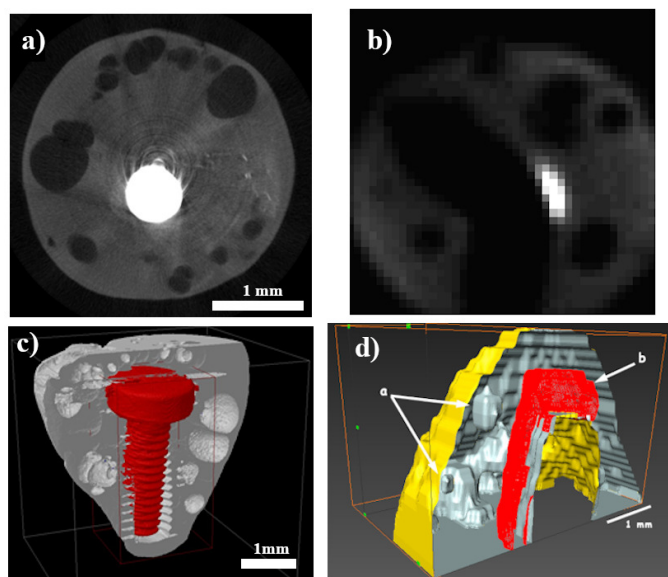


Figure 13: a) reconstructed tomographic slice by a semi-lens  $\mu$ CT setup of a screw encapsulated in organic glue; b) 2D scan by confocal  $\mu$ XRF on a specific  $z$ -axis position for the same sample. Image refer a layer showing three different regions: a high fluorescence area due to the presence of the metal screw, a region associated to the primary radiation scattered by the glue and a signal-free region - air bubbles; c) 3D reconstruction section for a PolyCO  $\mu$ CT system - the screw part is visualized using red color and glue part using grey; d) 3D reconstruction by confocal  $\mu$ XRF analysis, where the arrows a) and b) identify two air bubbles trapped during the hardening process of the glue.

In order to make a comparison with the results from another X-ray technique, a PolyCO based  $\mu$ CT scan was performed. Using a semi-lens a quasi-parallel beam was obtained characterized by output divergence about 1.4 mrad. The beam transmitted by the sample was detected by a Photonic Science CCD camera, placed 15 mm behind the sample. The detector has a sensitive area

of  $14.4 \times 10.8 \text{ mm}^2$  with a pixel resolution of  $10.4 \times 10.4 \text{ }\mu\text{m}^2$ . Projection images are recorded for a full turn ( $360^\circ$ ) with a  $0.25^\circ$  angular step. The time per projection equals 1.2 seconds when the semi-lens is used and 5 seconds if not, that means a reduction of exposure time 4 times greater. In Fig. 13a it is shown one of the  $z$ -axis reconstructed slice, while in Fig. 13c the 3D rendering based on the reconstructed tomography slices<sup>49, 11</sup>). Due to the high difference contrast between soft materials and metals, it was possible to identify the screw (in red) encapsulated in organic glue.

The test sample described was investigated using the *RXR* facility in a confocal scheme: a full lens combined with an X-ray Mo tube and a semi-lens combined with a spectral X-ray detector. Using a special motorized stage, it was possible to move the object under study in three dimensions relatively to the confocal point of the lenses, thus providing the analysis of the secondary X-ray emissions from each selected point, allowing a point-by-point for every layer image. In Fig. 13b is shown one of 2D  $\mu\text{XRF}$  scan (of a total of 21 layers in  $z$ -axis direction). Each pixel of this image is an integral of the spectrum registered by the X-ray detector for each particular point<sup>49, 11</sup>). Starting from the screw in two directions, two shadows are formed and caused by the total absorption of the X-ray corresponding to the X-ray tube or detector directions.

Compared to tomography, the 3D  $\mu\text{XRF}$  technique allows the recognition of specific elemental contributions. As an example, in Fig. 10d a 3D rendering with the iron contribution outlined in red (b), the external surface of scattered beam (yellow) and the internal surface of the sample (grey) are showed. This *elemental* visualization, with a spatial resolution of  $\sim 100\mu\text{m}$ , clearly highlights the presence of bubbles formed in the hardening process of the glue.

The starting conceptualization of *RXR* was to realize an instrumentation dedicated for Cultural Heritage applications. Up to now, a lot of external teams, from universities to museums, utilized *RXR* for archaeological purposes. In the following an important study of ancient scrolls will be reported. In collaboration with University of Rome Tor Vergata, the Casanatense Library, the Ragusa Foundation and the Pigorini Museum, the ink present in few ancient scrolls was studied, Fig. 14. The objective of the work was the determination of chemical components of the inks present within several areas of two different sample typologies from an ancient manuscript and some Buddhist scrolls<sup>50</sup>), in comparison with Fiber Optics Reflectance Spectroscopy (FORS). As XRF is

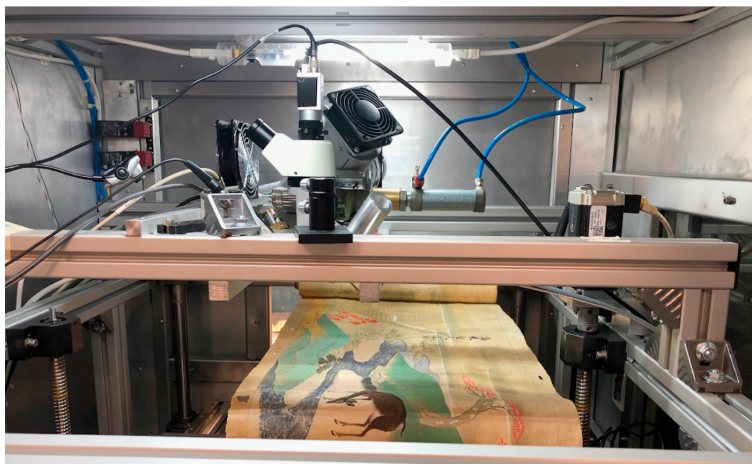


Figure 14: *The Engi Jizo Emakimono Coll. Ragusa n.142 838 scroll under study inside the RXR experimental setup.*

a unique tool for element analysis, RXR employed allowed punctual analyses and chemical characterization of the colours also where the pigments powder was inhomogeneous. The complementarity of these methods allowed to obtain the colour characterization of the investigated scrolls and the identification of the pigments, which are coherent with the historical-artistic period of the handscroll.

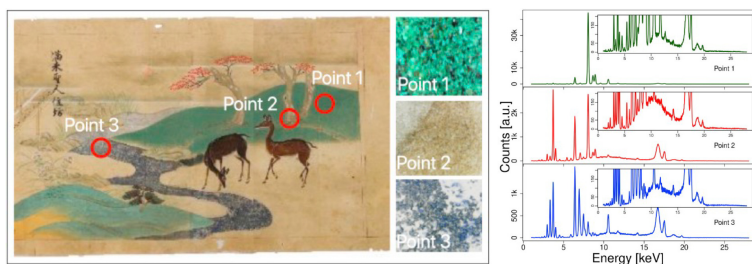


Figure 15:  *$\mu$ XRF spectra of the sampled points obtained by RXR.*

The pigments identification by FORS was confirmed by  $\mu$ XRF analyses

(Fig. 15 where the sampled points and the related XRF spectra are analyzed <sup>51</sup>). In particular, the Fundamental Parameter Method (FPM) was applied to estimate the concentration (in %) of the chemical elements, Fig. 16, obtained by  $\mu$ XRF with the purpose of assessing the existence of a stoichiometric ratio, among the elements, which could confirm or not the presence of a specific pigment.

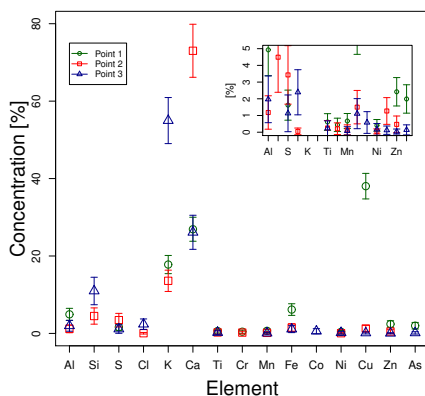


Figure 16: Concentration of chemical elements from the sampled points obtained by analysing the XRF spectra with the FPM approach.

### 3.3 PXRD

The third permanent experimental setup is the Powder X-ray Diffraction Station (*PXRD*S), a  $\Theta/2\Theta$  Seifert - XRD 3003 diffractometer <sup>52</sup>). The instrument has a remarkable mechanical stability, high precision and a variety of possible configurations. The diffractometer is a 2200W Power System with a  $\text{CuK}\alpha$  anode target, 1x12 mm beam, while the goniometer, placed in a vertical position, has a high precision thanks to the use of stepper motors with microstep movement which ensures an angular resolution greater than  $0.001^\circ$ , Fig. 17.

Designed and realized for the beamline BX1 in ADONE Accelerator at the end of 80', this experimental setup was removed from the line when the accelerator was turned off to build Dafne. Equipped with a new power supply

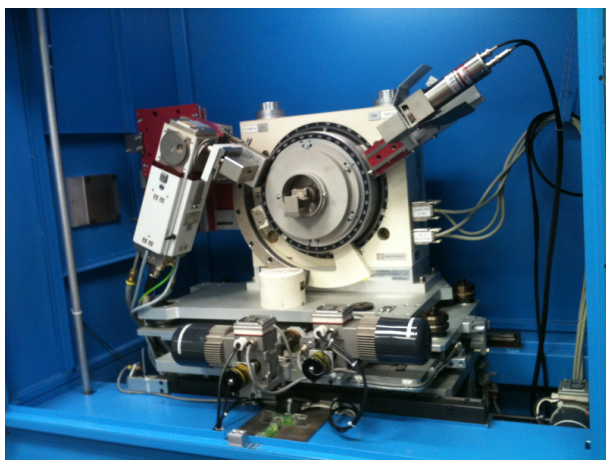


Figure 17: *PXRDS facility.*

and a conventional X-ray source, PXRD was utilized in several application fields, like cultural heritage, geology, pharmacology, new materials leading to the publication of a huge number of scientific papers.

One of the last application where PXRD was utilized is in the restoration chemistry for cultural heritage. A team from University of Tor Vergata realized a procedure for restoration and preservation of paper, proposing a biocompatible method to perform wet cleaning on paper based on the use of ultrasound in combination with water-dispersed polyvinyl alcohol microbubbles<sup>53</sup>). Paper samples inevitably degrade over time, depending on several factors (intrinsic composition, presence of additives and adverse environmental conditions, etc...), due to the fact that cellulose, paper's main component, is prone to deterioration through hydrolysis and/or oxidation reactions. By this, hydrolysis processes lead to fragile paper, while oxidation induce yellowing and a loss of readability of both the text and the artistic contents. The use of synthetic polymers to obtain hydrogels and microsized systems has been pointed out to overcome limitations imposed by natural procedures (for example water bath or natural gels) and to improve some of their useful features in the cultural heritage preservation field. Polyvinyl alcohol (PVA), in particular PVA microbubbles (PVAMBs) which is able to form stable chemical hydrogels and

microgels, demonstrated to show excellent compatibility with cellulose-based supports and good cleaning efficiency for both ancient and modern paper samples <sup>53</sup>).

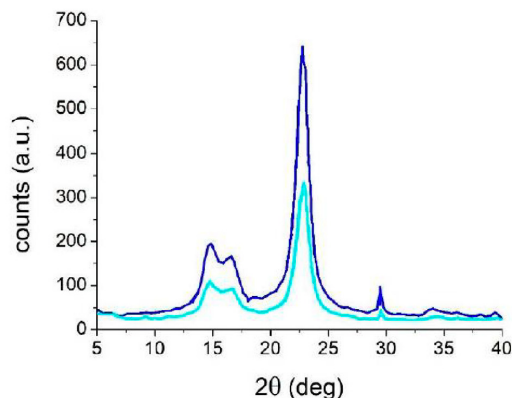


Figure 18: Diffraction pattern of *Breviarium* paper samples before (blue) and after treatment (light blue) <sup>53</sup> .

Since PVAMBs are acoustically active, thus representing a versatile tool to enhance the cleaning action with Ultrasound (US), the Tor Vergata team proposed the combined use of microbubbles and US for selective removal of a coating from a delicate substrate. The first restored ancient paper is a *Breviarium* ("Breviarium Romanum ad usum fratrum" belonging to the XVIII century, from a private collection), for the removal of cellulose degradation byproducts. However, US treatments already reported in the literature (see <sup>53</sup>) for details) warns about the potential mechanical damage they produce by thermal damage onto cellulose fibers. In this context, to study the excessive microstreaming flows and cavitation hotspots, and therefore, cellulose degradation, XRD analysis were performed to investigate the possibility of paper weakening induced by the PVAMB/US treatment. In the diffraction patterns of both treated and not treated *Breviarium* samples, in the 110-25° range, the peaks attributable to the (10 $\bar{1}$ ) plane and to the (00 $\bar{2}$ ) plane of the structure of cellulose I type  $\beta$  are present (PDF-card 3-289), Fig. 18. The XRD results demonstrated that the PVA microbubble coupled with US treatment was able to remove the

degradation without affecting the crystalline structure of the cellulose.

### 3.4 CTS

The station for micro tomography (CTS) was realized and completed in 2022, by following and satisfying the regulations in terms of safety requirements necessary for X-rays up to 100 keV, Fig. 19. CTS was designed and realized for very high resolution imaging and for high precision tomography. Developed as part of a project funded by the MIUR, the station, equipped with a micro-focusing source ( $5\ \mu\text{m}$  on the anode), high precision mechanics and high-resolution CCD detector ( $10.4\ \mu\text{m}$  per pixel), is able to reach a resolution of 600-700 nm per voxel through the phase retrieval technique. CTS is currently in the installation and commissioning step.

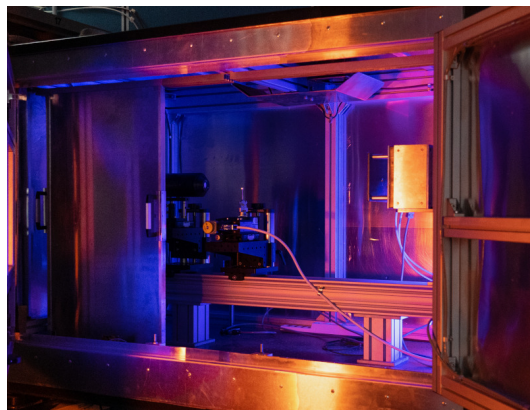


Figure 19: *CTS Experimental layout.*

CTS facility has been specifically designed with the purpose of operating either in absorption or in phase-contrast mode. Moreover, thanks to the know-how of XlabF team, a possible optional configuration is to use PolyCO in fast tomography of dynamical process. As a first result, in Fig. 20 it is shown a phase contrast radiography of organic sample entrapped in amber ( $R_1$  is the distance between the source and the sample while  $R_2$  is the distance of the sample from the detector). By phase propagation, the edge enhancement effects are clearly visible.



Figure 20: *Phase contrast and phase retrieval radiography for organic sample entrapped in amber. The source parameter are 40 kV, 50  $\mu$ A, 5  $\mu$ m anode focus, distance  $R_1=30$  mm, distance  $R_2=750$  mm and Time acquisition of 1min 30s.*

### 3.5 SoX

The Soft X-ray fluorescence station is the new fluorescence station for the study of organic materials, and it is actually under construction, Fig. 21. The main characteristics of this instrument are the high vacuum chamber, the 6-axis manipulator for positioning and a windowless detector necessary for detection of low atomic number elements, such as Carbon, Oxygen, Nitrogen and Fluorine.

### 3.6 Vitruvio OS

Since from its foundation to nowadays, the XlabF laboratory has acquired several instrumental devices that need to be managed through a dedicated framework system enabling also the remote access, when necessary. As a result, we designed and developed *Vitruvio*, based on a LabVIEW platform that allows a complete control of one or more experimental devices in parallel.

The central system core is the *operative units*, composed of generic applications dedicated to the different tasks assigned to them through JSON format. The units are divided into four groups: Admin, COM, analysis and FE (front end) as shown in Fig. 22.

First, the *Admin* class units receive commands from users, that are subsequently processed and finally sorted with the purpose of allocating each action



Figure 21: *SoX station - vacuum chamber.*

to the adequate level of allocation. Since the communication protocols between the various units are based on the JSON language, the user interfaces do not necessarily have to be on the LabVIEW platform, but can be completely generic. The Analysis units contain all the analysis algorithms, that in our case are all algorithms for spectroscopic, diagnostic and characterization studies.

The *FE* class units are the interface with the hardware present in the laboratory. Thanks to the modularity of the units, we have the possibility to insert any device at any time, as in the case of a detector, a source or a remote movement control. Moreover, thanks to the JSON format, the hardware itself does not necessarily need or request a driver specifically written in LabVIEW language.

Finally, *COM* class units are used for managing and interfacing with storage and database systems. One unit in particular is dedicated to a separate operation: the *ART* unit is a matrix of information of the current state of the

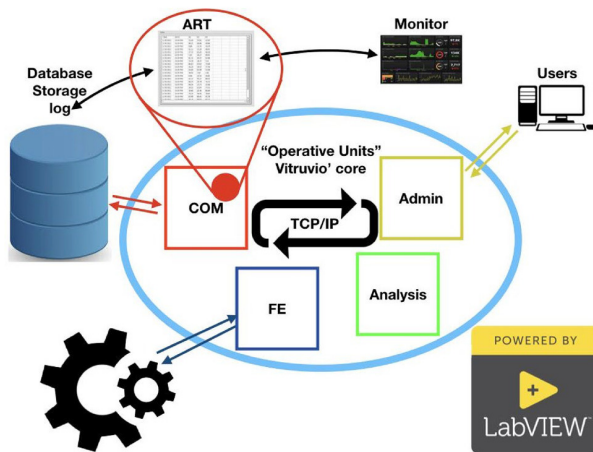


Figure 22: A schematic of the Vitruvio layout, comprehending the four units and their interaction with external elements.

operating system, i.e. all the other units, and this matrix allows us to process a log (event log) and to view it on a control monitor. This is particularly useful in case of critical events to be evidenced and solved.

Therefore, Vitruvio, although it was conceived for the management of all the running systems of XlabF, is a definitely generic management system that is adaptable to all the needs of an automatized framework in a lab where instrumentations and machines work independently and in parallel at the same time.

### 3.7 X-Channel Technologies

The XlabF laboratory currently is the unique Italian laboratory dedicated to the design, manufacture and characterization of X-ray and neutron polycapillary optics, Tab 2. Presently, XlabF represents one of the few facilities all over the world able to realize polycapillary optics, thanks to the presence within the INFN National Laboratories of Frascati of the XChannel - Technological Polo, dedicated to the whole production chain, ranging from fabrication of the lens/semi-lens from raw materials to the characterization of the final product. This was made possible thanks to the agreement signed by Prof. SB Dabagov

with the Unisantis FZE for the acquisition of all the intellectual rights covering the production of the PolyCOs, and including both the know-how and the industrial apparatuses. In addition, given the expertise and established know how of the XlabF researchers about polycapillary production, we are able to design and produce customised optics according to the users' experimental requirements.

		Reflective			Diffractive		Refractive
		Kirkpatrick-Baez	Channels Structures	Waveguides			
		Mirrors	PolyCO	Capillaries	Zone Plates		Refractive Lens
		Kirkpatrick Baez, 1948 3)	Kirger et al. 1948 20)	Balaic et al. 1995 21)	Baez 1952 23)		Snigerev et al. 1996 8)
		Underwood Barbee, 1986 19)	20-80 $\mu\text{m}$ 11)	< 1 $\mu\text{m}$ (SR) 12)	40 nm (SR) 13)		2nm (SR) 15)
Spot Size	< 10 nm (SR) 9)	40 nm (SR) 10)	< 30 keV		< 30 keV		< 1 MeV
E	< 20 keV	< 100 keV			< 20 keV		
$\Delta E/E$	white beam	$10^{-2}$	white beam		$10^{-3}$		$10^{-3}$

Table 1: X-ray optics with principal characteristics.

Optics Typology	Focal data	Focal Spot Size	Size of single channel	Energy range	Transmission	PolyCO length
Full PolyCO	30-80 mm	30-80 $\mu\text{m}$	3-10 $\mu\text{m}$	4-40 keV	40-80% @ 8 keV	60-100 mm
Semi-lens PolyCO	30-80 mm	1-3 mrad	3-10 $\mu\text{m}$	4-40 keV	40-80% @ 8 keV	40-60 mm
Straight PolyCO	-	-	3-10 $\mu\text{m}$	4-40 keV	40-80% @ 8 keV	5-600 mm
Full MonoCO	30-80 mm	30-80 $\mu\text{m}$	20-40 $\mu\text{m}$	< 10 keV	-	60-100 mm
Semi-lens MonoCO	30-80 mm	-	20-40 $\mu\text{m}$	< 10 keV	-	40-60 mm
Full single capillary	30-80 mm	10-50 $\mu\text{m}$	3-5 mm	-	-	60-100 mm
Semi-lens single capillary	30-80 mm	-	3-5 mm	-	-	40-60 mm

Table 2: Typologies of polycapillary optics produced @XlabF and their characteristics.

## 4 Conclusions

This overview shows some and more significative optics dedicated to X-rays based studies, by reporting a brief description of reflective, diffractive and refractive optics. Thanks to the development of large laboratories, as Synchrotron Radiation Facilities, nowadays these optics are commercially available also for conventional sources in common laboratories.

The first optics applied to X-rays are KB mirrors, with an intrinsic advantage compared to other techniques, i.e. non-dispersive or broadband focusing. On contrary, Fresnel Zone Plates and CRL are in-line optics, that gives certain advantages versus KB-systems. On-axis optics do not change the beam direction, providing easy alignment and operation. Moreover, in case of nanofocusing geometry FZP and CRL should have greater clearance from the optics to the sample. FZP elements have attractive features as they are very compact and easy to use. The advantages of CRLs are: they are very robust and small, the focal length and size are adjustable by adding or removing individual lenses and the lenses can withstand high heat-load. The lens aperture can range from few microns to few millimeters. Their focal distances can range from a few millimeters to tens of meters, covering an energy range from 4 keV to 200 keV. Comparing different optics, it is of great interest to consider what is a physical limit to obtain an efficient focusing of hard X-rays. It was found that mirrors have a numerical aperture limited by critical angle of total reflection and the ultimate resolution limit is 10 nm, while for refractive optics this limit is slightly lower and 2 nm might be achievable. However, all these peculiarities are allowed only in SR facilities, reducing the possibility to manipulate efficiently X-ray radiation in conventional laboratories.

In contraposition, capillary optics has for the first time allowed to control efficiently X-ray radiation within a broad frequency range even with conventional sources. This kind of optics effectively turn the beam by large angles, transform a divergent beam into a parallel beam and vice versa and focus the radiation with an intensity increasing by a factor of 100 to 10000 and more, making capillary technique a real breakthrough in X-ray applications. In the last 2 decades, the use of capillary structures has greatly contributed to experiments in diffraction, in 2D/3D elemental analysis, in the production of high-power sources of X-ray radiation, and in many other areas.

As a dedicated laboratory to the study on X-ray optics and their ap-

plications, in this review we have outlined the latest and more reasonable results achieved at XLab Frascati by PolyCO combined with conventional X-ray sources. In particular, we have described all the facilities, open and available to the users and facilities that are in the commissioning phase, as well as the activities carried out by X-Channel Tech. for the design and realization of X-ray PolyCO.

## 5 Acknowledgements

One of the authors, S.B. Dabagov, would like to acknowledge the support received by the Competitiveness Program of the National Research Nuclear University MEPhI (Moscow).

## References

1. W. Fridrich, P. Knipping, M. von Laue, *Sitzungsber. Bayer. Akad. Wiss.* 303 (1912).
2. A.H. Compton, *Philos. Mag.* 45, 1121 (1923).
3. P. Kirkpatrick, A.V. Baez, *J. Opt. Soc. Am.* 38, 766 (1948).
4. H. Wolter, *Ann. Phys. (Leipzig)* 10, 286 (1952).
5. H. Mimura, H. Yumoto, S. Matsuyama et al., *Appl. Phys. Lett.* 90, 051903 (2007).
6. O. Hignette, P. Cloetens, C. Moraweey et al., *AIP Conf. Proc.* 879, 792-799 (2007).
7. D.H. Bilderback, S.A. Hoffman, D.J. Thiel, *Science* 263, 201-203 (1994).
8. A. Snigirev, V. Kohn, I. Snigireva et al., *Nat.* 384, 49 (1996).
9. X. Xu et al., *Optics Express* 30(15), 26761-26773 (2022).
10. K.T. Murray et al., *Optics Express* 27(5), 7120-7138 (2019).
11. D. Hampai et al., *JINST* 13, C04024 (2018).
12. R.A. Barrea et al., *J. Sync. Rad.* 16, 76-82 (2009).

13. A. Jarre, C. Fuhse, C. Ollinger et al., *Phys. Rev. Lett.* 94, 074801 (2005).
14. H.C. Kang, J. Maser, G.B. Stephenson, C. Liu et al., *Phys. Rev. Lett.* 96, 127401 (2006).
15. C.G. Schroer, O. Kurapova, J. Patommel et al., *Appl. Phys. Lett.* 87, 124103 (2005).
16. C. Bergemann, H. Keymeulen, J.F. Van der Veen, *Phys. Rev. Lett.* 91, 204801 (2003).
17. C. Schroer, B. Lengeler, *Phys. Rev. Lett.* 94, 054802 (2005).
18. V.V. Lider, *J. Surf. Invest.* 13(4), 670-682 (2019).
19. J. H. Underwood, T. W. Barbee and C. Frieber, *Appl. Opt.* 25, 1730-1732 (1986).
20. D.R. Kreger, *Rec. trav. bot. néerlandais*, 41, 603 (1948).
21. D. Balaic and K.A. Nugent, *Appl. Opt.* 34, 7263-7272 (1995).
22. Y.P. Feng, S.K. Sinha, H.W. Deckman et al., *Phys. Rev. Lett.* 71, 537-540 (1993).
23. A.V. Baez, *J. Opt. Soc. Am.* 51, 405-412 (1961).
24. A. Ohba et al, *Rev. Sci. Instr.* 92, 093704 (2021).
25. chandra.harvard.edu
26. xmm.esac.esa.int
27. M.A. Kumakhov and F.F. Komarov, *Phys. Rep.*191(5), 289-350(1990).
28. S.B. Dabagov, *Phys. Usp.* 46(10), 1053-1075 (2003).
29. F.F. Komarov et al. *Poverkhnost* 6, 31 (1986) and *Phys. Chem. Mech. of Surfaces* 5, 1360 (1990).
30. M.I. Mazuritskiy, A.M. Lerer, S.B. Dabagov, A. Marcelli, D. Hampai and K. Dziedzic-Kocurek, *J. Surf. Invest.* 13(6), 1005-1013 (2019).
31. V. De Andrade et al., *Adv. Mat.* 33(21), 2008653 (2021).

32. J.L. Soret, *Ann. Phys. Chem* 156, 99 (1875).
33. I. Snigireva and A. Snigirev, *J. Environ. Monit.* 8, 33-42 (2006).
34. E. Di Fabrizio et.al, *Nature* 401, 895 (1999).
35. A. Snigirev et al., *App. Opt.* 37(4), 653-662 (1998).
36. B. Cederstrom, M. Lundqvist and C. Ribbing, *Appl. Phys. Lett.* 81, 1399-1401 (2002).
37. S.D. Shastri, J. Almer, C. Ribbing and B. Cederstrom, *J. Synchrotron Rad.* 14, 204-211 (2007).
38. L. Marchitto, D. Hampai, S.B. Dabagov, L. Allocca, S. Alfuso, C. Polese A. Liedl, *Intern. J. of Multiphase Flow* 70, 15-21 (2015).
39. Nanoray, a portable X-ray machine, FP7 Project N 222426 (2008-2011).
40. D. Hampai et al., *Spectrochim. Acta B* 64 (11), 1180-1184 (2009).
41. G. Cappuccio, S. B. Dabagov, D. Hampai, Yu. I. Dudchik and F. F. Komarov, *Proc. of SPIE, Proc. of SPIE, Vol. 6634, 6634M* (2007).
42. A. Liedl, S.B. Dabagov, D. Hampai and C. Polese, *Nucl. Instr. Meth. B* 355, 289-292 (2015)
43. G. Cavoto, S. Dabagov, D. Hampai, G. Piredda, F. Renga, E. Ripiccini, C. Voena and A. Zullo, *JINST* 10, P03012 (2015).
44. F. Bonfigli, D. Hampai, S.B. Dabagov, R.M. Montereali, *Opt. Mat.* 58, 398-405 (2016).
45. D. Hampai, S.B. Dabagov, C. Polese, et al., *Spectrochim. Acta B* 101 (2014) 114-117 (2014).
46. H. Gomi and K. Hasegawa, *Int. J. Multiphase Flow* 10, 553-661 (1984).
47. G. Cappuccio, G. Cibin, S.B. Dabagov, A. Di Filippo, G. Piovesan, D. Hampai, V. Maggi and A. Marcelli, *Condens. Matter*, 3(4), 33 (2018).
48. D. Hampai et al., *Optics Letters* Vol. 33(23), 2743-2745 (2008).

49. Yu.M. Cherepennikov et al., JINST 13, C07003 (2018).
50. S. Ceccarelli et al., Scires-IT, 12(2), 109-118 (2022).
51. G. Cappuccio et al., Radiation Physics and Chemistry 188, 109660 (2021).
52. E Burattini et al., LNF preprint, LNF-91/014 (1991).
53. L. Severini et al., A. D'Andrea, M. Redi, S.B. Dabagov, V. Guglielmotti, D. Hampai, L. Micheli, R. Cancelliere, F. Domenici, C. Mazzuca, G. Paradossi and A. Palleschi, Gels 9(7), 509 (2023).

**SEEING TREES THROUGH X-RAYS: IMPLEMENTING FAST  
SCANNING OF LARGE SAMPLES TO UNDERSTAND PLANT  
BIOLOGY AND MONITORING ENVIRONMENTAL CHANGES  
IN TIME AND SPACE**

A. Di Filippo

*Dep. of Agriculture and Forest Science (DAFNE), Univ. Tuscia, Viterbo, Italy*

S.B. Dabagov

*INFN-LNF, XLab Frascati, Frascati, Italy*

*RAS P.N. Lebedev Physical Institute, 119991, Moscow, Russia.*

*National Research Nuclear University MEPhI, 115409, Moscow, Russia*

V. Guglielmotti

*INFN-LNF, XLab Frascati, Frascati, Italy*

D. Hampai

*INFN-LNF, XLab Frascati, Frascati, Italy*

**Abstract**

Plant diagnostics and phenotyping represent fast-advancing research frontiers, providing new knowledge on how plants respond to their environment. In vivo 3d imaging of plant functioning, anatomical traits and metallomics are among the most promising and quickly evolving fields in current basic and applied plant biology. Thanks to the long-term environmental information they store in annual wood rings, trees can be implemented as monitoring tools for multi-decadal to century-long spatiotemporal environmental variability. However, their effectiveness in large-scale and long-term monitoring efforts requires the development of fast phenotyping platforms that provide high-resolution scanning of large samples (e.g. leaves or wood increment cores) with many replicates to characterize intra- and inter-population variability. Advancing applications of X-ray techniques based on polycapillary optics (PolyCO), like X-ray-based computer-assisted tomography ( $\mu$ CT) and X-ray Fluorescence (XRF) are among the most promising tools to document tree structure, functioning and chemistry to disclose whole-organism properties and environmental changes.

## 1 Introduction

Plant science has been quickly evolving in the last decades with advancements in microscopic, spectroscopic and computing tools dedicated to the quantitative analysis of biological samples <sup>1)</sup>. The increasing performance of microscopes in terms of magnification, light management and motorization, coupled with the growing potential in computing and rendering capabilities, has been revolutionizing the way we look at plants. Technological advances are increasingly allowing our ability to detail plant phenotyping, i.e. quantifying plant morpho-anatomical aspects in the search for functional traits related to environmental variations.

Among the greatest frontiers challenging plant diagnostics, we can cite the following:

- In vivo 3d imaging of plant functioning, especially in woody plants where large size and the presence of secondary tissues complicate the analysis of samples.
- Identification of anatomical traits connected to plant functioning (functional anatomy), used in macroecological studies as clues for plant acclimation potential to changing environmental conditions (e.g. climate change).
- Metallomics, i.e. quantifying the inorganic constituents of organisms (essential mineral nutrients and trace elements), considered the ‘fourth pillar’ of functional genomics (together with the transcriptome, proteome and metabolome <sup>2)</sup>).

## 2 Trees as Environmental Archives

The study of trees as a whole organism still represents a big challenge. Trees are sessile organisms with indefinite growth, rooted in the same spot for centuries - or even millennia - and are unique living archives for the reconstruction of ecological history <sup>3)</sup>. Their long living tissues, like secondary xylem (i.e. wood), contain sequences of cell layers deposited through the growing season whose features are shaped according to the plant’s metabolism interaction with environmental variability. Thus, long-living plants represent biological archives that allow for long-term *a posteriori* ecological monitoring.

The use of trees as biological archives has multiple applications. In dendrochronology, the first aim is to date each xylem ring at the annual resolution. The method called cross-dating is based on comparing growth patterns among tree-ring series to assess their synchronization through a number of techniques <sup>4)</sup>. Cross-dating tree-ring series allows for the exact temporal determination (i.e. one year) of any kind of event that affected a woody plant's life.

Dendroecology is the use of cross-dated tree-ring data to reconstruct ecological events that occurred to study trees. The most widespread application is dendroclimatology, i.e. reconstructing past climate variability to cover non-instrumental periods. More in general, dendroecological applications regard the reconstruction of any kind of ecological phenomenon able to alter tree rings in terms of average development or anatomical features <sup>5)</sup>.

In dendroclimatology, extracting the climate signal from tree-ring width series allows quantifying the main climatic factors limiting inter-annual growth variability in species growing in the same or different environments. Climate control over growth can even be explored at the intra-annual time scale by matching within-ring anatomical features or intra-annual density fluctuations in wood <sup>6)</sup> to seasonal climate or selected extreme events. Increasing the time resolution of dendroclimatic studies has pushed forward our ability to reconstruct plant-climate relationships at the seasonal to the weekly timescale <sup>7)</sup>. Such a possibility has deeply relied on advances in microscopic and imaging techniques, which made easier the acquisition, manipulation and statistical elaboration of many high-resolution microscopic images to be used for tree phenotyping and quantitative functional anatomy <sup>8)</sup>.

Within the context of dendroecological techniques, a rising field is represented by dendrochemistry, i.e. the determination of the chemical composition of cross-dated tree rings <sup>9)</sup>. Detecting the presence of chemical elements in tree rings has powerful implications for both biological and ecological studies at intra- and inter-annual time scales. Information on the spatial/temporal distribution within woody tissues of chemical elements which represent basic cellular components or nutrients involved in basic physiological cellular processes (e.g. K, Cl, Mg, Mn) can provide key insights into how trees allocate nutrients to their tissues according to species, age, or environmental changes. The capability of trees to store in their annual rings inorganic (e.g. lead,

cadmium <sup>10)</sup>) and organic pollutants <sup>11)</sup> makes dendrochemical applications effective a posteriori monitoring tools to quantitatively reconstruct the time dynamics of pollution over a territory.

### 3 Physics Methods for Plant Biology

Several applications of physics have become increasingly familiar in biology in the last decades, largely thanks to research in medicine. Among the most popular techniques, we can count isotope analysis, either focused on dating biological samples via the use of radiocarbon half-life <sup>12)</sup> or on the use of the stable isotopes of carbon, hydrogen or nitrogen to infer plant functioning <sup>13)</sup> or tracing plant provenances (e.g. in olive oil <sup>14)</sup>).

Techniques like Magnetic Resonance Imaging (MRI) and Computer Tomography (CT) have become greatly popular in medical applications. MRI techniques in human organs exploit hydrogen response to modified magnetic fields to describe water diffusion through organs or tissues and infer their microstructural features or physiological state <sup>15)</sup>. CT is a scanning method that instead relies on X-rays to produce non-destructive, high-resolution microscopic reconstructions of plant structures <sup>16)</sup> or track in vivo plant functioning e.g. the formation of embolism in wood vessels during drought <sup>17)</sup>.

In plant sample spectroscopic, X-ray Fluorescence (XRF) got great popularity in applications to either leaves or wood <sup>18, 19, 20)</sup>. XRF has successfully been applied to leaves to determine the deposition of specific chemical elements. Large gaps remain in understanding the biological pathways through which pollution-related chemical elements are allocated into woody tissues after being deposited onto plant organs (leaves, bark). Furthermore, a detailed mapping of the presence of nutrients essential to plant metabolism (e.g. Ca, Mn, K) is needed to understand how chemicals are allocated to different plant's organs, and how such allocation changes with species, size or age.

At present, ultimate X-ray characterizations can be performed at Synchrotron Radiation (SR) facilities because they provide optimized radiation parameters for investigations <sup>21)</sup>. Namely, to perform advanced analyses it is necessary to deliver a high radiation flux to the sample with repeatable and controlled characteristics such as spot size, beam profile, coherence, polarization, etc. However, access to SR facilities is generally limited and many dedicated experimental stations are oversubscribed. Moreover, considering conventional X-

ray sources, the lack of optimized optics as well as hard X-ray detectors is the bottleneck for their wider use<sup>22</sup>). Nevertheless, recent achievements in the design of X-ray optical devices make it possible to obtain spatial resolution down to the micro-scale, even working with conventional X-ray tubes. Nowadays we can refer to technological advances associated with the availability of powerful compact X-ray sources and optics as well.

Among the most attractive and powerful X-ray optics well matching tabletop X-ray sources, we can emphasize polycapillary optics, e.g., multi-capillary-based lenses, semi-lenses, pillars, etc., the use of which has been continuously expanding since its invention<sup>23, 24, 25</sup>). These optics are characterized by strong focusing capability for X-ray beams with large divergences. Moreover, polycapillary optics can act as very efficient optical units both to collimate an X-ray beam and to transform a divergent X-ray beam into a quasi-parallel one<sup>26, 27</sup>).

#### **4 X-ray Applications to Tree Organs and Tissues to Enhance Environmental Analyses**

To effectively implement trees as monitoring tools for spatiotemporal environmental variability requires the development of fast phenotyping platforms with the high-resolution scanning of large samples (e.g. plant tissues or organ like leaves, wood cores) and analyze many replicates to characterize intra- and inter-population variability. In this context, PolyCO techniques can provide several insights into tree structure and properties.

The main research activities performed at XlabF were focused on X-ray analysis by means of desktop techniques, mostly based on polycapillary optical elements (PolyCO). In particular, our laboratory equipment is dedicated to several applications ranging from the analysis of micro-macro X-ray Fluorescence (XRF; traditional, confocal, total external reflection) applied to cultural heritage, geological and natural archives, to X-ray diffraction applied to imaging techniques (tomography).

X-ray based computer assisted tomography (CT) is based on a computer controlling an X-ray device that generates a series of detailed sections of an organism from different angles to create 3-dimensional (3D) views of tissues and organs. We implemented CTS (Computed Tomography Station), i.e. a measuring station for high-precision tomography equipped with a microfocusing

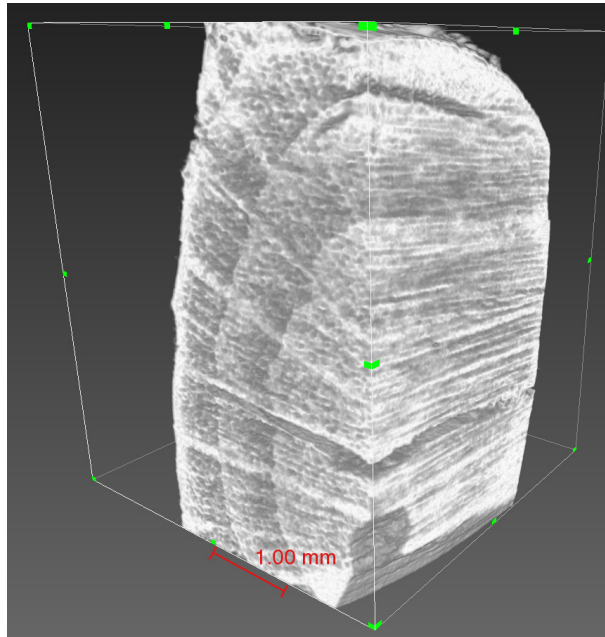


Figure 1: *Three-dimensional anatomical structure of tree wood. Inner structure of the secondary xylem of a wood sample from Aleppo pine (*Pinus halepensis* Miller) detected by X-ray micro Computer Tomography ( $\mu$ CT). The tomography shows tree rings of different widths, the presence of earlywood and latewood, the distribution of vessels and radial parenchyma.*

source ( $5\ \mu\text{m}$  on the anode), high-precision mechanics and high-resolution CCD detector ( $10.4\ \mu\text{m}$  per pixel). Through the phase retrieval technique, CTS resolution is estimated at 600-700 nm per voxel. We explored how CTS could describe the morpho-anatomical features of tree tissues/organs, with the ability to enter the inner part of the sample without the need to section it (Fig. 1). CTS was able to catch anatomical traits connected to plant phenotype changes with environmental constraints, e.g. functional traits like vessel size used for in-vivo tracking of embolism diffusion in plant conductive systems <sup>16</sup>).

A dedicated compact experimental unit, the RXR station, has been developed for advanced X-ray micro-fluorescence studies on 2- or 3- dimension stages (2D/3D  $\mu$ XRF) <sup>28</sup>). The system is equipped with a full lens PolyCO for

the primary beam, with parameters corresponding to the input focal distance (IFD) of 58.5 mm, the output focal distance (OFD) of 42 mm (the nominal values of OFD and beam size has been verified by taking some CCD images at various distances from the optics), the length of 12 cm, the input diameter of 4 mm, and a  $90\ \mu\text{m}$  focal spot size. The RXR action core is based on confocal geometry<sup>28)</sup>, the advanced method to investigate the elemental depth profile of a sample. By mounting a second semi lens for the secondary beam, the probe size is about  $80\ \mu\text{m}$  collecting a fluorescence signal in the energy range from 6 to 30 keV (the low energy can be optionally decreased to approximately 1 keV, but not in confocal mode). This configuration allows RXR to perform elemental depth profiling for different types of samples<sup>10)</sup>. Moreover, the confocal approach simplifies the measurement procedure and allows discriminating depth-dependent signals from high to low Z elements avoiding negative superposition of images.

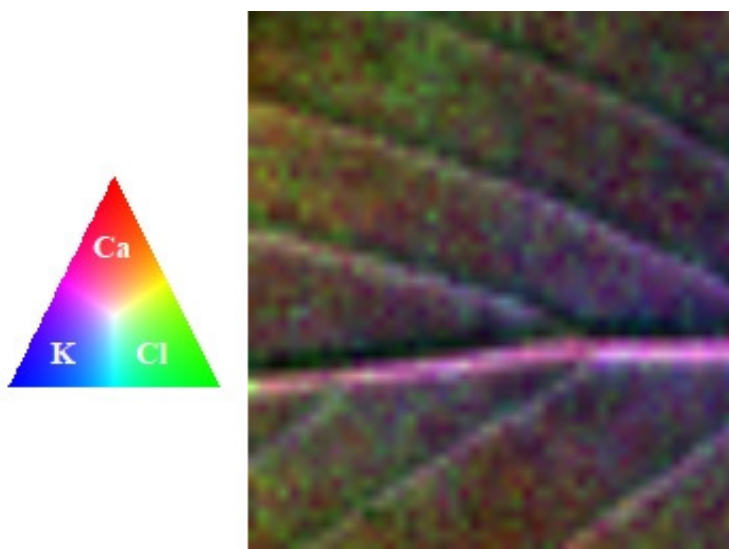


Figure 2: *Leaf surface. Selected elements detected by X-ray Fluorescence (XRF) on the bottom of a leaf blade by scanning in  $100 \times 100\ \mu\text{m}$  steps with 10 s/step acquisition time using microfocus sources coupled to polycapillary optics (PolyCO).*

$\mu$ XRF allowed the fast scanning of plant organs for mapping the presence of selected chemical elements (Fig. 2). An interesting perspective is offered in dendrochemical applications by coupling high-resolution XRF to annually resolved cross-dated tree rings to reconstruct the year-to-year pollution history of a site <sup>10</sup>).

In Fig. 3, a tree core from the main stem of European beech (*Fagus sylvatica* L.) has been analyzed for the presence of essential nutrients (Ca, K) and heavy metals (Fe, Pb). The 100  $\mu$ m scan showed in this case the increase in elements important to metabolism (K) in the physiologically active part of the stem (sapwood, toward the bark) and an increase of accumulation in heavy metal (especially lead) in the no-active part of the stem (heartwood).

The possibility of exploring how element accumulation changes through tree rings of the same plant can give information on how tree metabolism changes with increasing age/size or how pollution changes over time. According to the age of the trees sampled, dendrochemical studies can inform on how dynamics change across different time scales (seasonal to multidecadal time resolution).

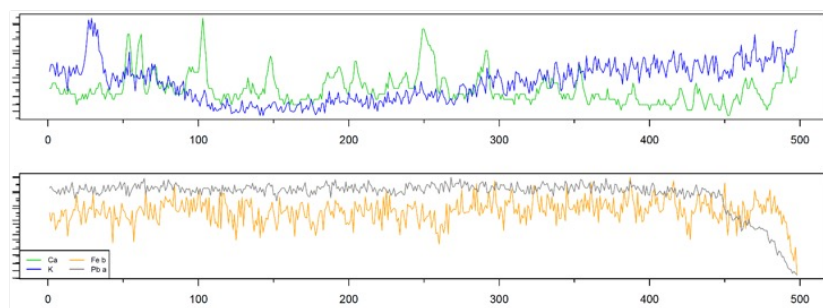


Figure 3: Tree wood increment core. Selected elements (relative units) detected by X-ray Fluorescence (XRF) from bark (right) to pith (left) in European beech (*Fagus sylvatica* L.). Each series is the average of 5 scanning lines preceding by 100x100  $\mu$ m steps with 10 s/step acquisition time using microfocus sources coupled to polycapillary optics (PolyCO). Tree core taken in radial direction with an increment borer at 1.3 m from the ground.

## 5 Conclusions

Merging dendroecology and X-ray techniques is a highly promising transdisciplinary approach to advance our knowledge of both tree biology and large-scale ecology. The possibility of analyzing relatively quickly and with low-energy requirements many large samples from different plant tissues (leaf epidermis, bark, wood) and organs (shoots, main stem) is beneficial for both biological and environmental research. It allows the establishment of large monitoring networks based on many replicated observation points relying on decadal or even century-long information (tree-rings), needed to provide the wide perspective necessary to model ecological phenomena over landscapes and help support policies to sustain environmental quality.

In macroecological applications, dendrochemistry can effectively contribute to the detection of environmental pollution along large-scale environmental gradients. Coupling the temporal perspective of tree rings with the continuous spatial coverage of satellite missions holds huge potential for modelling biosphere processes<sup>30</sup>). Multidecadal pollution time series reconstructed by tree-rings and XRF can be coupled to national- or regional-level observational networks of pollution (last 10-20 years) and new satellite missions monitoring air pollution weekly and continuously over the EU territory<sup>31</sup>) to develop new models of regional deposition dynamics. Urban or extra-urban pollution, often associated with the dispersion of particulate, is considered the leading environmental health risk factor globally, often coupled with the presence of heavy metals<sup>32</sup>). Reconstructing pollution dynamics in pre-instrumental times using tree rings and modelling their deposition along ecological gradients by integrating satellite and ground-truth data, represent a much-needed tool to determine environmental quality and plan the development of policies at the landscape level.

## 6 Acknowledgements

This study was carried out within the Agritech National Research Center (Spoke #7 - Task 1.2) and received funding from the European Union Next-GenerationEU (Piano Nazionale Di Ripresa E Resilienza (PNRR) - Missione 4 Componente 2, Investimento 1.4 - D.D. 1032 17/06/2022, CN00000022). This manuscript reflects only the authors' views and opinions, neither the European

Union nor the European Commission can be considered responsible for them.

## References

1. E.B. Blancaflor and S. Gilroy, Plant cell biology in the new millennium: new tools and new insights, *American Journal of Botany* 87(11), 1547-1560 (2000).
2. S. Mounicou, J. Szpunar, and R. Lobinski, Metallomics: the concept and methodology, *Chemical Society Reviews* 38(4), 1119-1138 (2009).
3. H. Fritts, *Tree rings and climate*, ed. Elsevier (2012).
4. M. A. Stokes, *An introduction to tree-ring dating*, University of Arizona Press (1996).
5. H.C. Fritts and T.W. Swetnam, Dendroecology: a tool for evaluating variations in past and present forest environments, *Advances in ecological research* 19, 111-188 (1989).
6. A. Di Filippo, M. Baliva, M. Brunetti and L. Di Fiore, Long-term tree-ring response to drought and frost in two *Pinus halepensis* populations growing under contrasting environmental conditions in Peninsular Italy, *Forests* 12(3), 305 (2021).
7. A. Di Filippo et al., Bioclimatology of beech (*Fagus sylvatica* L.) in the Eastern Alps: spatial and altitudinal climatic signals identified through a tree-ring network, *Journal of Biogeography* 34(11), 1873-1892 (2007).
8. F. Gennaretti, I. García-González, M. Carrer, S. Rossi and G. von Arx, Quantitative wood anatomy to explore tree responses to global change (2022).
9. G. Binda, A. Di Iorio and D. Monticelli, The what, how, why, and when of dendrochemistry: (paleo) environmental information from the chemical analysis of tree rings, *Science of the Total Environment* 758, 143672 (2021).
10. G. Cappuccio, G. Cibin, S.B. Dabagov, A. Di Filippo, G. Piovesan, D. Hampai, V. Maggi and A. Marcelli, Challenging X-ray fluorescence applications for environmental studies at XLab Frascati, *Condensed Matter* 3, 33 (2018).

11. R. Bernini et al., Dendrochemical investigation on hexachlorocyclohexane isomers (HCHs) in poplars by an integrated study of micro-Fourier transform infrared spectroscopy and gas chromatography, *Trees* 30, 1455-1463 (2016).
12. G. Quarta et al., Identifying the 993-994 CE Miyake event in the oldest dated living tree in Europe, *Radiocarbon* 61(5), 1317-1325 (2019).
13. N.J. Loader, D. McCarroll, M. Gagen, I. Robertson and R. Jalkanen, Extracting climatic information from stable isotopes in tree rings, *Terrestrial Ecology* 1, 25-48 (2007).
14. F. Camin et al., Isotopic and elemental data for tracing the origin of European olive oils, *Journal of Agricultural and Food Chemistry* 58(1), 570-577 (2010).
15. S. De Santis, A. Gabrielli, M. Bozzali, B. Maraviglia, E. Macaluso and S. Capuani, Anisotropic anomalous diffusion assessed in the human brain by scalar invariant indices, *Magnetic resonance in medicine* 65(4), 1043-1052 (2011).
16. A.J. McElrone, B. Choat, D.Y. Parkinson, A.A. MacDowell and C.R. Brodersen, Using high resolution computed tomography to visualize the three dimensional structure and function of plant vasculature, *JoVE* 74, e50162 (2013).
17. M. Nolf, R. Lopez, J.M. Peters, R.J. Flavel, L.S. Kolodan, I.M. Young and B. Choat, Visualization of xylem embolism by X-ray microtomography: a direct test against hydraulic measurements, *New Phytologist* 214(2), 890-898 (2017).
18. M. Nečemer et al., Application of X-ray fluorescence analytical techniques in phytoremediation and plant biology studies, *Spectrochimica acta part B: atomic spectroscopy* 63(11), 1240-1247 (2008).
19. F. Bilo et al., Elemental analysis of tree leaves by total reflection X-ray fluorescence: New approaches for air quality monitoring, *Chemosphere* 178, 504-512 (2017).

20. G.S. Montanha, E.S. Rodrigues, J.P.R. Marques, E. De Almeida, A.R. Dos Reis and H.W. Pereira de Carvalho, X-ray fluorescence spectroscopy (XRF) applied to plant science: challenges towards in vivo analysis of plants, *Metallomics* 12(2), 183-192 (2020).
21. K. Tsuji, J. Injuk and R. Van Grieken, *X-ray Spectrometry: Recent Technological Advances*, Wiley (2004).
22. D. Attwood, *Soft X-rays and Extreme Ultraviolet Radiation: Principles and Applications*, Cambridge University Press (2007).
23. K. Tsuji, K. Nakano and X. Ding, Development of confocal micro X-ray fluorescence instrument using two X-ray beams, *Spectrochim. Acta B* 62, 549 (2007).
24. G. Buzanich, P. Wobrauschek, C. Strel, A. Markowicz, D. Wegrzynek, E. Chinea-Cano et al., PART II (Portable ART analyzer)-development of a XRF spectrometer adapted for the study of artworks in the Kunsthistorisches Museum, Vienna, *X-ray Spectrom.* 39, 98 (2010).
25. S. Smolek, B. Pemmer, M. Fölser, C. Strel and P. Wobrauschek, Confocal micro-X-ray fluorescence spectrometer for light element analysis, *Rev. Sci. Instrum.* 83, 083703 (2012).
26. M. Kumakhov, Multiple reflection from surface X-ray optics, *Phys. Rep.* 191, 289 (1990).
27. S.B. Dabagov, Channeling of neutral particles in micro- and nanocapillaries, *Phys. Usp.* 46, 1053 (2003).
28. D. Hampai, A. Liedl, G. Cappuccio, E. Capitolo, M. Iannarelli, M. Massucci, S. Tucci, R. Sardella, A. Sciancalepore, C. Polese, S.B. Dabagov, 2D-3D  $\mu$ XRF elemental mapping of archeological samples, *Nucl. Instr. Meth. B* 402, 274-277 (2017).
29. D. Hampai, Yu.M. Cherepennikov, A. Liedl, G. Cappuccio, E. Capitolo, M. Iannarelli, C. Azzutti, Yu.P. Gladkikh, A. Marcelli and S.B. Dabagov, Polycapillary based  $\mu$ XRF station for 3D colour tomography, *JINST* 13, C04024 (2018).

30. L. Di Fiore et al., Modelling *Fagus sylvatica* stem growth along a wide thermal gradient in Italy by incorporating dendroclimatic classification and land surface phenology metrics, *International Journal of Biometeorology* 66(12), 2433-2448 (2022).
31. J.P. Veefkind et al., TROPOMI on the ESA Sentinel-5 Precursor: A GMES mission for global observations of the atmospheric composition for climate, air quality and ozone layer applications, *Remote Sensing of Environment* 120, 70-83 (2012).
32. L.T. Popoola, S.A. Adebajo and B.K. Adeoye, Assessment of atmospheric particulate matter and heavy metals: a critical review, *International Journal of Environmental Science and Technology* 15, 935-948 (2018).

**Volumetric reconstruction of color center distributions in X-ray irradiated LiF crystals obtained by confocal spectro-microscopy techniques**

F. Bonfigli

*ENEA C.R. Frascati,*

*Fusion and Technologies for Nuclear Safety and Security Dep.,*

*Photonics Micro- and Nano-structures Laboratory,*

*FSN-TECFIS-MNF, Frascati (Rome), Italy*

S. Botti

*ENEA C.R. Frascati,*

*Fusion and Technologies for Nuclear Safety and Security Dep.,*

*Photonics Micro- and Nano-structures Laboratory,*

*FSN-TECFIS-MNF, Frascati (Rome), Italy*

R.M. Montereali

*ENEA C.R. Frascati,*

*Fusion and Technologies for Nuclear Safety and Security Dep.,*

*Photonics Micro- and Nano-structures Laboratory,*

*FSN-TECFIS-MNF, Frascati (Rome), Italy*

E. Nichelatti

*ENEA C.R. Casaccia,*

*Fusion and Technologies for Safety and Security Department,*

*Photonics Micro- and Nano-structures Laboratory,*

*FSN-TECFIS-MNF, Rome, Italy*

V. Nigro

*ENEA C.R. Frascati,*

*Fusion and Technologies for Nuclear Safety and Security Dep.,*

*Photonics Micro- and Nano-structures Laboratory,*

*FSN-TECFIS-MNF, Frascati (Rome), Italy*

M. Piccinini

*ENEA C.R. Frascati,*

*Fusion and Technologies for Nuclear Safety and Security Dep.,*

*Photonics Micro- and Nano-structures Laboratory,*

*FSN-TECFIS-MNF, Frascati (Rome), Italy*

M.A. Vincenti

*ENEA C.R. Frascati,*

*Fusion and Technologies for Nuclear Safety and Security Dep.,*

*Photonics Micro- and Nano-structures Laboratory,*

*FSN-TECFIS-MNF, Frascati (Rome), Italy*

A Cecilia

*Institute for Photon Science and Synchrotron Radiation,*

*Karlsruhe Institute of Technology (KIT), Karlsruhe, Germany*

## Abstract

We report 3D reconstructions of X-ray-induced color center volumetric distributions in LiF crystals performed by confocal spectro-microscopy techniques: fluorescence microscopy and Raman micro-spectroscopy. The investigated LiF crystals were irradiated with photons of 8 and 16 keV provided by a double multilayer monochromator available at the KIT synchrotron light source (Karlsruhe, Germany). The capability of a LiF crystal to register volumetric X-ray mapping combined with the optical sectioning operations of the confocal techniques allowed to obtain 3D reconstructions of the X-ray colored volumes, providing promising results for 3D X-ray detection advanced tools.

## 1 Introduction

Solid-state radiation detectors based on lithium fluoride (LiF) represent a versatile tool for X-ray imaging [1] and for characterization of X-ray beams and optics. Passive LiF detectors rely on the visible photoluminescence (PL) emitted by stable radiation-induced color centers (CCs) that are locally produced by X-rays. Among the peculiarities of LiF-based detectors, noteworthy ones are their very high intrinsic spatial resolution across a large field of view, wide dynamic range and versatility. These detectors have been used as X-ray imaging plates with several X-ray sources, such as compact sources emitting from soft to hard X-rays [2–4], large-scale facilities [5] and for X-FEL beam monitoring [6, 7]. Volumetric detection for X-ray 3D imaging application is a topical task nowadays. The penetration of X-rays in LiF crystals produces CC volumetric distributions inside them. The combination of capability of a LiF crystal to register a volumetric X-ray mapping at high spatial resolution with the tridimensional (3D) direct reading of confocal microscope techniques allowed performing 3D reconstructions of the stored colored volumes [8–10]. LiF crystals were used to characterize the operation of polycapillary optics, such as X-ray lenses (full- and semi-lenses), by registering the transmitted X-ray beam in focusing and parallel modes [8]. A confocal laser microscope, used as reading instrument in fluorescence mode, allowed getting 2D high spatial resolution images of transmitted X-rays through the entire polycapillary semi-lens and through each single channel and a 3D tomography of the colored volume produced by quasi-parallel and focused X-ray beams by a half-lens and a full-lens, respectively [8]. This characterization has demonstrated that, with

a single X-ray beam irradiation of LiF crystals, 3D information can be obtained by using a confocal optical microscope reading system. In this paper, we report 3D reconstructions of X-ray-induced CC volumetric distributions in LiF crystals performed by two confocal laser spectro-microscopy techniques: fluorescence microscopy and Raman micro-spectroscopy. The investigated LiF crystals were irradiated at the X-ray energies of 8 keV and 16 keV provided by a double multilayer monochromator (DMM) available at the KIT synchrotron light source (Karlsruhe, Germany). The selected DMM stripe is a Pd/B<sub>4</sub>C multilayer (250 periods, layer thickness of 2.5nm) optimized to work in the energy range between 8 keV and 20 keV with an energy bandwidth of 2%. The capability of a LiF crystal to register volumetric X-ray mapping combined with the optical sectioning operations of the confocal techniques, allowed to obtain 3D reconstructions of the X-ray colored volumes.

## 2 Experimental

Two commercial LiF crystals (MacroOptica Ltd) in the form of squared plates ( $10 \times 10 \text{ mm}^2$ , 1 mm thickness), polished on both faces, were irradiated at the synchrotron light source of KIT with 8 keV and 16 keV DMM X-ray beams. The crystals were placed on axis of the synchrotron beam at normal angle of incidence and were irradiated on a uniform area of  $(4 \times 4) \text{ mm}^2$  for 112 s in the case of 8 keV X-ray beam (with an estimated dose rate of about 6 Gy/s) and for 114 s in the case of 16 keV X-ray beam (with an estimated dose rate of about 18.5 Gy/s). Among the radiation-induced electronic defects, known as CCs, we focus our attention on  $F_2$  and  $F_3^+$  aggregated defects, which consist of two electrons bound to two and three close anion vacancies, respectively. These defects have almost overlapped broad absorption bands (the M band) peaked at about 450 nm [11] and they exhibit two distinct Stokes-shifted broad emission bands in the green ( $F_3^+$ ) and red ( $F_2$ ) spectral ranges [11]. The optical absorption measurements of the irradiated LiF crystals were performed by using a Perkin-Elmer Lambda 1050 spectrophotometer at normal incidence. The spectral range was set to 190-1000 nm with 1 nm resolution. The irradiated LiF crystals store volumetric information through the local generation of stable CCs produced by X-rays along the crystal depth. After irradiation, the LiF crystals were observed by a confocal laser scanning microscope (CLSM) operating in fluorescence mode and by a confocal laser scanning Raman micro-spectrometer.

In the case of the CLSM reading system (Nikon 80i-C1), the LiF crystals were illuminated by a 445 nm continuous laser (with nominal output power of 1.5 mW) pumping in the M band. The red  $F_2$  and the green  $F_3^+$  PL signals were detected by two photomultipliers, in the red and in the green spectral ranges by using proper optical filters. By removing one of the filters in front of a photomultiplier is possible to detect the spectrally-integrated PL signal overlapped with the reflected signal of pumping laser. By scanning along the Z optical axis, the CLSM can operate an optical sectioning of the observed sample by using a pinhole in front of the detector placed in a conjugate plane with respect to the focus one and detecting only signals from the in-focus plane by eliminating signals from out-of-focus ones. The optical sectioning allows obtaining a 3D reconstruction of the sample and it has been exploited to reconstruct the 3D depth distribution of CCs in the colored volumes. 2D and 3D Raman maps were measured by a Raman spectrometer combined with a confocal microscope (Horiba XploRA Plus) by exciting with a 532 nm wavelength laser. A Raman spectrometer combined with a confocal optical microscope acquires signals of a complete Raman spectrum in each point of 2D and 3D maps by scanning the sample in the XYZ directions.

### 3 Results

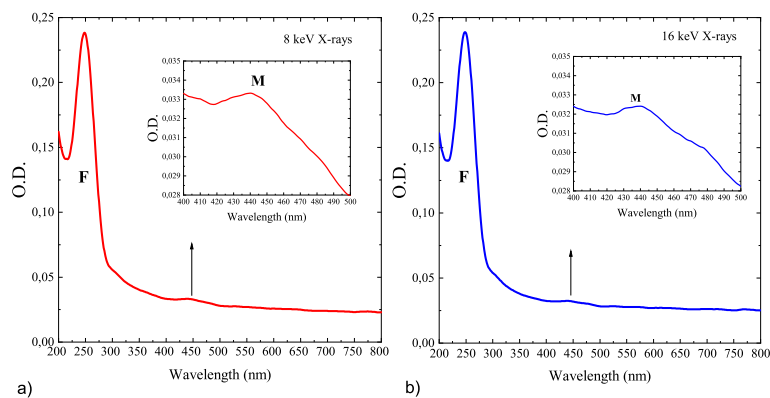


Figure 1: *Absorption spectra at room temperature of colored areas of the LiF crystals irradiated with the DMM X-ray beams at 8 keV (a) and 16 keV (b).*

Absorption spectra reported in Figure 1 were measured for the LiF crystals irradiated with the DMM X-ray beams at 8 keV (a) and 16 keV (b). The F band is related to the primary F defects, otherwise the broad M band is due to the overlapping absorption band of the  $F_2$  and  $F_3^+$  aggregated defects.

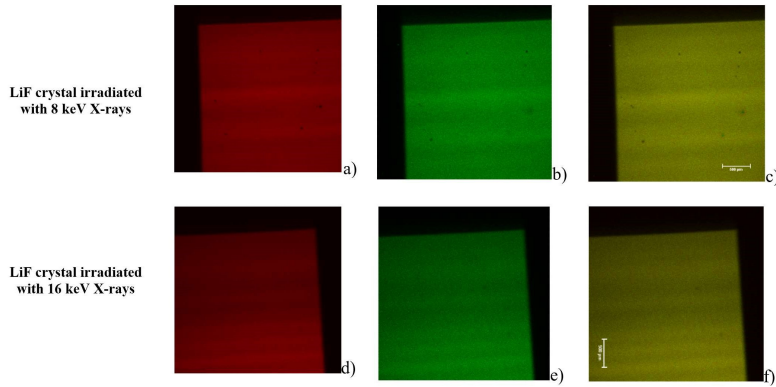


Figure 2: 2D CLSM fluorescence images of the X-ray (8 keV (a,b,c) and 16 keV (d,e,f)) irradiated LiF crystals corresponding to the detections of the red PL signal of  $F_2$  CCs (a, d), the green PL signal of  $F_3^+$  CCs (b, e) and their overlapping signals (c, f). Scale bar 500  $\mu\text{m}$ .

Figure 2 reports the 2D CLSM fluorescence images of corners of the uniform square areas of the X-ray (8 and 16 keV) irradiated LiF crystals corresponding to the detections, separately, of the red PL signal of  $F_2$  CCs, the green PL signal of  $F_3^+$  CCs, and their overlapping signal. The CLSM fluorescence images are characterized by a slight intensity modulation, which is related to the pattern stripe typical of DMM beams [12].

By using the optical sectioning of the CLSM system operating in fluorescence mode along the optical Z axis by controlled spatial increments, several slices along the colored volume of the irradiated LiF crystals were obtained. Figure 3 reports the 3D reconstruction ( $XY = 636 \times 636 \mu\text{m}^2$ ,  $Z = 0-1 \text{ mm}$ ) of the colored volumes, obtained by detecting the  $F_2$  PL signals of the 8 keV (a) and the 16 keV (b) X-ray irradiated LiF crystals. According to the X-ray

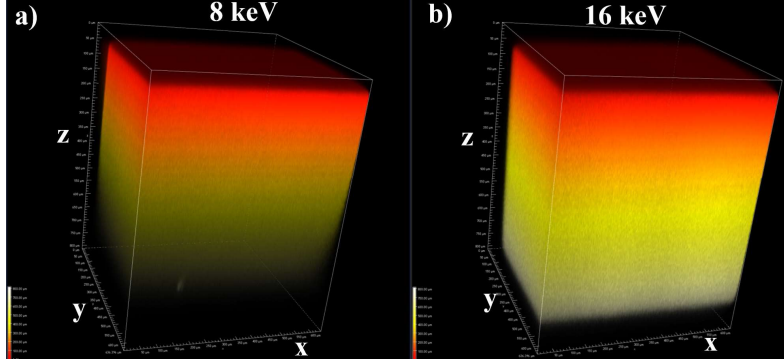


Figure 3: 3D reconstructions ( $XY = 636 \times 636 \mu\text{m}^2$ ,  $Z = 0\text{-}1 \text{ mm}$ ) of the red photoluminescent CC volumes acquired by CLSM of the 8 keV (a) and the 16 keV (b) X-ray irradiated LiF crystals on a uniform area.

transmission properties in solids [13], the penetration depth of X-rays in LiF depends on the X-ray energy and the energy deposition of an X-ray beam exponentially decreases along the penetration depth. In the X-ray induced CC volume distributions reported in Figure 3, it is evident a higher penetration depth at the highest energy and a decrease of the PL signal with depth. Assuming that the CC concentrations are proportional to the deposited energy, the confocal fluorescence microscope is an appropriate technique to investigate the X-ray colored profile along the crystal thickness (Z direction).

Figures 4 a) and b) report the PL intensity profiles (black curves) along the Z scan optical axis (thickness of the LiF crystals) of the 3D image reported in Figure 3 a) and b) for the 8 and 16 keV irradiated LiF crystals, respectively. The  $F_2$  PL profiles are shown together with the laser signals reflected by the LiF crystal surfaces overlapped with the PL signals (grey curves), as spatial reference. Figures 4 c) and d) report the PL intensity profiles (black curves) along the Z scan optical axis together with Monte Carlo simulations of absorbed dose (red dashed curves) for 8 and 16 keV energies, respectively, obtained with the free software EGSnrc [14]. By a best fitting of the experimental  $F_2$  PL profiles along the Z axis with a single exponential curve, a value of  $(236 \pm 3) \mu\text{m}$ ,

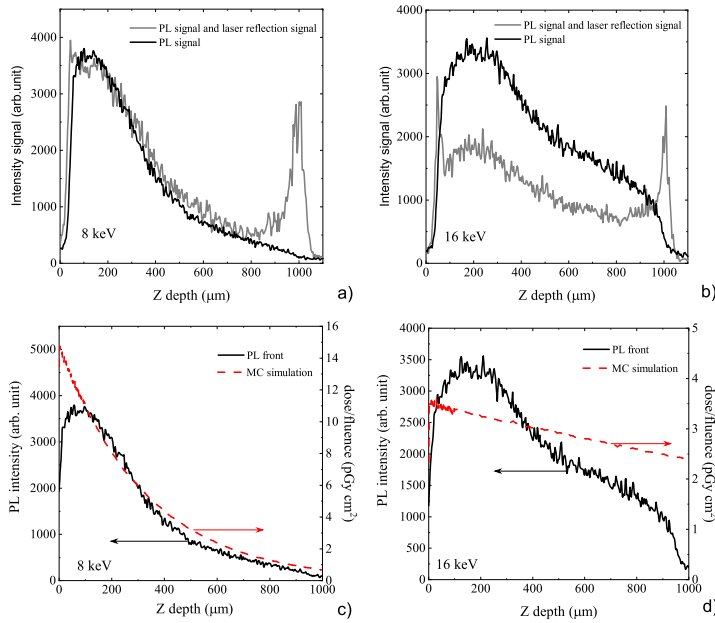


Figure 4: a) b)  $F_2$  PL intensity profiles (black curves, arbitrary units) along the Z axis (LiF crystal thickness) of the 3D images for the 8 and 16 keV X-ray irradiated LiF crystals reported in Figure 3 a) and b), respectively. The  $F_2$  PL profiles are shown together with laser signals reflected by the LiF crystal surfaces overlapped to the PL signals (grey curves). c) d) PL intensity profiles (black curves) along the Z scan optical axis together with Monte Carlo simulations of absorbed dose (red dashed curves) for 8 and 16 keV energies, respectively.

corresponding to the  $1/e$  of the maximum, was obtained [9]. The theoretical X-ray attenuation length in LiF corresponding to an X-ray energy of  $\approx 8$  keV is about  $331 \mu\text{m}$  [13]. For the 16 keV irradiated LiF crystal, the expected value is about  $2650 \mu\text{m}$  and at higher energy the experimental data deviate from simulations. Possible effect of absorption of the 445 nm pumping laser by CCs could have occurred in the optical sectioning operation; a comparison with the confocal Raman micro-spectrometer was performed, as at 532 nm the absorption is negligible (see Figure 1).

3D Raman maps ( $XY = 182 \times 172 \mu\text{m}^2$ ,  $Z = 0\text{-}1 \text{ mm}$ ) of the uniform

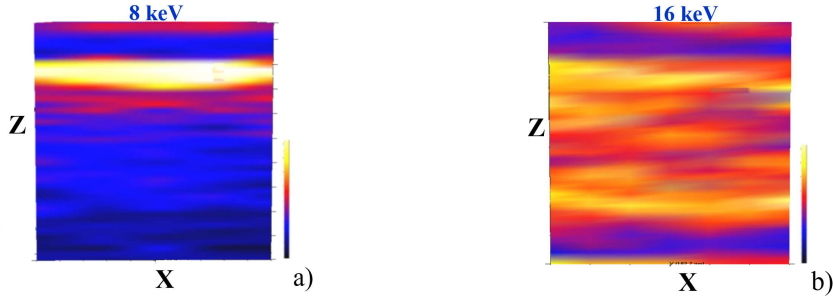


Figure 5:  $XZ$  ( $Z$ : 0-800  $\mu\text{m}$ ) slices of the 3D Raman maps for the 8 keV (a) and the 16 keV (b) X-rays irradiated LiF crystals.

colored area of the 1 mm thick LiF crystals irradiated with 8 keV and 16 keV X-rays were measured by using the optical sectioning of the confocal Raman spectrometer along the optical  $Z$  axis. Figure 5 reports the  $XZ$  slices of the 3D Raman maps for the 8 keV (a) and the 16 keV (b) X-rays irradiated LiF crystals.

Figures 6 a) and b) report the Raman signal profiles (blue curves) along the  $Z$  scan optical axis together with Monte Carlo simulations for 8 and 16 keV energies, respectively. For 8 keV irradiated LiF crystal, the experimental curve fit quite well the simulation at short  $Z$  depths; again, at the higher X-ray energy the experimental data deviate from simulations.

In the case of the 8 keV irradiated LiF crystal, from the fitting with a single exponential curve of the experimental Raman intensity profile along the  $Z$  direction, a value of  $(221 \pm 3) \mu\text{m}$ , corresponding to the  $1/e$  of the maximum, was obtained [9]. This value is close to that obtained with the red fluorescence signal in the CLSM systems. Further investigations regarding optical sectioning operations of the confocal systems based on the detection of PL and Raman signals applied to X-ray colored LiF crystals are in progress.

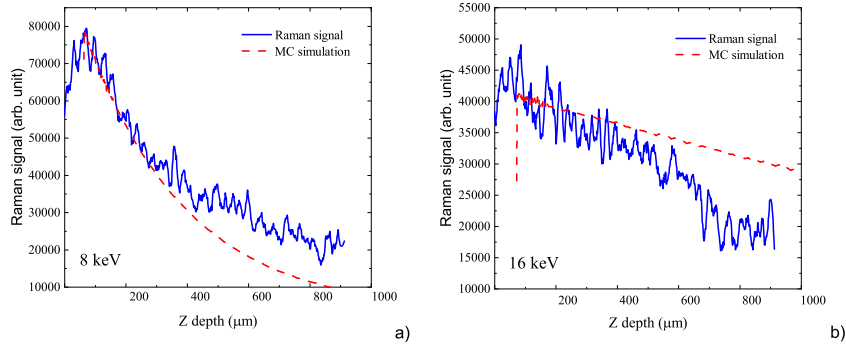


Figure 6: Raman signal profiles (blue curves, arbitrary units) along the Z axis (thickness of the LiF crystals) of the 3D images reported in Figure 5 a) and b) for the LiF crystals irradiated with 8 (a) and 16 keV (b) energies. The Raman signal profiles are shown together with Monte Carlo simulations performed for both energies (red dashed curves).

#### 4 Conclusions

Volumetric distributions of CCs in LiF crystals were measured by confocal spectro-microscopy techniques operating in fluorescence and Raman modes. The CCs were produced in LiF crystals by irradiating at normal angle of incidence with respect to the crystal surfaces with DMM X-rays (8 and 16 keV) at KIT synchrotron light source (Karlsruhe, Germany). Experimental PL and Raman signal profiles along the LiF crystal depths were analyzed and compared with Monte Carlo simulations. Further investigations regarding optical sectioning performed by confocal techniques based on fluorescence microscopy and Raman micro-spectroscopy applied to the reconstruction of volumetric CC distributions in LiF crystals are in progress in order to understand the effects of the measurement conditions and the limits of this approach. The capability of LiF crystals to register volumetric radiation-induced defects together with 3D reconstruction operated by confocal laser techniques provide promising perspectives for 3D X-ray detection advanced tools and for optical data storage applications.

## 5 Acknowledgements

Research carried out within the TecHea (Technologies for Health) project, funded by ENEA.

## References

1. R. M. Montereali, F. Bonfigli, E. Nichelatti, M. Piccinini, and M. A. Vincenti. 2.3 Luminescence of point defects in lithium fluoride thin layers for radiation imaging detectors at the nanoscale. In Alfred J. Meixner, Monika Fleischer, Dieter P. Kern, Evgeniya Sheremet, and Norman McMillan, editors, *Optical NanoSpectroscopy*, volume **3**, pages 69–96. Boston: De Gruyter, 2023.
2. D. Hampai, F. Bonfigli, S.B. Dabagov, R.M. Montereali, G. Della Ventura, F. Bellatreccia, and M. Magi. LiF Detectors-Polycapillary Lens for Advanced X-ray Imaging. *Nuclear Instruments & Methods In Physics Research A NIMA*, **720**, 113 – 115, (2013).
3. S. Almviva, F. Bonfigli, I. Franzini, A.Lai, D.Pelliccia R.M. Montereali, A.Cedola, and S. Lagomarsino. Hard x-ray contact microscopy with 250 nm spatial resolution using a LiF film detector and table-top microsource. *Applied Physics Letters*, **89**, 054102–1–3, (2006).
4. G. Baldacchini, S. Bollanti, F. Bonfigli, F. Flora, P. Di Lazzaro, A. Lai, T. Marolo, R. M. Montereali, D. Murra, A. Faenov, E. Nichelatti T. Pikuz, G. Tomassetti, A. Reale, L. Reale, A. Ritucci, T. Limongi, L. Palladino, M. Francucci, S. Martellucci, and G. Petrocelli. Soft X-ray submicron imaging detector based on point defects in LiF. *Review Scientific Instrument*, **76**, 113104–1–12, (2005).
5. F. Bonfigli, A. Cecilia, S. Heidari Bateni, E. Nichelatti, D. Pelliccia, F. Somma, P. Vagovic, M.A. Vincenti, T. Baumbach, and R.M. Montereali. In-line X-ray lensless imaging with lithium fluoride film detectors. *Radiation Measurements*, **56**, 277–280, (2013).
6. F. Bonfigli on behalf of F. Capotondi and A. Cricenti and L. Giannessi, M. Kiskinova and M. Luce and N. Mahne and M. Manfreda and R. M. Mon-

- teriali and E. Nichelatti and E. Pedersoli and L. Raimondi and M. A. Vincenti and M. Zangrando. Imaging detectors based on photoluminescence of radiation-induced defects in lithium fluoride for XFEL beam monitoring. *Il Nuovo Cimento*, **42 C**, 1–8, (2019).
7. F. Bonfigli, N. J. Hartley, Y. Inubushi, M. Koenig, T. Matsuoka, S. Makarov, R. M. Montereali, E. Nichelatti, N. Ozaki, M. Piccinini, S. Pikuz, T. Pikuz, D. Sagae, M. A. Vincenti, M. Yabashi, and T. Yabuuchi. Photoluminescence properties and characterization of LiF-based imaging detector irradiated by 10 keV XFEL beam. In Libor Juha, Saša Bajt, and Stéphane Guizard, editors, *Optics Damage and Materials Processing by EUV/X-ray Radiation VII*, volume **11035**, page 110350N. International Society for Optics and Photonics, SPIE, (2019).
  8. F. Bonfigli, D. Hampai, S. B. Dabagov, and R. M. Montereali. Characterization of X-ray polycapillary optics by LiF crystal radiation detectors through confocal fluorescence microscopy. *Optical Materials*, **58**, 398–405, (2016).
  9. F. Bonfigli, Sabina S. Botti, Angelica Cecilia, Rosa Maria Montereali, Enrico Nichelatti, Valentina Nigro, Massimo Piccinini, and Maria Aurora Vincenti. Confocal Fluorescence Microscopy and Confocal Raman Microspectroscopy of X-ray Irradiated LiF Crystals. *Condensed Matter*, **6**, (4), (2021).
  10. T. Pikuz, A. Faenov, T. Matsuoka, S. Matsuyama, N. Ozaki K. Yamauchi, B. Albertazzi, Y. Inubushi, M. Yabashi, K. Tono, Y. Sato, H. Yumoto, H. Ohashi, S. Pikuz, A. N. Grum-Grzhimailo, M. Nishikino, T. Kawachi, T. Ishikawa, and R. Kodama. 3D visualization of XFEL beam focusing properties using LiF crystal X-ray detector. *Scientific Report*, **5**, 1–10, (2015).
  11. J. Nahum and D. A. Wiegand. Optical Properties of Some *F*-Aggregate Centers in LiF. *Phys. Rev.*, **154**, 817–830, Feb (1967).
  12. A. Rack, T. Weitkamp, I. Zanette, Ch. Morawe, A. Vivo Rommeveaux, P. Tafforeau, P. Cloetens, E. Ziegler, T. Rack, A. Cecilia, P. Vagovič, E. Harmann, R. Dietsch, and H. Riesemeier. Coherence preservation

and beam flatness of a single-bounce multilayer monochromator (beamline ID19—ESRF). *Nuclear Instruments and Methods in Physics Research Section A: Accelerators, Spectrometers, Detectors and Associated Equipment*, **649**(1), 123–127, (2011). National Synchrotron Radiation Instrumentation conference in 2010.

13. X-Ray Database. [http://henke.lbl.gov/optical\\_constants/](http://henke.lbl.gov/optical_constants/).
14. I. Kawrakow and E. Mainegra-Hing and D.W.O. Rogers and F. Tessier and B.R.B. Walters. The egsnrc code system: Monte carlo simulation of electron and photon transport. Technical Report Technical Report PIRS-701, National Research Council, Canada, (2017).

**DIAGNOSTIC STUDY FOR THE COLOUR  
CHARACTERISATION AND RESTORATION OF A JAPANESE  
HANDSCROLL**

S. Ceccarelli

*Ist. di Sci. per il Patrimonio Culturale, CNR, Montelibretti, Rome, Italy.*

M. Redi

*Lab. di Conservazione e Restauro dei Beni Culturali,  
Dip. Studi Letterari, Filosofici e di Storia dell'Arte,  
Univ. di Roma Tor Vergata, Rome, Italy.*

A. Terrei

*Lab. di Conservazione e Restauro dei Beni Culturali,  
Dip. Studi Letterari, Filosofici e di Storia dell'Arte,  
Univ. di Roma Tor Vergata, Rome, Italy.*

N. Orazi

*Dip. di Ingegneria Industriale, Univ. di Roma Tor Vergata, Rome, Italy.*

V. Guglielmotti

*INFN LNF, XlabF, Frascati, Rome, Italy.  
Univ. degli Studi Guglielmo Marconi, Rome, Italy.*

D. Hampai

*INFN LNF, XlabF, Frascati, Rome, Italy.*

S.B. Dabagov

*INFN LNF, XlabF, Frascati, Rome, Italy.  
RAS P.N. Lebedev Physical Institute, 119991, Moscow, Russia.  
National Research Nuclear University MEPhI, 115409, Moscow, Russia*

F. Mercuri

*Dip. di Ingegneria Industriale, Univ. di Roma Tor Vergata, Rome, Italy.*

**Abstract**

In the analysis of a Cultural Heritage item aimed at its restoration, the materials characterisation is fundamental to achieve a better knowledge of the artwork and to address the choice of suitable tools for the recovery and the consolidation of the object layers. In this paper, we present a diagnostic study on a unique Japanese painted handscroll (emakimono) dated back to the 19<sup>th</sup> century, preserved at the Museum of the Civilisation- Prehistoric Ethnographic Museum "Luigi Pigorini" in Rome (Italy). The artwork required an urgent restoration of the entire structure and also the consolidation of the pictorial

layer. In order to define specific interventions and restoration materials, non-destructive measurements by means of Fiber Optics Reflectance Spectroscopy (FORS) and X-Rays Fluorescence Spectroscopy (XRF) were carried out on the artefact. The results allowed the identification of the colour palette, then used for tests on the chromaticity and the efficacy of the consolidants to employ in the restoration.

## 1 Introduction

Colour is an important feature of a Cultural Heritage (CH) item, representing the very first means of communication since the prehistoric periods and the expression of human creativity. In painted artefacts, colours are the main part of the artwork itself and they are an essential element of its materiality. The loss of such features leads to the decrease of the value, the meaning and also the communication power of the CH item. In the case of ancient manuscripts, coloured elements had the role of enriching the artefact and capturing the attention of the reader. Indeed, the colour appears in many types of decorations, like as small and colourful illuminations, typical of the occidental mediaeval manuscripts <sup>1)</sup>, or as tool to describe the story itself, like in the oriental handscroll here investigated. The studied artefact is classified as emakimono, that means "horizontal painting to unroll" <sup>2)</sup> and it is characterised by a particular decorative apparatus with a rich coloured palette which presented several conservation problems, such as the loss of cohesion of the pigments and their detachment from the paper support. Thus, a non-destructive diagnostic survey based on the colour identification was essential in order to design the best restoration approach to consolidate the paint layer and to create the conditions suitable for the museum exposition. For these reasons, Fiber Optics Reflectance Spectroscopy (FORS) and X-Rays Fluorescence Spectroscopy (XRF) were employed on the handscroll for the colorimetric and qualitative evaluations of pigments through the analysis of the characteristic spectra and chemical responses <sup>3, 4, 5, 6)</sup>. FORS technique was used for its capability to obtain, in a non-destructive way, quick colorimetric data for the evaluation of changes in colour or whiteness in the artwork. In addition, a prototypal XRF system was employed, allowing us to obtain punctual analyses and chemical characterisation of the colours, also where the pigments powder was inhomogeneous. The

complementarity of these methods provided the colour characterization of the investigated emakimono and the identification of the pigments, which are coherent with the historical-artistic period of the handscroll. Finally, the results were then used for the elaboration of a laboratory mock-up with the aim of studying the behaviour of different types of consolidants to be applied to the pigments and evaluating the behaviour of the adopted materials, also artificial aged, with the final goal of planning the most adequate intervention procedure.

## 2 The Japanese handscroll

The handscroll object of this study is entitled *Jizō Engi Jō* and it is the volume one of the Legend of Jizo referred to the history of the Yata temple in Kyoto. Such an artwork is a Japanese emakimono executed in ink and paint on paper, part of the Vincenzo Ragusa's Collection owned by the Civilization Museum in Rome. The scroll is a 19<sup>th</sup> century copy of a 14<sup>th</sup> century work, known as *Yata Jizō Engi*, composed by two handscrolls (*jo* and *ge*, volume one and two) that is believed to be written by the Japanese poet Fujiwara no Ietaka in the early Kamakura period and probably illustrated by the famous painter Takashina Takakane. The 14<sup>th</sup> century handscrolls are still preserved at the Yata temple in Kyoto and they are considered as Important Cultural Property. The *Jizō Engi Jō* emakimono is dated approximately back to the 1870 decade thanks to a brief text written on the last sheet of the scroll. Such text refers to the purchase of the object for export purposes during the seventh or tenth year of the Meiji era (respectively 1874 or 1877) and it is accompanied by a seal of the Japanese antique dealer Ninagawa Noritane. The artwork was indeed purchased by the Italian artist Vincenzo Ragusa (1841-1927) who lived in Tokyo between 1876 and 1882. Between 1888 and 1916, after his return to Palermo with his wife, the Japanese painter O'Tama Kiyohara (1861-1939), the Italian artist sold his collection to the Royal Luigi Pigorini Ethnographic Museum in Rome and nowadays it is preserved at the Museum of Civilizations. The handscroll belongs to the *Engi-e* genre, a label that applies to a wide range of textual and painting materials, especially referring to the histories and legends of Buddhist temples and shrines. The *Jizō Engi Jō* narrates part of the legends relating to the Yata-dera temple principal deity, the Bodhisattva Jizō, and it illustrates the journey of the High Priest Manmei to the Reign of King Enma (one of the ten kings of the Buddhist Hell), where the monk

admires the Bodhisattva's benevolence towards the souls of the damned, who can be saved from the torments of Hell thanks to Jizo's intercession.

The illustrated scenes, which adorn most of the handscroll, are painted in a Japanese style typical of the late 14<sup>th</sup> century, called Yamato-e. The absence of geometric perspective and the use of overlapping layers of colours outlined by thin brushstrokes are some of the elements that characterise this pictorial style. The first sheets of the scroll contain a text in Chinese language written in black ink (*sumi*), which represents an introduction to the narrated events and links the foundation of the temple to the will of Emperor Tenmu (631-686). Furthermore, short texts written in popular vernacular Japanese are interspersed among the paintings. The structure of the Engi *emakimono* realised on paper differs in some features with the respect to the most known Japanese handscrolls. Paintings mounted in this format are meant to be unrolled horizontally (from right to left) and viewed by one person at a time, who, while unrolling the scroll with the left hand, should roll up the section just viewed with the right one (Fig. 1). Therefore, the materials of which handscrolls are made must be flexible yet robust, qualities both owned by Japanese paper and silk. They are usually made up by various sheets of paper (more rarely silk) lined and joined together with a system of backing layers of Japanese paper, wrapped around a roller attached to the left end <sup>7, 8</sup>). Due to the "functional" destination of use of Japanese artworks and the nature of the material employed in the making of such artistic artifacts <sup>9</sup>), it is well known that Japanese scrolls often require periodic conservation treatments and substitution of the lining, thus they are rarely found in the original state: therefore, the historical significance of the treated painting is enhanced by the preservation state of its original conditions.

The Jizō Engi measures approximately 35 cm in height per 10 m in length and its structure is composed by a cover, the outermost sheet ( *hyōshi*) and at its right end is attached the *hasso*, a traditional bamboo wooden stick that allows the correct closing system of the handscroll. Four sheets (35cm x 25cm) are attached to the *hyōshi* that contain the Chinese text, followed by 32 sheets containing the painting and brief texts, these sheets constitute the *honshi* of the scroll <sup>10</sup>). The *honshi* is backed by one layer of lining made by a series of paper sheets of *kozo* paper firstly attached together by gluing themselves on the short sides, slightly overlapped, then glued to the back of the artwork itself <sup>11, 12</sup>). A wooden rod with red lacquered ends, *jiku*, is attached to the



Figure 1: *Detail of the Jizō Engi Jō handscroll.*

outermost part (left edge) of the last sheet of the handscroll, that is the rod around which the entire scroll is rolled.

## 2.1 Conservation issues

Because of the peculiar ways of conservation of handscrolls, which are typically preserved by being rolled up, the *emakimono*'s paintings usually do not suffer much from photochemical damages caused by the exposure to light. Nevertheless, they are consistently subjected to mechanical and physical stresses induced during the consultation and manipulation. The state of conservation of the coating of the paper supports, traditionally made of a mixture of animal glue (*nikawa*) and alum, known as *dosa*, contribute significantly to the conservation of the pictorial film of this kind of works of art. *Dosa* reduces the porosity of the paper surface, making it more resistant to hygroscopic variations, but it can also prevent pigments and colours from penetrating into the painting supports.

The *Jizō Engi* handscroll has never been restored before and the conservation assessment of the work revealed several damages of the paper support, such as material losses, foxing along the edges and horizontal creases probably due to the wrong handling of the object. Nevertheless, the structural qualities and the mechanical properties of the support were to be considered in discrete state of conservation. On the other hand, the dehydration and the ageing of the media's binding determined its loss of functionality hence causing losses, flaking of the pictorial surface and the incoherence of the pigments in many

areas of the handscroll, requiring an urgent consolidation procedure. Extended losses affected the areas painted in blue, while the green details of the illustrations were often affected by the flaking of the most superficial layers of paint. The areas of the paper support near the reds showed the abundant presence of particles of pigments detached from the painting surface and the same dusting and incoherence affected the orange painted details.

### 3 Analysis

In order to characterise the colour palette of the *emakimono* for the identification of the proper materials for the restoration, a combined approach was applied by performing non-destructive FORS and XRF measurements on the artwork. The results were then used for the elaboration of a test sample with the aim of evaluating the effects caused by the artificial ageing of consolidants and pigments.

#### 3.1 Fiber Optics Reflectance Spectroscopy

Reflectance spectra were recorded with a StellarNet GREEN-Wave spectrometers equipped with a D65 illuminant for measurements within the spectral range from 350nm to 1150 nm. The instrument is optically coupled by means of fibre to a cube with an internal integrating sphere able to measure an area with a diameter of 1 cm<sup>2</sup> <sup>13)</sup>. The calibration of the system was performed using a reference target with a >97% certificated reflectance to the light from 300-1700 nm. The measures were performed arranging the probe on the handscroll where the colours appeared to be more consistent. Then, the acquired spectra were compared with the available database <sup>14)</sup> to identify the pigments by their characteristics reflectance spectra.

Further investigations were conducted on the paper support for characterising its chromatism and whiteness with the aim of verifying the effectiveness of the cleaning procedure. Such evaluations were carried out by calculating the differences in colour ( $\Delta EL^*a^*b^*$ ) and in whiteness ( $\Delta WL^*a^*b^*$ ) <sup>15, 16)</sup> before and after the restoration procedures.



Figure 2: *Sampled points with FORS technique.*

### 3.2 Prototypal X-Rays Fluorescence Spectroscopy

The XRF spectra were acquired in the same points of the FORS measures by using the "Rainbow X-Ray" (*RXR*) experimental station developed at the XLab Frascati of the Istituto Nazionale di Fisica Nucleare–Laboratori Nazionali di Frascati (INFN-LNF) <sup>17, 18</sup>. The RXR layout is dedicated to advanced X-ray micro-fluorescence studies on 2-or 3-dimension stages (2D/3D  $\mu$ XRF), being equipped with polycapillary lenses in a confocal geometry <sup>17, 18</sup>. The system is based on a full lens PolyCO for the primary beam, with parameters corresponding to the input focal distance (IFD) of 58.5 mm, the output focal distance (OFD) of 42 mm, the length of 120 mm, the input diameter of 4 mm and a 90  $\mu$ m focal spot size. This configuration allows RXR to perform elemental depth profiling for different types of the samples <sup>18</sup>. Moreover, the confocal approach simplifies the measurement procedure and allows discrimi-

nating depth-dependent signals from high to low  $Z$  elements avoiding negative superposition of images. The core of RXR (Fig. 3) is based on the measurement head (a monolithic Al block) in which the various components inserted are: an X-ray tube (Mo, 50 kV - 1 mA) with a focusing PolyCO, two detectors (one combined with a PolyCO for confocal measurements), an optical microscope with CCD camera. The xyz is a micrometric stage with the precision of  $3\ \mu\text{m}$  in the plane  $xy$  and  $10\ \mu\text{m}$  in  $z$  designed to enable XRF analysis of objects large up to  $40\times 60\times 40\ \text{cm}^3$  with a weight up to 100 kg.



Figure 3: *RXR experimental setup.*

#### 4 Results

The results of the non-destructive analyses are shown in the following paragraphs, comparing FORS and XRF data for the handscroll characterisation.

#### 4.1 Colours identification

The FORS spectra show the typical profiles of the analysed colours with a higher signal in correspondence of most homogeneous sampled areas, such as in the case of red pigment. The different signal intensity between the green and yellow samples with respect to their references are probably due to pigment powder inhomogeneity, paper support and binder ageing effects. The lower reflectance signal could be due also to the support and binder contributions. Comparing the spectra with the existing databases<sup>14)</sup>, a recognition of the pigments was provided, as reported in Fig. 4. The pigments identification was confirmed by the XRF analyses (Fig. 5 where the sampled points and the related XRF spectra are reported). The details of the experimental parameters were already reported in<sup>18)</sup>. In particular, the Fundamental Parameter Method (FPM) was applied to estimate the concentration (in %) of the chemical elements (reported in Tab. 1) revealed by micro XRF with the purpose of assessing the existence of a stoichiometric ratio, among the elements, which could confirm or not the presence of a specific pigment. The values given in Tab. 1 derive from the application of a mathematical calculation used to estimate concentrations<sup>17)</sup> to which an approximation on the significant figures was applied.

These findings were coupled with the data coming from historical and literature knowledge about the scrolls and the artistic materials, confirming the coherence between materials and dating. The identified pigments of the analysed colours are summarised in Tab. 2

In order to evaluate any changes in the chromatism ( $\Delta E$ ) and the whiteness ( $\Delta W$ ) of the paper support after the restoration and the consequent effectiveness of the cleaning procedure, further FORS measures were performed before and after the cleaning in different areas of the handscroll, where no colours were present. The results are reported in Tab. 3. It is worth to note that the minimum value associated with a difference in colour perceived by the human eye is 2. In many of the treated areas, significant variations were measured in term of colorimetric parameters and brightness of the supports. In most cases, the effects of cleaning, appreciable to the naked eye, were confirmed by values of  $\Delta E$  between 3 and 12. Moreover, a general increase in the whiteness parameter ( $\Delta W$ ) was observed, confirming the effectiveness of cleaning process.

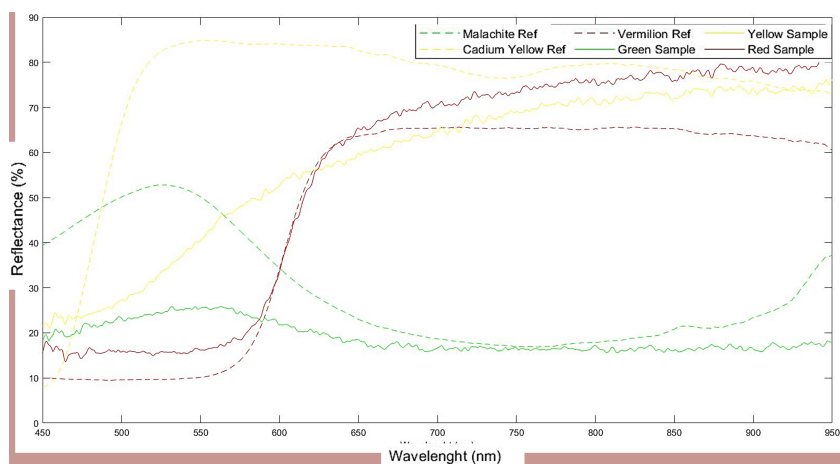


Figure 4: *FORS spectra of the sampled points on the handscroll of Fig. 2 (the continuous lines) compared with the references (dashed lines) coming from the database <sup>14</sup>.*

#### 4.2 Test Sample

The above-described results were used for the preparation of a laboratory sample on which further tests were performed for the identification of the best consolidant to apply during the restoration, by evaluating any chromaticity variations due to an artificial ageing process induced on the sample. Such an artificial process was performed for 17 days within a climate chamber at a temperature of 80° C and humidity values between 65-70 %. For the evaluation of the effects caused by the ageing of the consolidants on the sample, the variations of chromatism ( $\Delta E$ ) and, in this case, lightness ( $\Delta L$ ) were considered. The assessment of such parameters has the purpose to verify the consolidants inability to alter the refractive index and the chromatic characteristic of the media (i.e., that it must not shine, dull or yellow the surface). The laboratory mock-up was prepared using powdered mineral pigments mixed with Nikawa glue, applied on a support made of two layers of Japanese paper sized to simulate conditions and materials as similar as the original ones. The paint samples were then treated with the following consolidants <sup>19</sup>):

- Klucel<sup>®</sup> G (hydroxypropylcellulose) prepared in alcohol solution with a



Figure 5: *microXRF spectra of the sampled points obtained by RXR.*

concentration of 1%;

- Funori at 0.5% concentration in water solution;
- Nikawa glue at 1% concentration.

As can be noticed by the data shown in Tab. 4 for the green colour, the best results were obtained with Funori and Nikawa glue. In both cases, the smallest variations of the parameters were measured, corresponding to changes not perceptible to the eye.

Thus, considering the smallest values of  $\Delta E$  and  $\Delta L$ , the best consolidant considered suitable for the restoration of the handscroll was the Nikawa glue. The latter is the same adhesive traditionally used as binding and whose properties of flexibility, chemical stability and compatibility with Oriental artefacts and paintings are beginning to be acknowledged even in the Western conservation culture <sup>7)</sup>.

## 5 Restoration

Preliminary analytical tests and analysis conducted on the artefact have allowed to gain information about the materials employed in the Jizo Engi scroll and the traditional methods of handscroll manufacturing, being of crucial importance

Table 1: Concentration and error values (in %) of the chemical elements acquired in the points in Fig. 5.

	<b>Blue</b>		<b>Light Blue</b>		<b>Brown</b>		<b>Green</b>		<b>Light Green</b>		<b>Root</b>	
<b>Element</b>	Conc. [%]	Err. [%]	Conc. [%]	Err. [%]	Conc. [%]	Err. [%]	Conc. [%]	Err. [%]	Conc. [%]	Err. [%]	Conc. [%]	Err. [%]
<b>Al</b>	0.00	0.00	3.14	0.15	2.09	0.25	12.85	0.67	8.71	0.68	3.10	0.22
<b>Si</b>	3.73	0.59	2.14	0.36	5.87	0.56	0.00	0.00	0.96	0.08	0.00	0.00
<b>S</b>	3.89	0.07	3.14	0.86	5.39	0.56	5.30	0.87	1.94	0.28	9.10	0.24
<b>Cl</b>	4.05	0.14	0.00	0.00	0.00	0.00	0.00	0.00	1.85	0.25	1.07	0.13
<b>K</b>	52.02	0.61	62.00	5.70	25.22	0.66	2.66	0.14	3.95	0.14	10.62	0.30
<b>Ca</b>	32.87	0.67	21.90	1.22	48.09	0.46	28.23	0.18	38.04	0.17	72.56	0.36
<b>Ti</b>	0.41	0.01	0.60	0.01	0.92	0.01	0.90	0.03	0.27	0.02	0.30	0.00
<b>Cr</b>	0.00	0.00	0.00	0.00	0.30	0.00	0.37	0.00	0.01	0.00	0.17	0.00
<b>Mn</b>	0.08	0.00	0.13	0.01	0.20	0.00	0.58	0.01	0.31	0.00	0.11	0.00
<b>Fe</b>	1.54	0.01	2.84	0.08	11.40	0.03	7.12	0.04	4.00	0.03	1.65	0.01
<b>Co</b>	0.78	0.01	2.32	0.24	0.00	0.00	0.00	0.00	0.00	0.00	0.00	0.00
<b>Ni</b>	0.28	0.00	0.67	0.01	0.08	0.01	0.19	0.01	0.00	0.00	0.03	0.00
<b>Cu</b>	0.00	0.00	0.20	0.02	0.20	0.00	34.73	0.05	36.83	0.08	1.10	0.00
<b>Zn</b>	0.05	0.00	0.07	0.01	0.14	0.00	4.69	0.11	2.22	0.08	0.11	0.00
<b>Pb</b>	0.00	0.00	0.00	0.00	0.00	0.00	0.00	0.00	0.00	0.00	0.01	0.00
<b>As</b>	0.20	0.00	0.76	0.17	0.00	0.00	2.38	0.01	0.91	0.00	0.00	0.00
<b>Sr</b>	0.10	0.01	0.09	0.02	0.10	0.02	0.00	0.00	0.00	0.00	0.07	0.01

for the definition of suitable conservation treatments. The structure and the paper support of both the primary and the backing layers were in discrete state of conservation so that a new lining of the artwork was not required. Such an important aspect has allowed the preservation of the original materials and structure of the handscroll and the limitation of infill and mending treatments, only localised areas of the paper support. The latter has represented a challenge under other points of view (due to preventing eventual mechanical stresses).

The restoration treatment began with an accurate cleaning of the surface of *recto* and *verso*, employing materials and techniques tested on small areas of the paper support before the cleaning treatment. The effects on the paper surface were assessed thoroughly with the help of a portable digital USB microscope (Jiusion USB Digital Microscope). Smokeoff sponges and QVC polyurethane sponges were chosen to clean respectively the surface of the verso

Table 2: : *Identified pigments.*

Colour	Chemical formula	Identified pigment
Red	HgS	Cinnabar/Vermilion
Green	Cu <sub>2</sub> (OH) <sub>2</sub> CO <sub>3</sub>	Malachite
Blue	FeK[Fe(CN)] <sub>6</sub>	Prussian blue
Orange	Pb <sub>3</sub> O <sub>4</sub>	Red Lead/Minium

Table 3: : *Identified pigments.*

	Point 1	Point 2	Point 3	Point 4
$\Delta E$	3.0	5.0	12.0	10.0
$\Delta W$	17.0	18.0	53.0	59.0

and recto of the handscroll <sup>20</sup>) (Fig. 6); the general aim of this step of the intervention was to remove incoherent dust and residues accumulated on the paper surface which usually are harmful carriers of fungi spores and pollution particles, while not altering the aesthetic properties of the artwork.

Restoration of the paper supports followed the cleaning treatment: this step was aimed to consolidate the abrasions caused by an entomological attack and to repair tears and losses of the primary and secondary support, localised especially in correspondence of the first sheets of the handscroll on the top and bottom edges. Multiple infills to the paper support were required to adjust the thickness of the repairs to the one of the original paper support (Fig. 7).

For the restoration treatments, starch glue is appropriately diluted and Japanese paper and tissue were used, adequately toned with watercolours. Tears caused by the previous housing system of the artwork, that had been hanging attached with metal pins, were repaired using Japanese tissue applied to the verso of the artwork, in order to maintain visible trace of the conservation history of the object, while assessing its consolidation. A large tear on the cover of the handscroll, in proximity of the *hassō*, required a different approach due to the more frequent and greater mechanical stresses to which the area is subjected: in this case different layers of Japanese paper were applied. The use of several layers of paper allowed the recovery of the integrated structure of the handscroll cover and the repairing of gaps, as can be seen in Fig. 8 and Fig. 9.

Table 4: : *Identified pigments.*

Consolidants	$\Delta E$	$\Delta L$
<b>Kluacel<sup>®</sup> G (1 %)</b>	5.4	1.1
<b>Funori (0.5 %)</b>	4.1	0.8
<b>Nikawa (1 %)</b>	3.6	0.7

For the consolidation treatment on the pictorial surface, a procedure was developed with the aim of avoiding any significant alteration on both the aesthetic and the mechanical properties of the paper support. The best consolidant for such application was studied in the laboratory tests and it was identified as the nikawa glue solution at 1% of concentration. The consolidant was applied to the surface of the painting through a compressed air sprayer, delimiting the treatment to the specific areas of the handscroll which presented decoesion and losses issues. For such application, paper masks were cutted out to isolate the damaged painted areas and to avoid as much as possible the dispersion of the adhesive over the support and the colours that did not require a consolidation treatment <sup>19)</sup> (Fig. 10).

During the drying process the paper support was kept under light weights and a light tension with the help of some magnets to keep the surface plain, as can be seen from Fig. 11. The artwork was kept under constant observation to monitor its conditions and to verify that did not occur any deformation or mechanical alteration of the paper support.

## 6 Conclusions

A colorimetric survey was performed on a colourful and written modern copy of a 14<sup>th</sup> century Japanese handscroll entitled Jizo Engi Jo. At the moment of the study, the 19th artwork presented several adhesion issues, mainly regarding the pigments, so that an urgent restoration procedure was needed. The results of FORS measurements allow the characterisation of colour palette of the handscroll, identifying the pigments used for the preparation of a laboratory mock-up for the identification of the best consolidants to employ to avoid further detachments of the pictorial apparatus of the Japanese handscroll. The outcomes of the presented work proved to be of great valuable for the characterisation of the materials of a particular oriental artefact as well



Figure 6: *Cleaning treatment on an area of the recto of the artwork, using QVC polyurethane sponges.*

as for the confirm of their historical reliability, coherent with the handscroll dating. Furthermore, the application of the results on the elaboration of a laboratory sample for the evaluation of the best consolidation materials showed the usefulness of the proposed approach in conservation and restoration fields.

## **7 Acknowledgements**

The authors would thank Dr. Loretta Paderni, Director of the Asian Department at National Prehistoric Ethnographic Museum Luigi Pigorini-Museum of Civilization, Prof. Laura Micheli from the Chemistry Department Laboratories of the University of Rome Tor Vergata for the artificial ageing of the samples and Prof. Luca Milasi from the University of Rome “La Sapienza” for the translation of the texts of the scroll.

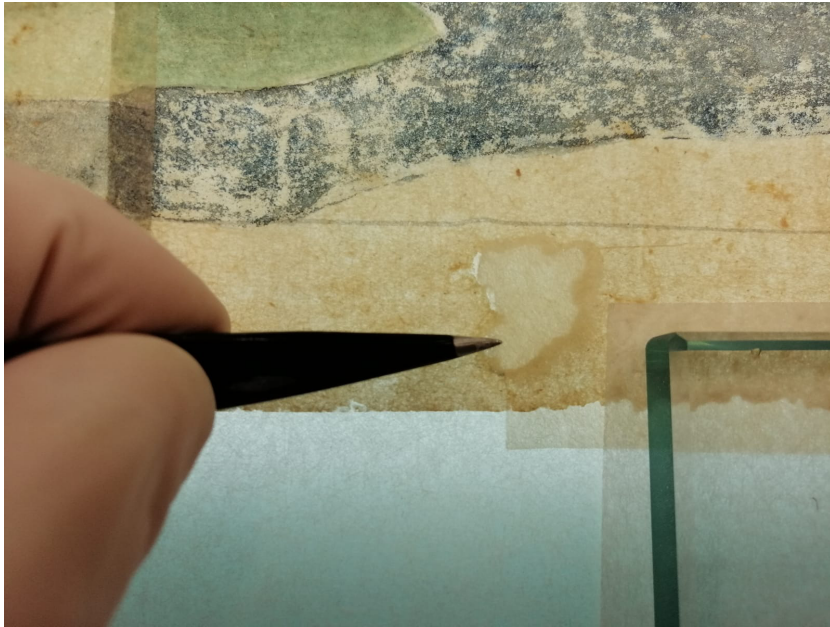


Figure 7: *Infill treatment with Japanese paper and glue starch.*

## 8 References

### References

1. M. Plossi Zappalá, La miniatura medievale su pergamena: la tecnica, i pigmenti, il supporto. *Kermes*, 12 (1991).
2. H. Okudaira, *Emaki: Japanese Picture Scrolls*. Charles E. Tuttle, (1962).
3. M. Aceto et al., *Analytical Methods* 6(5), 1488-1500 (2014).
4. M.L. Clarke et al., Imaging spectroscopies to characterize a 13th century Japanese handscroll, *The Miraculous Interventions of Jizō Bosatsu*. *Heritage Science* (2021).
5. L. Idjouadiene et al., *Journal of Cultural Heritage* 49, 289-297 (2021).
6. M. Leona and J. Winter, *Studies in Conservation* 46(3), (2001).



Figure 8: *The cover of the handscroll where a large damage is localized in proximity of the hasso (red rectangle) and many damages are dispersed on the surface (blue arrows).*

7. D. Radeaglia and M.V. Quattrini, *Il rotolo giapponese Bamodoizu - The Japanese Bamodoizu roll*, G. Editore (Ed.), (2014).
8. J. Winter, *East Asian paintings: materials, structures and deterioration mechanisms* (F. G. of Art, A. M. S. G. (Smithsonian Institution), & S. Institution (Eds.)). Archetype Publications (2008).
9. P. Wills, *The Paper Conservator* 9(1), 5-12 (1985).
10. J. Winter, *The Paper Conservator*, 9(1), 24-31 (1985).
11. G.F. Priori, and M.V. Quattrini, *La caratterizzazione delle carte orientali*, In *Bollettino ICR Nuova Serie*, 134-150 (2005).

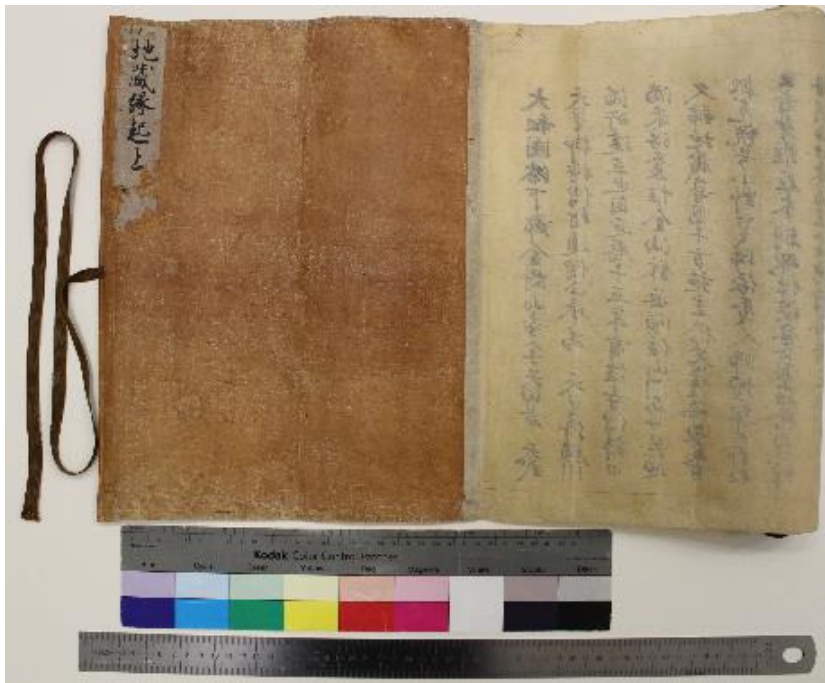


Figure 9: *The cover of the handscroll after the conservation treatment.*

12. M.V. Quattrini et al., *Studies in Conservation* 59, 328-340 (2014).
13. StellarNet FORS systems. (2021).
14. A. Aldrovandi et al., *Fiber Optics Reflectance Spectra (FORS) of Pictorial Materials in the 270-1700 nm range*, SABeC IFAC-CNR (2020).
15. E. Ganz and H.K.A. Pauli, *Applied Optics* 34(16), 2998 (1995).
16. C. Oleari, *Misurare il colore* (Hoepli (Ed.)) (2008).
17. D. Hampai et al., *X-Ray Spectrometry* 44(4), 243-247 (2015).
18. G. Cappuccio et al., *Radiation Physics and Chemistry* 188, 109660 (2021)
19. E. Hummert et al., *Restaurator* 34(2), 134-171 (2013).



Figure 10: *The consolidation treatment on the green and blue painted areas using a paper mask for its application.*

20. M. Daudin Schotte et al., *Analisi e applicazione di materiali per la pulitura a secco di superfici dipinte non verniciate*. Quaderni Cesmar7, (2011).



Figure 11: *Light weights and magnets used to keep the paper surface plain during the drying process.*

**A HIGH-QUALITY SINGLE-CRYSTAL CVD-DIAMOND  
DOSIMETER  
FOR HIGH ENERGY PHOTON BEAMS MONITORING**

S. Pettinato

*Università degli Studi Niccoló Cusano, via don Carlo Gnocchi 3, 00166 Rome, Italy*

A. Stravato

*"San Giovanni Addolorata" Hospital, Via dell'Amba Aradam, 8, 00184 Rome, Italy*

D. Hampai

*INFN - LNF, XLab Frascati, via E. Fermi, 54, 00044 Frascati (RM), Italy*

S. Salvatori

*Università degli Studi Niccolá Cusano, via don Carlo Gnocchi 3, 00166 Rome, Italy*

**Abstract**

The accuracy and efficacy of radiotherapy treatments are crucial for patients' proper and safe management. In this context, dosimetry plays a fundamental role in meeting the demands of quality assurance of performed treatments. In particular, fast X-ray detectors coupled with appropriate front-end electronics are required for real-time monitoring of high-energy X-ray beams used in radiotherapy. This work proposes a detection system based on a diamond dosimeter and dedicated front-end/read-out electronics to measure the dose released by each individual pulse from a linear accelerator delivering X-ray beams at 6 MeV. The system integrates the signal generated by the dosimeter in a time interval around the single pulse, thus assuring good measurement accuracy and real-time pulsed beam monitoring. The performance of the dosimeter was verified in the 0.1-5 Gy dose range and compared to that of an ionization chamber by acquiring the signal with a commercial electrometer. The device showed excellent response linearity with both the dose and the dose rate with a sensitivity of  $(301 \pm 0.002)$  nC/Gy. Pulse-by-pulse measurements performed

with the proposed synchronized electronics under the same experimental conditions demonstrated the feasibility of a diamond-based detection system able to effectively monitor the pulsed X-rays employed in modern radiotherapy techniques.

## 1 Introduction

Accurate dosimetry is a crucial prerequisite for successful and effective radiotherapy (RT) treatments. Dose measurements are a key element in both the definition of treatment plans and the calibration of radiation beams delivered by the medical linear accelerator (LINAC). Nowadays, modern conformal and dynamic radiotherapy techniques (i.e. Intensity Modulated RT, IMRT, or Volumetric Arc RT, VMAT <sup>1, 2</sup>) allow for the modulation of RT beams, ensuring a more uniform dose distribution also on an irregularly shaped target tissue (tumor volume) and better safeguarding healthy tissues. Both IMRT and VMAT techniques employ small field sizes, high dose gradients and space-time modulation of the radiation beam. Precisely define the dose delivered in modern dynamic and conformal techniques becomes pivotal in ensuring the best patient treatment. Highly qualified personnel and the use of special dose measuring instruments are the two cornerstones in defining the best treatment plan for the patient. Therefore, the application of dosimeters capable of detecting the released dose with high accuracy plays a key role. Particularly, dosimeters employed in the RT field must meet the requirements defined by the International Atomic Energy Agency (IAEA <sup>3</sup>): stability over the irradiation time; low settling time in the beam on-off transients; response linearity with both the dose and the dose rate; adequate sensitivity (i.e. collected charge per unit of administered dose) in the applied dose range.

LINACs employed in RT generate high-energy X-ray pulses with a duration of a few microseconds, at a pulse repetition frequency of a few hundreds of Hz. Ionization chambers (ICs) are considered the gold standard for dose measurements. Medical physicists use ICs coupled with electrometers for beam calibration in the clinical routine. However, the charge-collection time of ICs ranges from  $10^{-5}$  s to  $10^{-4}$  s <sup>4</sup>, and the integration time of precision electrometers is within 10-100 ms <sup>5</sup>.

Therefore, dose measurements are performed in time periods in which sev-

eral pulses are integrated, thus making real-time, pulse-by-pulse monitoring of the delivered dose impractical/unfeasible. Showing a response time in the order of ns <sup>6, 7)</sup>, diamond represents an excellent solution for the fabrication of fast solid-state detectors for RT dosimetry <sup>8)</sup>. Therefore, diamond detectors coupled to specific front-end electronics will represent a good solution for real-time monitoring of X-ray beams, especially for modern RT techniques. In addition, diamond has special physical-chemical characteristics that make it particularly appealing for dosimetric purposes. First of all, it is a tissue-equivalent material ( $Z=6$ ) <sup>9)</sup>; it is resistant to radiation damage (up to 10 MGy <sup>10)</sup>); it has a high cohesion energy (43 eV); and above all it shows a linear response with both dose and dose rate (DR) <sup>11)</sup>. Diamond also allows the fabrication of dosimeters with very small active volumes (lower than 1 mm<sup>3</sup>), which is a necessary requirement for dosimetry with small fields, such as those used in IMRT and VMAT. Thanks to advances in the development of Chemical Vapor Deposition (CVD) techniques, high-quality diamond samples, with impurity concentrations three orders of magnitude lower than those of the best natural diamond, are now available <sup>12)</sup>. Dosimeters based on CVD-diamond are now a mature and established technology for RT <sup>13, 14, 15, 16, 17)</sup>, and they are commercially available <sup>18)</sup>. On the contrary, detection systems for single-pulse monitoring used in radiotherapy is still lacking. Proposed solutions in the literature are mainly focused on scintillator- and fiber-optics-based dosimetry <sup>19, 20)</sup>. However, these types of dosimeters require relatively complex optical detection systems also employing Cherenkov radiation removal techniques <sup>21)</sup> proposed a prototypal system for single-pulse measurements based on diamond and developed a dedicated front-end electronics for signal processing. Such solution requires relatively complex electronics for the pulse height processing. Moreover, the detection system exhibits a response time of several milliseconds, thus resulting ineffective for fast detection solutions.

In this work, experimental results of a specifically assembled CVD-diamond dosimeter coupled to a tailored front-end/read-out electronics for pulse-by-pulse monitoring of the X-ray beam are reported. A diamond dosimeter was fabricated and its characteristics were evaluated both under continuous, low-energy X-ray irradiation and under high-energy X-rays generated by a medical LINAC. The signal of the dosimeter was acquired with a precision electrometer and results were compared with those provided by an ionization chamber. In

addition, a specifically developed synchronized front-end/read-out electronics, described in more detail in <sup>22, 23</sup>, was used to demonstrate the dose-per-pulse measurement capability of the proposed prototypal detection system.

## 2 Dosimeter fabrication

A  $4 \times 4 \times 0.5 \text{ mm}^3$  CVD single crystal optical grade (Element Six) diamond sample was used to fabricate the dosimeter. On the top and bottom faces of the sample, 300 nm thick Ag contacts were deposited by means of sputtering deposition technique. The geometry of the contacts with a radius of 1.6 mm was defined by means of a shadow mask. The active volume therefore of the diamond dosimeter is approximately  $4 \text{ mm}^3$ . Figure 1(a) shows a sketch of the detector. Two thin wires were glued with silver paste to the metal contacts and then soldered to the outer shield on the inner conductor of a 3.6 m long triaxial cable. Finally, the detector was encapsulated in a PMMA cylinder (diameter 9 mm, length 5 cm) and the free volume inside the PMMA case was filled with epoxy resin (Epotek<sup>®</sup> 301). Figure 1(b) shows a picture of the encapsulated dosimeter connected to triaxial-cable, whereas Figure 1(c) reports an X-ray scan image of dosimeter (dotted lines highlight the diamond plate edge).

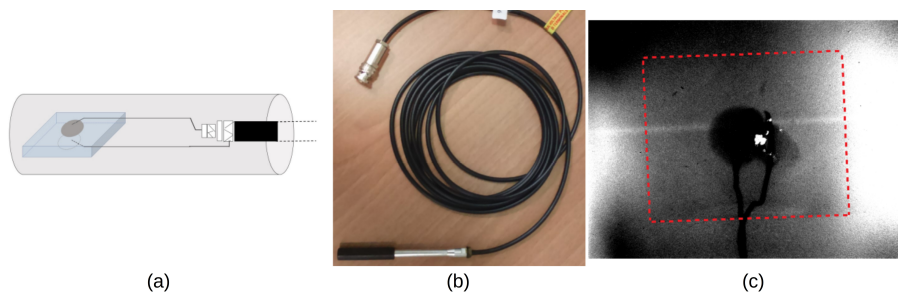


Figure 1: (a) Sketch of the geometry and the configuration of contact on the diamond sample. (b) Picture of the waterproof housing with triaxial connector. (c) X-ray scan of the encapsulated dosimeter.

### 3 Preliminary results with continuous low energy X-rays

After encapsulation, a preliminary characterization of the dosimeter under a continuous, low-energy X-ray beam was performed. A Coolidge tube (Oxford Apogee 5500) with a Cu target was used for this purpose. The X-rays produced by the Coolidge tube are characterized by a composite emission spectrum. The emission is given by the superposition of a continuous spectrum (braking radiation or Bremsstrahlung) and the two spectral characteristic lines of the target material,  $K_\alpha$  and  $K_\beta$ . In the case of the Cu target,  $K_\alpha$  and  $K_\beta$  are at 8.05 keV and 9.2 keV, respectively. No filter has been placed between the dosimeter and the source during the tests, thus allowing the dosimeter to collect also the Bremsstrahlung radiation. A collimator of radius 0.5 mm was placed 10 cm from the source to direct the radiation onto the dosimeter. The dosimeter was placed 12 cm apart from the collimator, resulting in a radiation spot with a diameter of approximately 1.8 mm impinging on the detector.

The detector photocurrent was measured with a Keithley 6517A electrometer in picoamperometer mode, simultaneously used for device biasing (10 V). The X-ray source was powered at 40 kV. Figure 2 shows the data recorded by varying the Coolidge tube-current in the 0.018-1 mA range. The dosimeter was irradiated for approximately 300 s at each current tube value. Data display an excellent linearity of the photocurrent generated by the dosimeter as a function of the tube current. However, work is in progress to assess the responsivity (i.e. the ratio between the photocurrent and the impinging dose-rate) of the dosimeter by measuring the dose-rate of the Coolidge tube at each current value.

## 4 Characterization under high-energy X-rays

### 4.1 Medical LINAC

Linear accelerators (LINACs) are the apparatuses currently used in External Beam RT (EBRT), capable of produce high energy radiation beams, either electrons or photons, typically from 4 MeV to 25 MeV. To produce MeV photons, high-energy electron packets are accelerated to collide with a heavy metal target. The electrons lose their energy on impact with the metal target, thus producing X-rays by Bremsstrahlung effect. A modulator delivers pulses of a few microseconds in duration to a magnetron or a klystron, as well as to the

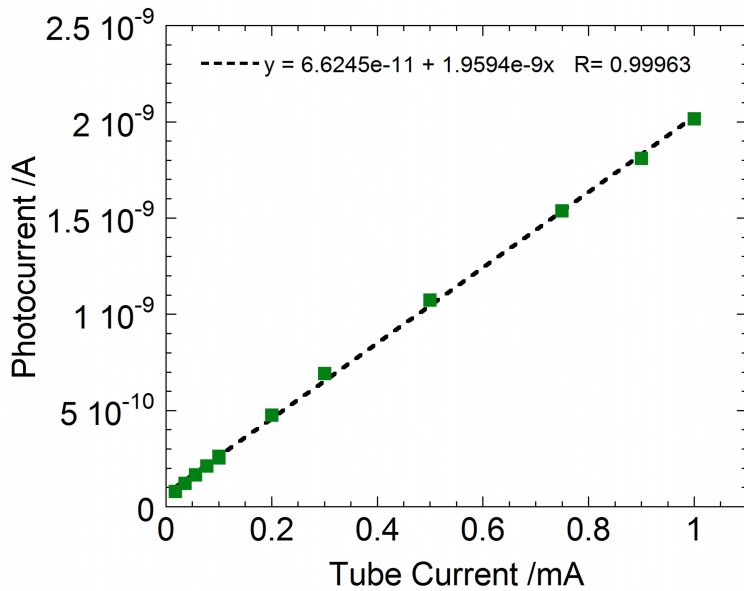


Figure 2: *Phocurrent generated by the detector as a function of tube current at a fixed voltage of 40 kV.*

electron gun. The microwave pulses produced by the generator are injected into the electron accelerator tube. The electron gun is the source of electron packets. By means of the modulator, electrons are grouped into pulses and not injected continuously in the accelerator tube. In the same time, the modulator drives the microwave power that is sent to the waveguide in short pulses of about 4  $\mu$ s durations. Then, each generated pulse has a duration of about 4  $\mu$ s while the time interval between consecutive pulses is of a few milliseconds. Electrons are injected into the accelerating structure by the electron gun with a kinetic energy of about 50 keV. The injected electrons interact with the microwaves and they gain the required energy to impinge on the target to produce X-rays. The electrons that escape from the accelerating structure enter the "treatment head" composed by a set of systems having the function to collimate, to conform, and to monitor the radiation beam. The electron beam is firstly deflected by an angle of 90° to be oriented towards the patient

placed on the treatment bed. The output of the machine, i.e., the dose rate, is established by the pulse repetition rate, as well as the peak current of the pulse. This is of the order of 1 mA if the LINAC directly sources electrons and about 100 mA for the production of X-photons.

## 4.2 Results

The diamond dosimeter photoresponse was evaluated under pulsed X-rays produced by a medical LINAC Clinac iX (Varian, Inc) installed at the Radiation Oncology Department of the "San Giovanni - Addolorata" Hospital in Rome (Italy). An electron acceleration voltage of 6 MV was set, so the X-rays exiting the tungsten target by Bremsstrahlung effect had an energy in the range of 0-6 MeV.

The tests were carried out under standard conditions: to ensure the electronic equilibrium, the dosimeter was placed in a Plexiglass<sup>®</sup> phantom<sup>24</sup>). The phantom was centered so that the active volume of the dosimeter was at the isocentre of the LINAC and at a surface source distance of 100 cm. Figure 3 shows a sketch of the set-up used during the dosimeter characterizations. A field of 10x10 cm<sup>2</sup> was used during the tests and the impinging photon beam direction was perpendicular to the diamond plate surface.

The tests were performed by acquiring both the charge and the photocurrent generated by the dosimeter using a Keithley 6517A electrometer. The set-up used is therefore the one typically employed by medical physicists in their clinical routines. The Keithley 6517A electrometer was used both as source to provide the bias voltage of 10 V to the dosimeter and to measure either the charge or the photocurrent generated by the detector. Measurements have been performed at DR = 3 Gy/min, in the range 0.1-5 Gy of delivered dose. The experimental results are reported in Figure 4, green squares (error bars are smaller than symbols). An excellent linearity in the investigated dose range was found. The dosimeter sensitivity estimated from the slope of the charge-dose characteristic is  $(301 \pm 0.002)$  nC/Gy.

To calibrate the diamond dosimeter, the dose measurements were repeated under the same experimental conditions substituting the diamond detector with a Farmer FC 65-G ionization chamber (IBA Dosimetry). The results are reported in the same Figure 4 (orange squares). The IC signal was acquired with a Scanditronix Dose 1 electrometer (IBA Dosimetry), thus employing the

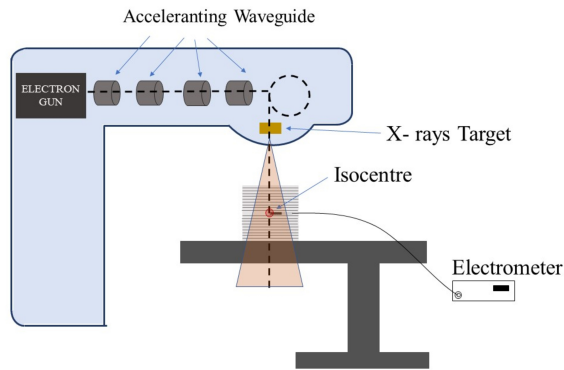


Figure 3: Schematic of the measurement set-up used for dose measurements under X-rays generated by the LINAC. The dosimeter was placed inside a PMMA phantom and positioned at the isocentre of the machine.

same instruments used at the Radiotherapy Department by medical physicians during their periodic calibration procedures. The measurements with the IC were performed in the dose range 0.2-20 Gy. As illustrated by experimental results of Figure 4, both the devices display an excellent linearity. In addition, the sensitivity of the IC results equal to  $(17.80 \pm 0.002)$  nC/Gy. It is worth noting that the ratio between the photoresponses of the two detectors is constant and equal to  $(17.01 \pm 0.02)$ , thus confirming the excellent quality of the fabricated diamond dosimeter.

Dose rate dependence of the diamond detector was investigated over all available DRs of the Clinac iX. Characterizations were then performed by measuring the photocurrent amplitude  $I_{ph}$  with the Keithley 6517A as a function of the dose-rate under 6 MeV photons in the range 1-6 Gy/min. At each dose-rate, the X-beam was switched on for about 60 s and then switched off for about 40 s before setting a new DR value. Figure 5 shows the mean values of the diamond detector photocurrent at each DR (green squares). For comparison, the measurements were repeated in the same experimental conditions with the Farmer FC 65-G ionization chamber acquiring the photocurrent with Scanditronix Dose 1 electrometer (orange squares).

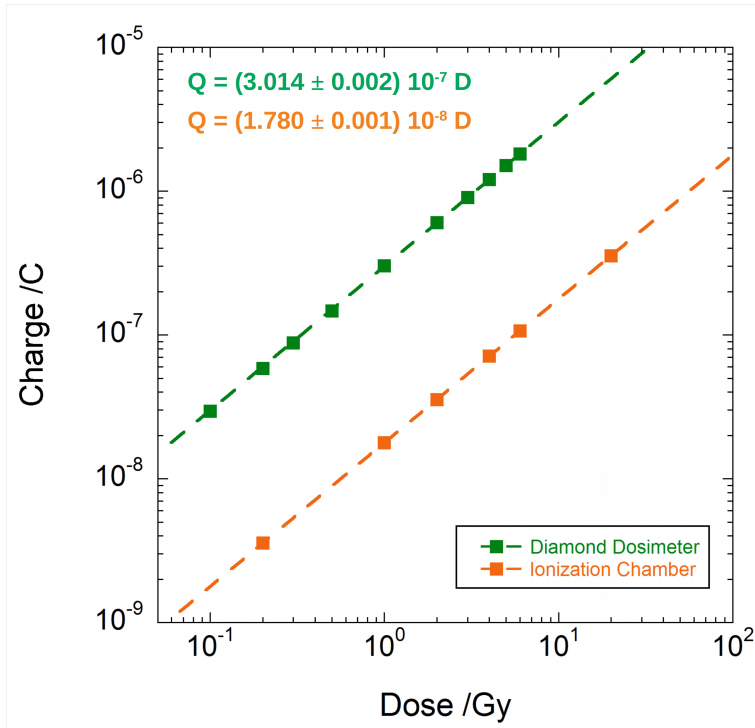


Figure 4: Charge as a function of dose acquired for 6 MV X-photon beam with both diamond dosimeter (green squares) and ionization chamber (orange squares).

One way of testing for dose rate dependence of a detector is by using the Fowler's law <sup>25)</sup>, where the induced photocurrent signal is proportional to the absorbed DR:

$$I_{ph} = k \cdot DR^{\Delta} \quad (1)$$

where a power law regression is used with fitting parameters  $k$  and  $\Delta$  (ranging from 0.5 to 1) to test for linearity. Best fit of data according to Equation 1 (dotted lines in Figure 5) give an exponent slightly lower than 1 for both the diamond detector and the IC. The proportionality factor of about  $5.0 \text{ nA} \cdot \text{Gy}^{-1} \cdot \text{min}$  found for the diamond dosimeter gives a current of 14.64 nA at

a DR equal to 3 Gy/min, i.e. a value of about 301 nC for 1 Gy of dose, in excellent agreement with the sensitivity estimated by charge-dose measurements performed at DR = 3 Gy/min (Figure 4). As expected, the responsivity of the diamond detector is about 17 times that evaluated for the IC, as also found for the sensitivities of Figure 4.

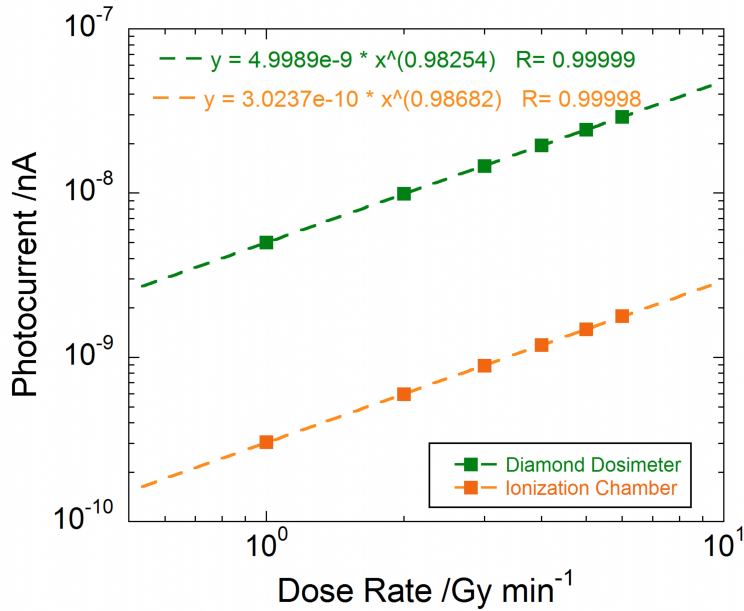


Figure 5: Photocurrent as a function of DR acquired for 6 MV X-photon beam with both diamond dosimeter (green squares) and ionization chamber (orange squares). A slight sub-linear behavior was recorded for both devices.

## 5 Front-end electronics for pulse-by-pulse dose monitoring

As aforementioned, in the LINAC, electron packets are accelerated to collide on the heavy metal target, thus producing pulsed X-rays by Bremsstrahlung effect. As already stated, electron packets have a duration of few microseconds, with a repetition rate up to several hundreds of Hz. The resulting X-rays are then repetitive with a very low duty cycle (of the order of 0.1%). The sync

signal, available at the LINAC control console, synchronizes all the components involved in the control of the electron bunches: from their generation by the thermionic gun to the input in the waveguides where they are accelerated. For the Clinac iX, after 12  $\mu\text{s}$  from the sync signal, the apparatus generates a current peak (target signal) induced by the electron packet impinging on the tungsten target, thus producing the X-rays pulses <sup>11, 23</sup>).

The sync signal allows performing gated-integration measurements, synchronizing and limiting the integration to a period centered on the pulse duration, thus increasing the measurement accuracy and enhancing the signal-to-noise ratio. In radiation dosimetry, the detection system must be able to assess the absorbed doses from ionizing radiation. Therefore, it is important to know the total amount of charge generated in a detector. The main feature of the front-end/readout electronics should be the ability to convert all the charge or current generated by the detector into a proportional voltage signal. To this purpose, integration of collected charges represents a feasible as well as simple solution for single-pulse signal conditioning. Figure 6 shows the block diagram of the proposed synchronized electronics tailored for effective pulse-by-pulse acquisition of the photocurrent peaks generated by a diamond dosimeter. The front-end electronics is based on the high-precision switched integrator transimpedance amplifier IVC102 (Texas Instruments). The State Configurable Timer (SCT) integrated in the LPC845 microcontroller (NXP Semiconductors) was used to generate the digital control signals to drive the two MOS switches of the IVC102 integrator. This allows the integration to be synchronized to the single pulse. Hence, the timer was programmed to determine the start and end of the integration around the single X-ray pulse. A fast amplifier is inserted between the output of the IVC102 and the analog-to-digital converter (ADC) to attenuate or amplify the IVC102 output voltage. In this way, the system can be adapted to the detector signal according to the specific working condition.

The sync signal from the control console of the LINAC (located outside the bunker) was brought to the input of the front-end electronics (located inside the bunker to avoid degradation on the response time of the detector) via a 20 m long coaxial cable terminated at 50  $\Omega$ . The instruments have been remotely controlled with a specifically developed LabVIEW program installed in a computer located in the bunker and interfaced to a remote computer with

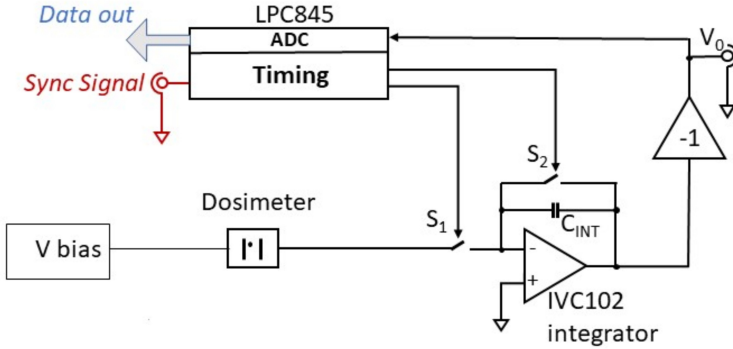


Figure 6: Block diagram of the front-end/read-out electronics specifically developed for the acquisition of the dose released pulse-by-pulse.

a LAN cable.

The characterization of the diamond detector coupled to the synchronous electronics was performed using the same set-up described in the previous section. The DR was fixed to 3 Gy/min and measurements were performed in a wide dose range: from 0.3 mGy (single pulse) to 10 Gy (i.e. 200 s of irradiation, corresponding to about 36000 pulses). The  $Q_p$  charge per pulse value was calculated according to:

$$Q_p = \frac{C_{INT} V_{ref}}{4096} N \quad (2)$$

where  $C_{INT}$  is the feedback capacitance of the IVC102 (100 pF of nominal value),  $V_{ref}$  is the ADC reference voltage, and  $N$  is the 12-bit output value of the ADC. A proper laboratory calibration procedure was performed to evaluate the  $C_{INT} V_{ref}$  product<sup>26</sup>). Collected charge is given by the sum of acquired  $Q_p$  over the irradiation time. As shown in Figure 7, an excellent linearity of the charge collected by the dosimeter as a function of the delivered dose has been found. The cumulative charge  $Q(D_m)$ , for a number  $m$  of impinging pulses with an expected dose equal to  $D_m = m \cdot D_P$ , with  $D_P$  the mean value of dose-per-pulse, was calculated as:

$$Q(D_m) = \sum_{i=1}^m q_i \quad (3)$$

with  $q_i$  indicating the charge measured by the instrument on every single pulse.

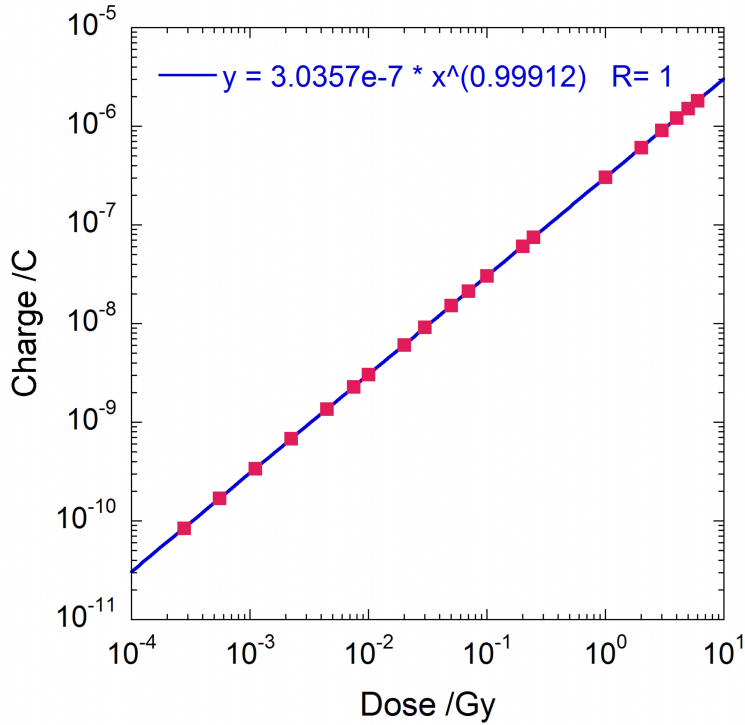


Figure 7: Collected charge as a function of dose for X-ray photons emitted at 6 MeV.

By best fit of data reported in figure 7 (continuous line), the evaluated diamond dosimeter sensitivity is  $(303.57 \pm 0.02)$  nC Gy $^{-1}$ , in excellent agreement with the sensitivity value estimated in the preliminary characterization performed with the electrometer. It is worth to note that the difference between the slopes of data acquired by the realized front-end/readout electronics and the 6517A electrometer is lower than 0.2%, highlighting an excellent agreement between the two instruments and thus the effectiveness of the designed system.

## References

1. M. Khan, J.P. Gibbons, Intensity-Modulated Radiation Therapy. In Khan's The Physics of Radiation Therapy, 5th ed., Lippincott Williams & Wilkins, 430-189 (2014).
2. M. Teoh *et al*, Br. J. Radiol. 84, 1007, (2011).
3. World Health Organization. "Absorbed dose determination in external beam radiotherapy. An international code of practice for dosimetry based on standards of absorbed dose to water." (2004).
4. P.T.W. Freiburg, Ionizing Radiation Detectors: Including Codes of Practice, 100 (2013).
5. Electrometer, R.C. High-Performance Dual-Channel Reference Class Electrometer 2.
6. M. Girolami *et al*, Proc. IEEE Sensors (2008).
7. S. Salvatori *et al*, Laser Phys. 26, 8 (2016).
8. C. Talamonti *et al*, Front. Phys. 9, 632299 (2021).
9. B. Gorka *et al*, Phys Med. 24(3), (2008).
10. T. Eberl *et al*, Nucl. Instrum. Methods Phys. Res., A, 502 (2003).
11. S. Pettinato *et al*, IEEE Sens. Jour., 22(12) (2022).
12. Element Six, Diamond Handbook.
13. C. Descamps *et al*, Rad. Meas. 43(2-6) (2008).
14. S.Almaviva *et al*, Nucl. Instrum. Methods Phys. Res. Sect. A Accel. Spectrometers Detect. Assoc. Equip, 608 (2009).
15. F. Marsolat *et al*. Phys. Med. Biol. 58 (2013).
16. M.A. Piliero *et al*, Radiat. Phys. Chem. 104 (2014).
17. G. Prestopino *et al*, Materials Science Forum 879, (2017).

18. PTW, "microDiamond Synthetic Diamond Detector for High-Precision Dosimetry" (2016).
19. M.R. Ashraf *et al*, Phys. Med. Biol., 67, 9 (2022).
20. A.R. Beierholm *et al*, Radiat. Meas., 45, 3–6 (2010).
21. J.J. Velthuis *et al*, IEEE Trans. Radiat. Plasma Med. Sci. 1, 6 (2017).
22. S. Pettinato *et al*, Single-Pulse Measurement Electronics for Accurate Dosimetry in X-ray Radiation Therapy, in Proc: IEEE International Symposium on Medical Measurements and Applications (MeMeA), (2021).
23. S. Pettinato *et al*, Materials, 14(18), (2021).
24. G.F. Knoll, Radiation Detection and Measurement, 4th ed., Hoboken, NJ, USA: John Wiley & Sons, Inc., 167-169 (2010).
25. J. Fowler, Solid state integrating dosimeters, in: F. Attix, W. Roesch, E. Tochilin, G. Hine (Eds.), Radiation Dosimetry, Academic Press, New York, 290 (1966).
26. S. Pettinato *et al*, Sensors, 22(14) (2022).

## **PELTUINUM: THE ROMAN CITY AND THE INTERDISCIPLINARY FIELDS**

L. Migliorati

*Dip. Scienze dell'Antichità, Univ. Sapienza, Rome, Italy*

### **Abstract**

Peltuinum is a Roman city in the L'Aquila Apennines. Its history is linked to the earthquakes of this highly seismic region and in fact ends as an urban reality following the earthquakes recorded in the fifth century A.D. However, the area continues to be inhabited through scattered nuclei. The contribution of other specific skills to research on the city proves to be indispensable for facing the development of a society at 360 degrees.

### **1 Peltuinum: the Roman City**

Peltuinum is a city that the Romans built in the Apennine area within the region inhabited by the Vestini population; today the ancient vestino district belongs to the province of L'Aquila. The geographical indication of the urban



Figure 1: *Peltuinum within the trattural network of central-southern Italy.*

center immediately refers to both seismic phenomena and transhumant routes, vectors of the periodic movement of herds between Sabina and Puglia, Fig. 1.

These two elements condition the life and the end of the city, while its birth is linked only to the cattle track. In fact, the "via delle greggi", which crossed the intramontane basins overcoming the natural connection bottlenecks, had found in the plateau on which Peltuinum will rise, almost 900 m above sea level, a comfortable stopping point since the dawn of transhumance <sup>1, 2</sup>), stop favored by the presence of at least one pool of water. The emergence of an aquifer at a high altitude, compared to the springs present 100 m below, in the plain from which the plateau stood out, led to the sacralization of the place already in the pre-Roman age <sup>3</sup>). It is clear that the aquifer outcrop is linked to the geological structure of the plateau consisting for most of the area of alternating layers of more or less cemented silt and gravel, with the occasional presence of thin sandstone blades, while in the north-western sector marine limestone is attested <sup>4, 5, 6</sup>). The presence of these geological strata conditions, as usually occurs, the building structure of the Roman city, which

is constantly characterized by the use of the material available on site both for public buildings, including infrastructures, and for private ones: limestone for square, reticulated, blocky; silt for pisé and as a flooring component; gravel for the roads and the square, but also, using very small-grained elements, as an ingredient in the mortar <sup>7)</sup>. The testaceous material is reserved only for the roofing, mostly made in tiles; in fact, a consistent presence of tiles can be seen only in the theater area, probably with specific relevance to the scenic building. Going back to the origin of the Roman centre, the urban codification takes place in the middle of the I century BC, coinciding with the awareness acquired by the *res publica* of the high economic value that the management of transhumance could have. And in fact the city was built astride the sheep track, which became the main crossing axis of the urban surface; this obviously includes the whole plateau, with a line of defenses that runs along the tactical edge and shows great strategic attention especially for the north-western sector, the weakest because it is the least steep, see Fig. 2.

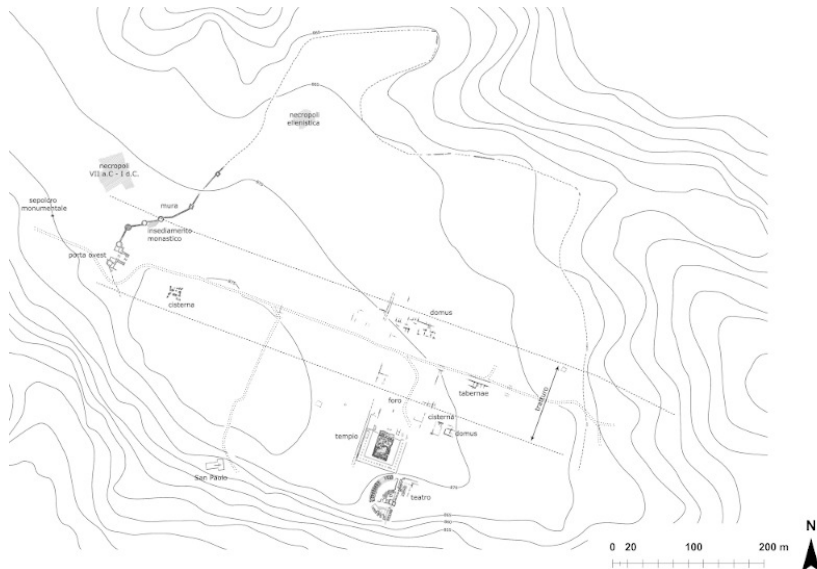


Figure 2: *Archaeological map on morphology.*

The high seismicity of the area is clearly denounced by the public struc-

tures, while an implicit testimony can be read in the building technique used in the houses, which seems to indicate the use of anti-seismic measures and therefore a knowledge of the phenomenon prior to the foundation of the settlement. In fact, the residual walls of the residential complexes are built with a plinth in limestone elements, while the upper part is in silt mixed with vegetable fibers with probable insertion of wooden components; this appears to be a constructive system adopted to make the walls more elastic and more resistant to shocks, but also more easily restored. The public buildings currently in light are the walls, the podium of the forensic temple and the theatre, Fig. 3.



Figure 3: *The plateau of the Roman city from the east (drone photo by A. Vecchione). 1, wall; 2, temple and triportico; 3, theater; 4, church of S. Paolo.*

The greater architectural complexity, size and political significance of these have led to the use of different materials and different construction techniques; all the works (square, reticulated, in blocks, uncertain) use limestone for the entire construction. In this case the action of earthquakes generates different effects. Starting from the fortifications, the festooned collapse that characterizes the preserved sector is already very eloquent in itself, while as regards the forensic temple and the theater, the investigations of excavation. It is important to underline that only earthquakes that have had consequences,

more or less disastrous, on structural organisms, or that have left traces in the archaeological stratigraphy can be recognised, but, remembering the geographical location, the number of such events will undoubtedly have been very high

In summary <sup>8, 9)</sup>, a first strong earthquake after the foundation of the city is placed under the emperor Claudius. Stratigraphic excavations have documented that the forensic complex and the theater (Fig. 4), then still under construction, suddenly undergo project changes. With regard to the forum, the temple, whose decoration attests to an Augustan construction <sup>10, 11)</sup> and therefore in coherence with the first urban phases, is perhaps the work that did not suffer very important damages; the solid cement podium may indicate that the designer, as an anti-seismic measure, relied on the weight of the podium to keep the center of gravity of the structure low, in order to mitigate the seismic effect of the inverted pendulum.



Figure 4: *The forensic complex and the theater from the north (drone photo by A. Vecchione).*

A nearby building must have suffered very different effects: its construction was interrupted while it was still in the construction phase, the walking

surface was raised by about thirty centimeters and on this a new building program was implemented, which envisages an expansion of the surface of the square itself and the consequent movement, to the limits of the extension of the area, of a new complex which, from the remains investigated for now, appears to have a more massive structure. In essence, the monumental framework of the forum square is modified in various respects. In fact, it is possible that the three-armed portico that frames the temple also belongs to this variant of the project, as both the autopsy examination and some preliminary results of the analysis of the wall paintings seem to indicate (Fig. 5).



Figure 5: *Triportico: sector of the western site with plaster and paint residues.*

As far as direct observation is concerned, it is most likely possible to hypothesize the decorative scheme only for the lower section of the wall, given the state of conservation of the walls of the triportico; the study points towards the second half of the first century. AD, with maximum opening at the beginning of the II, but with analogies of schemes and composition referable to the foundation of Aventicum by Claudius. A decisive contribution can be given by the comparative reading with the analyzes that are underway by INFN LNF, XlabF with the use of the X-ray diffraction technique <sup>12</sup>). In fact, it is through the close comparison between specialists of the various disciplines that scientifically reliable results are achieved. It is a pleonastic statement, but it is good to remember it.

The same seismic phenomenon had heavy effects on the theater built on the natural terrace below the one where the forum had been planned. The deci-

sion to locate the building at that point was dictated by the need to concentrate the solution to various problems in the construction (Fig. 6). Exploitation of the slope for the support of the steps for a large stretch of the cavea involved a saving of work, i.e. manpower, material, financial commitment, as it was sufficient to shape the ground before laying the blocks for the steps ; at the same time the shape of the theatre, with a horizontal arch, constituted an effective counter-thrust system for the upper terrace burdened by the weight of the temple-portico complex and potential slipping; in addition, a side of the plateau was covered which exposed a fragile soil to atmospheric agents, because it was formed by the aforementioned layers of silt and almost loose gravel that were easily subject to erosion.



Figure 6: *Theater and temple from the south (drone photo by A. Vecchione). The counterthrust function of the theater is evident.*

Furthermore, the exploitation of the slope directed the orientation of the

cavea towards the east and this also made it possible to obtain a *porticus pone scaenam*, with the classic function of foyer, with at least two arms, one parallel to the scenic building and the other, orthogonal, with a wall bottom which also worked as a containment of the upper terrace, in continuation of the role played by the cavea. Investigations in this specific sector have revealed the same situation present in the forum: a construction site in progress interrupted by a sudden event and a reconstruction with abandonment of the construction in progress, the raising of the walking surface, in this case by 75 cm, and the modification of the intervention of the original planning, giving up an arm of the portico, but consolidating the function of buttress that the back wall of the portico itself had. The variant of the project is also clearly visible in the structure of the theater itself; the consolidation took place through the addition of a semi-circular ring external to the primitive construction connected to a network of walls which also had the constructive function of the *summa cavea*; in addition, the chambers created were filled with earth (Fig. 7). The changes also had the consequence of increasing the number of seats for spectators <sup>13, 14</sup>).

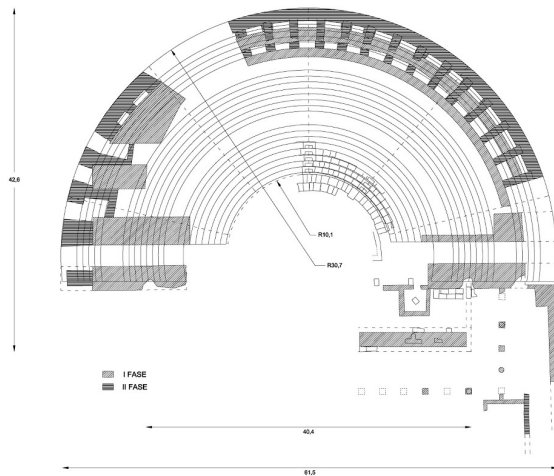


Figure 7: *Construction scheme of the theater* <sup>13)</sup>.

It is not of secondary importance to have found evidence of an earthquake that occurred in the central Apennine area in the Claudius reign, since the only

record of the event was limited to Rome and only on a historical-epigraphic basis 15, 16, 8). As often repeated, Rome feels the effects of earthquakes which mostly originate in the central Apennines and the new data from the excavations conducted at Peltuinum could be further confirmation. The reconstruction and restoration interventions in the city are probably part of Claudio's interest in this area of central Italy in which he was operating, using the skills of the army, for the regulation of Lake Fucino 17, 18, 3). Returning to the theme of interdisciplinary cooperation, the final results of the quantitative analyzes underway on the painting and plaster of the forensic portico could confirm the hypothesis on the presence in the central Apennines of the same soldiers who had been engaged in the foundation of the *Aventicum* (Avenches) colony.

Generically, in an urban area, the coexistence with minor seismic phenomena is documented by some restoration episodes. Subsequently, epigraphic and archaeological data attest a strong earthquake in southern Samnium in the mid-4th century A.D. It is not certain that this event involves northern Samnium, therefore also Peltuinum; it is certain instead that the life of the city comes to an end at the end of the 5th century, coinciding with the earthquakes of 443 and 484 19), known for the strong repercussions they had on the Colosseum 8).

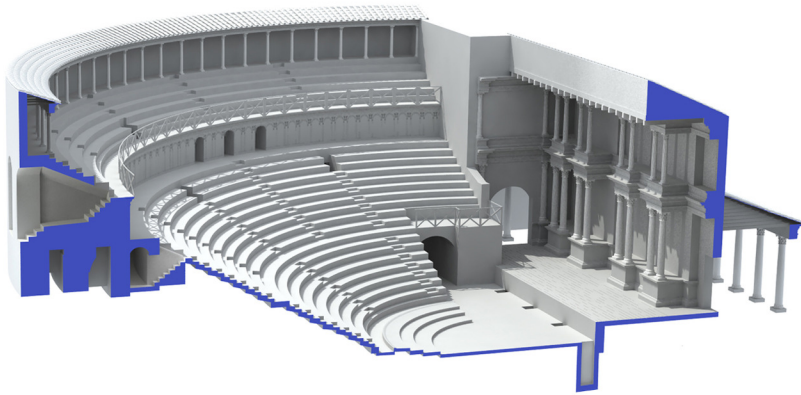


Figure 8: *Theatre: 3D reconstruction 13). In the foreground, on the right, the section of one of the wells related to the raising of the curtain.*

It is again the theater that offers particularly interesting data for a debate on the seismic events chronology mentioned. As is documented in many theatres, wells were built at the foot of the stage wall to house poles to which the curtain was tied, which was lowered at the beginning of the performance and raised to close the scene (Fig. 8). At Peltuinum, the filling of the wells yielded bone remains of human and newborn fetuses, dogs and other animals as well as building materials (Figs. 9-10). Also in this case a series of collaborations has been activated with physical anthropologists, geneticists, biologists, archaeozoologists. Osteological analyzes were able to reconstruct the presence of 87 human fetuses and newborns associated with the remains of 68 dogs and other domestic animals, including horses.



Figure 9: *Building materials inside cockpit IV.*

The whole context (20, 21) suggests the use of wells as a common deposition area for newborns, stillborns, fetuses, not yet part of society and therefore

not suitable to be buried with adults. The presence of dogs, mostly puppies, finds analogies in various situations and is widely explained.



Figure 10: *Bone remains (infant and dog) in well VI.*

On the other hand, the preliminary paleogenetic analysis of some infants offered a very interesting picture of the family groups composition in the area. The whole must be studied in depth in order to be able to reconstruct the life of society in rural areas in the late antiquity period. A further element for the advancement of research concerns the radiocarbon dating of the bone finds. The results of the analyzes give a chronological reference with the earthquake of 346 which shook southern Sannio; however the archaeological data document the obliteration of the wells consistent with the seismic events of the second half of the fifth century, as mentioned above. Also in this case a collective reflection on possible explanations is necessary. It cannot be excluded that the earthquake of 346 caused only partial collapses in the city and that a strong instability affected the linear construction of the stage building, determining its functional end. The location of the theater on a natural terrace at a lower level than the rest of the city - and therefore easily marginalized from attendance - and an

initial demographic disintegration may have facilitated the decision to elect the pozzetti as a common burial place for infants. The subsequent earthquakes of the fifth century, marking the definitive building and consequently demographic disintegration of the city, may have prevented the continuation of the ritual behaviour.

I believe, however, that the area is not being abandoned as a place of transit for flocks; the customs function for the passage of livestock is in fact documented by the toponym associated with the area since the 12th century: Ansonia, from the Latin *ansarium*, i.e. right of entry (of goods); the close relationship plateau-track, in geo-morphological terms, does not end until the middle of the last century, coinciding with the significant socio-economic changes of the period.

However, the site recovers some sedentary form through scattered nuclei from around the 7th century. In fact, it seems that the small monastery leaning against the north-western walls dates back to this period <sup>22)</sup>. A new building dedicated to St. Paul stands on the southern ridge of the plateau between the eighth and ninth centuries <sup>23)</sup>; the church will be rebuilt several times mainly due to collapses due to seismic shocks. What you see today is the result of various reconstructions, including the one after the 1703 earthquake; unfortunately we must add the recent event of 2009 which caused heavy damage that is still verifiable, since the restoration works have yet to begin. But, if the plan and the structure of the church are linked both to earthquakes and, sometimes coinciding, to changes to the system resulting from the different architectural styles, the material used almost unequivocally comes from the public buildings of the Roman city. The decorative elements of the forensic temple and of the theater are clearly recognizable, in addition to the small blocks of the reticulated work which are implemented according to the original technique. On the other hand, a path along the southern side of the plateau easily connected the church with the theatre, which after the abandonment of the city had become a quarry of materials (with areas for reworking) used over the centuries for the construction of castles, villages, religious buildings even a few kilometers away. Moreover, the reservoir of the cavea also easily collected elements from the upper terrace occupied by the forensic complex.

An important modification to the building structure takes place with the insertion of a fortress on the southern part, at the edge of the plateau: an ideal

position for controlling the viability of the valley floor and optimal exploitation of the sector which had necessarily required a constructive commitment for the support of the cavea and not the simple support on the slope. Plausibly this intervention takes place in the ambit of the fortification phase of the L'Aquila basin between the 12th and 13th centuries <sup>9, 24</sup>). It is clear that the fort already recovers Roman materials, even for the manufacture of lime itself, as two limestones obtained in the orchestra invite us to think, excellently placed in relation to protection from the prevailing winds from the west.

A subsequent intervention on the theater marks the definitive division of the building into three distinct sectors:

1. the northern half partially retains the original structure as it is covered by collapses;
2. the southern half is obliterated by the fortress with the reuse of some ancient walls;
3. an intermediate sector sees the complete removal of the steps for the construction of rooms intended for the shelter of workers as well as a processing area for the reuse of residual materials from the collapsed theater and temple (Fig. 11).

The rooms are arranged in a series from west to east, facing onto a road that separates them from the fort and which leads to the church of S. Paul following the path halfway up the hill mentioned above. Excavation data connect what can be defined as a working-class neighborhood to a period between the end of the 13th and the middle of the 14th century. A relationship with the violent tremors that hit L'Aquila in 1349 <sup>9</sup>) is more than plausible, subsequently triggering an obvious building fervor which included the church itself. Later the rooms were abandoned and only their occasional reuse as a temporary shelter is documented; but the life of the last environment to the east is interrupted while the function of the neighborhood is still active; a layer of pantiles found in contact with the floor (Fig. 12) testifies to the collapse of the roof, probably resulting from an earthquake, and the layers that set upon it indicate a subsequent use as a landfill area.

Analyses were carried out by XlabF on three samples of tiled tiles from

1. from this late medieval environment;

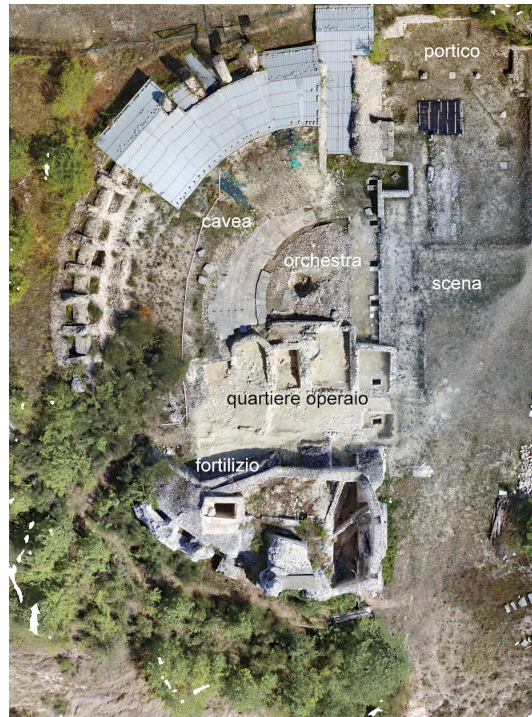


Figure 11: *The transformations of the Roman theater.*

2. from one of the wells of the theater, therefore from the roof of the stage building from the Claudian era;
3. from a room of the forum also linked to the Julio-Claudian phase.

The results show no difference between the samples. This may indicate that in the roof of the late medieval room no newly manufactured tiles were used, but that recovered tiles from the Roman age were used, also coming from other buildings in the city, since the roof of the stage building theatrical also included tiles, as evidenced by the elements piled up at the foot of the stage wall and found in the wells of the theatre, not just roof tiles; it is therefore possible that accumulations of the latter had remained, chosen over time from the urban rubble and, among other things, easier to implement. The analyzes carried



Figure 12: *Working-class neighborhood: environment ζ. Collapsed roof tiles on the floor.*

out have therefore better addressed some considerations on building reuse. In conclusion, I return to the initial reflection: the contribution of other specific skills to research on the city proves to be indispensable for fully addressing the development of a society in a period of considerable change, such as that between late antiquity and the early Middle Ages.

## References

1. G. De Benedittis, Considerazioni sulla transumanza, in I Georgofili, Quaderni (2001) 5, 19-24 (2002).
2. G. Barker, L'origine della pastorizia e della transumanza in Italia, in G. De Benedittis, Il mutevole aspetto di Clio. Le conferenze del premio E.T. Salmon1, 75-98 (1994).
3. L. Migliorati, Peltuinum. Un caso di pietrificazione di un'area di culto, in Saturnia Tellus, Atti del Congresso Internazionale, (Roma, 2004), Roma 2008, 341-356 (2008).
4. S. Agostini, M.A. Rossi and M. Tallini, Geologia e paleontologia del Qua-

- ternario nel territorio aquilano, in S. Bourdin, V. D'Ercole, I Vestini e il loro territorio dalla Preistoria al Medioevo, CEFR 494, 7-19 (2014).
5. L. Migliorati, Gli scavi di Peltuinum, in S. Bourdin, V. D'Ercole, I Vestini e il loro territorio dalla Preistoria al Medioevo, CEFR 494, pp. 249-260 (2014).
  6. L. Migliorati, Piceno meridionale e Sannio vestino: gli insediamenti pre-romani e le opzioni di Roma, in P.L. Dall'Aglio, C. Franceschelli, L. Maganzani, Atti IV Convegno Internazionale Studi Veleiati, 313-330 (2014).
  7. L. Migliorati, I. Fiore, A. Pansini, P.F. Rossi, T. Sgrulloni and A. Sperduti, Sepolti nel teatro: il valore simbolico dei cani in sepolture comuni infantili, in E. Lippolis, P. Vannicelli, V. Parisi, Il sacrificio. Forme rituali, linguaggi e strutture sociali, in Scienze dell'Antichità, 593-611 (2018).
  8. L. Migliorati, Terremoti e riuso: nuovi dati da una città romana dell'Appennino centrale, in R. Compatangelo-Soussignan, F. Diosono, F. Le Blay, Living with Seismic Phenomena in the Mediterranean and Beyond between Antiquity and the Middle Ages, 211-222 (2022).
  9. L. Migliorati, T. Sgrulloni and A. Vecchione, Peltuinum (Prata d'Ansidonia, L'Aquila) - Il teatro romano e il quartiere tardo-medievale di demolizione: lavori in corso, in Notizie Scavi n.s. I, 107-144 (2021).
  10. P. Sommella, Peltuinum: contributi alla discussione sulla città antica, in Peltuinum 2011-12, 271-286 (2011).
  11. F. Bianchi, Il tempio del foro, in Peltuinum 2011-12, 287-330 (2011).
  12. L. Migliorati and M. Buonocore, Peltuinum: nuovi dati dal foro, in Rend. Pont. Acc. 94, 301-357 (2021).
  13. D. Nepi, Il teatro di Peltuinum. Studio tecnico strutturale, in S. Bourdin, V. D'Ercole, I Vestini e il loro territorio dalla Preistoria al Medioevo, CEFR 494, 261-264 (2014).
  14. L. Migliorati, Peltuinum: un aggiornamento, JAT XVII, 107-126 (2007).

15. S. Panciera, Nuovi luoghi di culto a Roma dalle testimonianze epigrafiche, in *Archeologia laziale* 3 (Quaderni del centro di studio per l'archeologia etrusco-italica 4), 202-213 (1980).
16. S. Panciera, Nuovi luoghi di culto a Roma dalle testimonianze epigrafiche, S. Panciera, *Epigrafi, epigrafia, epigrafisti. Scritti vari e inediti (1956–2005) con note complementari e indici, I (Vetera, 16)*, 275-288 (2006).
17. C. Letta, La bonifica antica e la statio della flotta pretoria di Ravenna sul Fucino, in *Il Fucino e le aree limitrofe nell'antichità, Atti del Convegno di Archeologia*, 500-511 (1991).
18. C.F. Giuliani, Sfidando gli inferi: problemi di cantiere dell'emissario del Fucino, in *AEspA* 46, 39-54 (2008).
19. C.F. Giuliani, La Domus Flavia come problema, in *ATTA* 24, 43-58 (2014).
20. A. Sperduti, L. Migliorati, A. Pansini, T. Sgrulloni, P.F. Rossi, V. Vaccari, I. Fiore, Differential burial treatment of newborn infants from late Roman age. Children and dogs depositions at Peltuinum, *Atti del 3 Incontro Internazionale di Studi di Antropologia e Archeologia a confronto* 1, 299-313 (2018).
21. L. Migliorati, I. Fiore, A. Pansini, P.F. Rossi, T. Sgrulloni, A. Sperduti, Sepolti nel teatro: il valore simbolico dei cani in sepolture comuni infantili, *Scienze dell'Antichità* 23 (3), 593-611 (2017).
22. L. Tulipani, Da Peltuinum alla Civita Ansidonia, in A. Campanelli, *Peltuinum. Antica città sul tratturo*, 50-61 (1996).
23. L. Pani Ermini, Contributi alla storia delle diocesi di Amiternum, Furcona e Valva nell'alto Medioevo, in *Rend. Pont. Acc.* 44, 257-274 (1972).
24. A. Campanelli, La città romana di Peltuinum: storia di una ricerca, in *Peltuinum. Antica città sul tratturo*, 32-43 (1996).

**HIGH DOSE-RATE AND SPATIAL RESOLUTION X-RAY  
BEAM AT THE HIGH BRILLIANCE X-RAY LABORATORY  
(HIBRIX LAB)**

A. Alessio

*Dep. of Physics, Univ. Torino, and INFN-TO, Via Giuria 1, 10125 Torino, Italy*

S.B. Dabagov

*XLab Frascati, INFN - LNF, Via E. Fermi, 54, 00044 Frascati (Rome), Italy*

D. Hampai

*XLab Frascati, INFN - LNF, Via E. Fermi, 54, 00044 Frascati (Rome), Italy*

V. Guglielmotti

*XLab Frascati, INFN - LNF, Via E. Fermi, 54, 00044 Frascati (Rome), Italy*

A. Lo Giudice

*Dep. of Physics, Univ. Torino, and INFN-TO, Via Giuria 1, 10125 Torino, Italy*

A. Re

*Dep. of Physics, Univ. Torino, and INFN-TO, Via Giuria 1, 10125 Torino, Italy*

M. Truccato

*Dep. of Physics, Univ. Torino, and INFN-TO, Via Giuria 1, 10125 Torino, Italy*

F. Picollo

*Dep. of Physics, Univ. Torino, and INFN-TO, Via Giuria 1, 10125 Torino, Italy*

**Abstract**

The High-Brilliance X-ray laboratory (HiBriX Lab) of the University of Torino is here presented. This facility is based on a MetalJet X-ray source featuring high brilliance and two emission windows that allowed setting up two branches dedicated to different applications: one is arranged for imaging (both radiography and tomography) whereas the other one is for characterization (XRF and XRD) and/or irradiation with a micrometric resolution of the samples of interest (solid state as well as biological).

The present configuration of the microfocused branch, which takes advantage of polycapillary optics for the X-ray focusing, offers a minimum spot size of about 75 microns and a maximum flux density of  $2.7 \cdot 10^{10}$  ph s<sup>-1</sup> mm<sup>-2</sup>.

## 1 Introduction

To date, microfocus X-ray sources have been usually manufactured by means of conventional X-ray tubes, where high-energy electrons are accelerated towards a solid-state metal target, like for instance tungsten. This technology has an inherent limitation from the point of view of the maximum achievable brilliance because it requires quickly removing the heat induced by the impact between electrons and the target in order not to melt the latter. Indeed, the most performing traditional microfocus sources have either to limit the maximum current of the electron beam (0.5 mA can be considered as a typical maximum value) or to increase its size (50 microns can be considered as a typical minimum value in high-current mode). Smaller spot sizes down to about 5 microns in diameter are certainly possible, but in this case, the power of the electron beam has to be decreased to values as small as 4 W, therefore severely limiting the brilliance of the X-ray source.

In recent years, a novel technology based on the use of a liquid anode has been developed, which has already reached the maturity stage of commercialization due to the efforts made by Excillum AB. In this approach, the anode is represented by a Ga- or In-based alloy in its liquid state, which forms a jet with a diameter of the order of 70 microns flowing at a speed of about  $60 \text{ m s}^{-1}$ . On the one hand, this method exploits the fact that melting the anode is not a problem anymore because it has already been intentionally melted, and on the other hand any local accumulation of thermal energy is prevented by the high-speed flow of the liquid. In this way, the metal-jet technology allows for a power of 250 W to be delivered by an electron beam 20 microns in diameter, achieving a brilliance that is at least one order of magnitude higher compared to conventional microfocus sources <sup>1)</sup>.

With this innovative technology at its heart, HiBriX Lab was set up by integrating a variety of detectors and focusing optics to represent a unique laboratory in Italy and with a handful of comparable examples in the world. In this paper, we describe this facility that was designed to cover several applications such as:

- material characterization via  $\mu\text{XRD}$  and  $\mu\text{XRD}$  maps <sup>2, 3)</sup>;
- investigation of sensor performances by means of their evaluation in terms of charge collection efficiency or damage effects;

- single cell level radiobiology <sup>4, 5</sup>);
- X-ray imaging (2D radiography and 3D computed tomography - CT) of objects having a wide size range <sup>6</sup>).

## 2 Experimental Setup

The experimental setup is based on an X-ray source MetalJet D2+ by Excillum, which is able to operate at voltages between 40 and 160 kV while delivering an electron beam with a power value ranging approximately between 5 W and 250 W. The typical emission spot size is 20  $\mu\text{m}$  in diameter, but in principle, it can be reduced down to 5  $\mu\text{m}$  with position stability better than 0.5  $\mu\text{m}$  over 24 hours.

The liquid anode is made of an In/Ga/Sn (I1) alloy, resulting in the emission spectrum shown in Figure 1a, where intense emissions corresponding to the  $K_\alpha$  and  $K_\beta$  lines of these three elements can be observed, on top of a Bremsstrahlung background. As a reference, the brilliance of the Ga- $K_\alpha$  line (i.e. the most intense one) is rated as  $6.5 \cdot 10^{10}$  photons/(s·mm<sup>2</sup>·mrad<sup>2</sup>·line) for an emission spot 10  $\mu\text{m}$  in diameter and a power of 125 W.

The X-ray source is equipped with two Be windows on opposite sides of the jet allowing the extraction of two X-ray beams having an emission cone of 13° and 30°, respectively.

On one side a versatile X-ray imaging setup is installed, which allows the acquisition of radiography and tomography scans of very different kinds of samples: objects of dimensions in the sub-mm to few tenths of cm range, with wide variability in atomic number and density values. The acquisition is carried out through a flat panel XRD 1622 from Varex Imaging, with 200·200  $\mu\text{m}^2$  pixels and an active area of 41·41 cm<sup>2</sup>. The detector can be remotely controlled and automatically moved horizontally and vertically in a 1 m range and manually moved in the beam direction. To acquire a sequence of many projections at different angles, as necessary for tomography, a rotary platform is placed below the sample and remotely controlled.

On the other side, an X-ray microbeam setup is installed. X-ray photons are focused by polycapillary optics on the sample, which is mounted on three motorized stages. The polycapillary optics has been fabricated by INFN-XlabF and exploits total reflection to focus the beam to a spot of  $\sim 75$   $\mu\text{m}$  (Figure

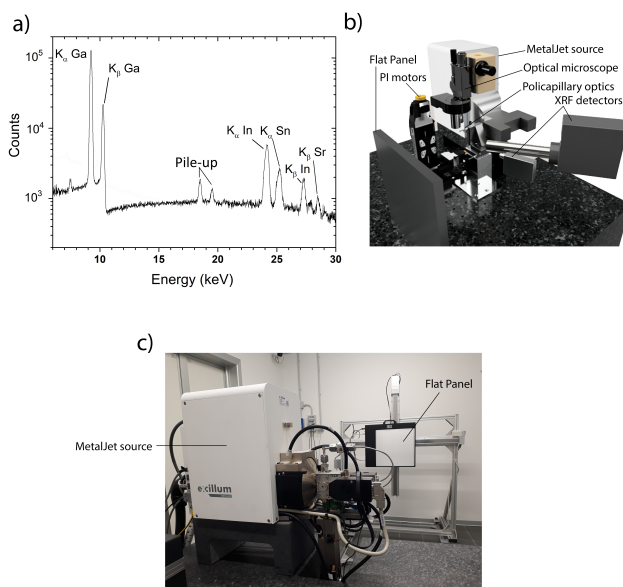


Figure 1: *Emission spectrum of the MetalJet source (a), schematics of the X-ray microbeam setup (b) and picture of X-ray imaging set-up (c).*

2a), corresponding to a maximum flux density of  $2.7 \cdot 10^{10} \text{ ph s}^{-1} \text{ mm}^{-2}$ . The polycapillary optics used has a full lens shape to focus the divergent beam from X-ray source. The lens provided a focal spot of  $\sim 80 \mu\text{m}$  and 50% transmission, characterized with a Cu Anode X-ray Source <sup>7)</sup>.

The flux has been measured by using a Canberra PD300-14-500AB Si photodiode and converting the measured photocurrent into the corresponding number of photons per second at the different powers of the source following the method reported <sup>8)</sup> (Figure 2b).

The microbeam setup is equipped with two Silicon Drift Detectors (SDD) for the acquisition of  $\mu\text{XRF}$  maps. The first detector is an Amptek XR-123 Fast SDD, which features an active area of  $25 \text{ mm}^2$  collimated to  $17 \text{ mm}^2$  and a maximum energy resolution of about 125 eV at 5.9 keV and a maximum output count rate of 40 kcps; the second detector is a Vortex- EM-5524-C by Hitachi with a sensor active area of  $100 \text{ mm}^2$  collimated to  $50 \text{ mm}^2$  and a sensor

thickness of 2 mm, which is able to provide an energy resolution of about 130 eV at the same energy of 5.9 keV and maximum output count rate of about 120 kcps. The combinations of Be window and sensor thicknesses are able to provide a quantum efficiency greater than 10% in the energy range between 0.84 and 32.7 keV for the Amptek and between 0.84 and 51.4 keV for the Vortex detector, respectively. The AMPTEK detector is interfaced with the PI motors through an Arduino Due board for synchronization of sample movements and data acquisition.

A flat panel RAD-ICON 2329 by Teledyne DALSA allows the precise alignment of the polycapillary optics with the optical axis of the X-ray source and the determination of the polycapillary input focal distance by means of an iterative procedure consisting of: i) scanning the optics in the plane normal to the optical axis of the X-ray source while recording images of the beam in order to centre the polycapillaries, and ii) scanning the optics along the optical axis while measuring the photon flux by means of the photodiode in order to maximize it. Two iterations are typically enough to align the optics. This flat panel is also intended for the collection of XRD patterns with micrometric resolution, but this is still to be implemented.

The spot size of the X-ray beam focused by the polycapillary optics was measured by means of the knife edge method. To this purpose, the sharp edge of a Cu electrode on a Shapal board was scanned along a direction normal to the optical axis of the source while recording the Cu fluorescence signal generated by the intersection of the beam with the electrode. The procedure has been repeated at different z positions along the optical axis, and for each position, the derivative of the Cu fluorescence signal was calculated and the corresponding Full Width at Half Maximum has been reported in Figure 2a. In this way, the output focal distance corresponding to the minimum spot size can be clearly identified.

This experimental setup will be completed with an optical microscope that will allow a precise alignment of the microbeam on the sample and easy determination of the focal point. Moreover, the installation of a motorized rotation stage for the sample will allow simultaneous XRF and XRD mapping, with photon fluxes unachievable by means of traditional laboratory scale X-ray sources.

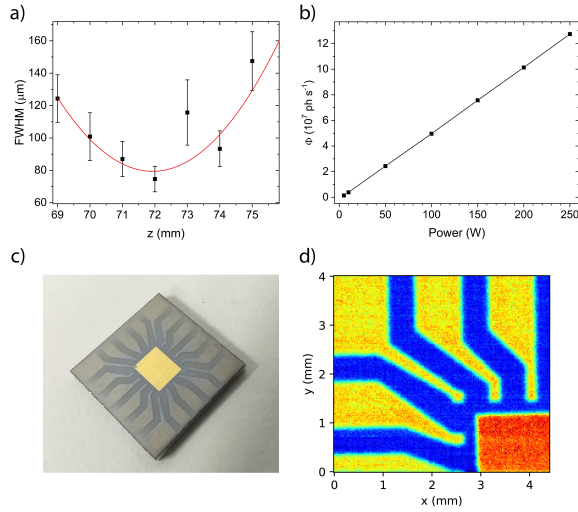


Figure 2: *Beam size at different  $z$  values obtained from knife edge method (a) and photon flux for different source power (b). Photograph of the Shapal board (c) and corresponding XRF map showing Cu electrodes (d).*

### 3 Conclusions

A High-Brilliance X-ray laboratory (HiBriX Lab) is presently under development at the University of Torino in the framework of regional and local projects, and the INFN project RESOLVE is presently stimulating its development by exploiting the corresponding assets. Procurement of the different components has been almost completed and their integration is underway, also by means of the development of specifically dedicated software for system control. To date, concerning the microfocused branch of the lab, a minimum spot size of about 75 microns and a maximum flux density of  $2.7 \cdot 10^{10}$  ph s $^{-1}$  mm $^{-2}$  has been achieved by means of the first polycapillary optics system specifically delivered by INFN X-lab in Frascati.

## 4 Acknowledgements

This work is supported by the following projects: RESOLVE project funded by National Institute of Nuclear Physics, PLaMeRaX and Biophysix projects funded by from CRT Foundation, SAX project funded by Regione Piemonte, "Departments of Excellence" (L. 232/2016) project funded by Italian MIUR, SAXSAB funded by University of Torino, HiBriX Lab funded by University of Torino and Compagnia di SanPaolo Foundation.

## References

1. O. Hemberg et al., Liquid-metal-jet anode electron-impact x-ray source, *Appl. Phys. Lett.* 83, 1483 (2003).
2. M. Truccato et al., Evidence of ion diffusion at room temperature in microcrystals of the  $\text{Bi}_2\text{Sr}_2\text{CaCu}_2\text{O}_{8+\delta}$  superconductor, *Appl. Phys. Lett.*, 86, 213116 (2005).
3. L. Bauer et al., Confocal micro-X-ray fluorescence spectroscopy with a liquid metal jet source, *J. Anal. At. Spectrom.*, 33, 1552-1558 (2018).
4. F. Picollo et al., Triggering Neurotransmitters Secretion from Single Cells by X - ray Nanobeam Irradiation, *Nano Lett.*, 20, 3889-3894 (2020).
5. G. Tomagra et al., Diamond-based sensors for in vitro cellular radiobiology: Simultaneous detection of cell exocytic activity and ionizing radiation, *Biosens. Bioelectron.*, 220, 114876 (2023).
6. F. Tansella et al, X-ray Computed Tomography Analysis of Historical Woodwind Instruments of the Late Eighteenth Century, *J. Imaging*, 8(10), 260 (2022).
7. D. Hampai et al., Shaped X-ray beams by channeling in polycapillary optics *Radiat. Phys. Chem.*, 174, 108965 (2020).
8. R. L. Owen et al., Determination of X-ray flux using silicon pin diodes, *J. Synchrotron Rad.* 16, 143-51 (2009).